Entanglement-Enhanced Bioimaging and Sensing

Thesis by
Manni He

In Partial Fulfillment of the Requirements for the
Degree of
Doctor of Philosophy

CALIFORNIA INSTITUTE OF TECHNOLOGY
Pasadena, California

2024
Defended February 21, 2024

Manni He
ORCID: 0009-0001-4237-900X

To Mom and Dad

ACKNOWLEDGEMENTS

This work would not be possible without the support of numerous mentors, colleagues, friends, and family members, to whom I am deeply grateful. The following notes contain those who deserve special recognition.

To Dr. Scott Cushing, my PhD advisor, it has been an incredible journey since we first started making entangled photons together over five years ago. I am eternally grateful to you for always believing in my potential, for sharing with me not only scientific knowledge but also key skills needed to become a well-rounded scientist, for supporting my mental health, and for helping me explore various career paths after graduate school.

I thank my thesis committee members, Dr. Lu Wei, Dr. Betty Hong, and Dr. Geoff Blake. You have been the most encouraging audience at every thesis progress meeting or exam. I am fortunate to have received your scientific and career advice.

To my past mentors, I could not have become a Caltech PhD student without your prior teaching. Dr. Caihong Dong at the Chinese Academy of Sciences, who took a chance on me while I was still a clueless high school student, thank you for launching my scientific career and introducing me to microbiology research. Dr. Ke Xu and Dr. Rui Yan from UC Berkeley, who welcomed me into the super-resolution imaging lab with open arms, thank you for helping me develop the mindset of a serious scientist that constantly seeks to answer deeper questions.

This work was made possible by the scientific help from my colleagues in the Cushing Lab at Caltech, including Dr. Bryce Hickam with whom I co-developed most of the experiments, Dr. Szilard Szoke, Nathan Harper, Emily Hwang, Hamilton Evans, Dr. Ye-Jin Kim, and Dr. Hanzhe Liu.

I also thank students in the Blake Lab, especially Dr. Griffin Mead, Dr. Haw Wei Lin, and Jax Dallas, and students in the Wei Lab, especially Dr. Kun Miao and Dongkwan Lee for offering scientific help with optics. I thank students in the Hong Lab and the Shapiro Lab, as well as Dr. Andres Collazo and Dr. Giada Spigolon at the Caltech Beckman Institute Biological Imaging Facility for help with bioimaging experiments.

I am grateful for being part of a close-knit and caring research group where I got to make many great friends, including Dr. Bryce Hickam, Dr. Jonathan Michelsen,

Dr. Isabel Klein, Danika Nimlos, Nathan Harper, Levi Palmer, Dr. Hanzhe Liu, Hamilton Evans, Jocelyn Mendes, Dr. Ye-Jin Kim, Wonseok Lee, Kim Pham, Alejandro Arellano, Yulu Cao, and others.

I am grateful to the friends I made at Caltech, many of whom are international students like myself as we bonded through similar struggles as expats. They include Marta Gonzalvo, Linh Le, Dr. Jaron Tong, Dr. Roman Korol, Liam Heidt, Dr. Sadie Dutton, Natalie Hills, Helena Awad, Ruben Mirzoyan, Dr. Taleen Dilanyan, Sven Sund, Silje Sund, Jake Evans, Dr. Alex Barth, Dr. Rui Cheng, and Dr. Yujia Tao.

I thank the staff at the Caltech Division of Chemistry and Chemical Engineering for their essential support, especially Elisha Okawa, Joe Drew, and Alison Ross Keller. I am also grateful to the Caltech Y for enriching my graduate school life through community service and activism. I am fortunate to have met the wonderful Caltech Y members and students, including Greg Fletcher, Dr. Athena Castro, Manisha Kapasiawala, Dr. Elyse Pennington, and Dr. Kathleen Kennedy.

I thank AcuFocus, Inc. for offering me the invaluable internship opportunity to gain insight into the medical device industry and to enrich my graduate studies. I am especially grateful to Jason Safabash and Laurent Hoffmann on the Research & Development team for their mentorship and guidance. I am also grateful to Tara Philips for discovering my résumé and supporting me throughout the internship.

Friends outside of Caltech, thank you for keeping me somewhat sane by taking me away from the campus, including Raul Jimenez, Carissa Kane, Sojin Ahn, Sam Joe, Tim Lin, Alejandro Grossman, Matt Dees, Jenn Rodig, Matt Rodig, and fencing Coach Bleu Aneiryn.

To my partner William Hight, I am fortunate to have met you. Thank you for always trying to listen to and understand my research struggles, for finding creative ways to help me de-stress, and for raising our sweet cat, Gabby, together. I cannot wait to start a new chapter of our lives in Seattle. I also thank John and Julie Hight for being my American parents and creating wonderful memories at family gatherings.

I am forever grateful to my parents for teaching me how to be a good person, for providing me with an excellent education, and for creating a happy childhood for me through thick and thin. You have sacrificed a lot by supporting me to study abroad since I was 18 years old. I hope I have made you proud. I also thank Cousin Chen Liang for being as close as a sister over the years, and her family for their support and love.

My studies and research are supported by Dr. Barbara Burger and the Biotechnology Leadership Program created by Dr. Frances Arnold. I am grateful for Dr. Burger and Dr. Arnold's mentorship and career support. Certain materials of this work are based upon work supported by the U.S. Department of Energy, Office of Science, Office of Basic Energy Sciences, under Grant DE-SC0020151 (S.K.C.). Certain materials of this work are also supported by the Tianqiao and Chrissy Chen Institute for Neuroscience and the Rosen Center for Bioengineering.

ABSTRACT

Studies of entangled light-matter interactions have been gaining momentum because of their potential applications in bioimaging and sensing. Entangled photons are predicted to linearize nonlinear optical processes and offer orders of magnitude of enhancement to the interaction cross sections. To investigate the validity of entanglement-enhanced bioimaging techniques, a continuous wave (CW)-powered, on-chip, broadband entangled light source based on periodically poled lithium tantalate (ppLT) was designed and characterized. This light source achieved femtosecond entangled correlation times comparable to classical ultrafast lasers with an unprecedented power of $\sim$ 100 nW in near-infrared (NIR), which is a crucial first step toward fully integrated, thin-film lithium niobate (TFLN)-based, visible to NIR entangled photon sources. This light source was then used for subsequent spectroscopy/microscopy experiments to systematically investigate the feasibility of entanglement-enabled microscopy techniques such as entangled two-photon absorption (ETPA) microscopy and entangled fluorescence lifetime measurements. A novel method was developed to measure fluorescence from ETPA using a spectrotemporally resolved Michelson interferometer which is good at eliminating false signals due to one-photon absorption and scattering. Careful experimental attempts at detecting virtual-state mediated ETPA from rhodamine 6G (R6G) and resonance-enhanced ETPA from indocyanine green (ICG) were made, and the ETPA signals were found to be below the instrument detection limits and often masked by one-photon effects such as scattering and linear absorption. Instead, experimental upper bounds were placed on the ETPA cross sections of the studied molecules, with an emphasis on continued improvement of the light source and instrument detection limits. On-chip entangled fluorescence lifetime imaging microscopy (entangled-FLIM) has also been identified as a new future development focus. The feasibility of the technique was demonstrated via a proof-of-principle experiment which measured the fluorescence lifetime of ICG in various solvents. Using entangled photons produced from a CW laser, the lifetime measurement scheme achieved a temporal resolution of 50 ps and a minimum measurable lifetime of 365 ps, which can be used to distinguish most biologically relevant fluorophores in the corresponding wavelength range. This experiment is a critical first step toward scalable, high-throughput, wavelength-multiplexed, and on-chip FLIM or lifetime measurements which could be used in label-free health monitoring technologies.

PUBLISHED CONTENT AND CONTRIBUTIONS

1. He, M., Hickam, B. P., Harper, N. & Cushing, S. K. Experimental Upper Bounds for Resonance-Enhanced Entangled Two-Photon Absorption Cross Section of Indocyanine Green. *The Journal of Chemical Physics,* Accepted (2024).
   M. H. conceived the study, identified the sample material, designed and conducted the experiments, analyzed data, performed mathematical modeling, and wrote a significant portion of the manuscript.

2. Harper, N., Hickam, B. P., He, M. & Cushing, S. K. Entangled Photon Correlations Allow a Continuous-Wave Laser Diode to Measure Single-Photon, Time-Resolved Fluorescence. *The Journal of Physical Chemistry Letters,* 5805–5811. https://doi.org/10.1021/acs.jpclett.3c01266 (2023).
   M. H. identified the sample material, co-designed the experiments, and wrote a portion of the manuscript.

3. Hickam, B. P., He, M., Harper, N., Szoke, S. & Cushing, S. K. Single-Photon Scattering Can Account for the Discrepancies among Entangled Two-Photon Measurement Techniques. *The Journal of Physical Chemistry Letters,* 4934–4940. https://pubs.acs.org/doi/10.1021/acs.jpclett.2c00865 (2022).
   M. H. conceived the study, designed the experiments, analyzed data, performed mathematical modeling, wrote a significant portion of the manuscript.

4. Szoke, S., He, M., Hickam, B. P. & Cushing, S. K. Designing High-Power, oOctave Spanning Entangled Photon Sources for Quantum Spectroscopy. *The Journal of Chemical Physics* **154,** 244201. https://aip.scitation.org/doi/10.1063/5.0053688 (2021).
   M. H. designed and conducted the experiments, analyzed data, performed mathematical modeling, and wrote a significant portion of the manuscript.

5. Szoke, S., Liu, H., Hickam, B. P., He, M. & Cushing, S. K. Entangled Light–Matter Interactions and Spectroscopy. *Journal of Materials Chemistry C* **8,** 10732–10741. http://pubs.rsc.org/en/content/articlelanding/2020/tc/d0tc02300k (2020).
   M. H. performed literature review, and wrote a portion of the manuscript.

TABLE OF CONTENTS

LIST OF ILLUSTRATIONS

LIST OF TABLES

NOMENCLATURE

BBO. Beta barium borate.

CMOS. Complementary metal-oxide-semiconductor.

CW. Continuous wave.

EMICCD. Electron multiplying intensified charge-coupled device.

ETPA. Entangled two-photon absorption.

FLIM. Fluorescence lifetime imaging microscopy.

ICG. Indocyanine green.

IR. Infrared.

KTP. Potassium titanyl phosphate.

LED. Light-emitting diode.

MgO. Magnesium oxide.

NIR. Near-infrared.

ppLT. Periodically poled lithium tantalate.

r-ETPA. Resonance-enhanced ETPA.

R6G. Rhodamine 6G.

SFG. Sum-frequency generation.

SHG. Second-harmonic generation.

SPAD. Single photon avalanche photodiode.

SPDC. Spontaneous parametric down-conversion.

SRS. Stimulated Raman scattering.

TCSPC. Time-correlated single photon counting.

TFLN. Thin-film lithium niobate.

TPA. Two-photon absorption.

UV. Ultraviolet.

v-ETPA. Virtual state-mediated ETPA.

ZnTPP. Zinc tetraphenylporphyrin.

Chapter 1

INTRODUCTION

Multiphoton microscopy has become a powerful tool for in vivo imaging at the cellular level because it improves spatial resolution and penetration depth beyond that of one-photon imaging. In particular, multiphoton excitation in the near-infrared (NIR, 700 nm - 1700 nm) reduces scattering, suppresses tissue autofluorescence, and improves penetration depths to allow deep tissue imaging and optogenetic studies [1]. Other "label-free" techniques such as second-harmonic generation (SHG) imaging [2] of collagen in brain tissues and stimulated Raman scattering microscopy [3, 4] are pushing the boundaries of cellular structure and kinetics studies. Time-resolved fluorescence measurements such as fluorescence lifetime imaging microscopy (FLIM) are also expanding the frontiers of multiplexed fluorescence and endogenous signal measurements [5, 6].

The large size, cost, and maintenance of ultrafast lasers have historically relegated advanced bioimaging techniques to academic laboratories. Recent advances in fiber and semiconductor integrated sources are now bringing commercial nonlinear microscopes to bioimaging centers around the world. However, even with these advances, the realm of truly compact, portable, distributable, or even tether-free on-subject nonlinear microscopy remains out of reach. For example, miniature single-photon microscopy has become a standard technique for optogenetic imaging and control of freely moving mammals [7], enabling more realistic studies of the complex neuronal circuits involved in animal behavior. Whereas single-photon microscopy can be powered by an integrated light-emitting diode (LED), there is not an on-chip version of a high peak power ultrafast laser. Fiber-optic tethers and bench-top electronics are always required [8]. Increasing the accessibility of nonlinear and time-resolved microscopies, and their inherent advantages, requires the development of on-chip, integrated laser sources that can approach the simplicity and power draw of an LED. Although this goal seems dauntingly unfeasible, the potential reward of an on-chip ultrafast light source is also immeasurable as it will not only allow for tetherless and information-rich deep tissue imaging (Fig. 1.1) but also translationally enable advanced, noninvasive health monitoring in consumer electronics [9, 10].

Figure 1.1: An imagined future for lab rats where on-chip entangled photon sources enable minimally invasive, tetherless, information-rich deep brain imaging.

To address this unmet need, my colleagues and I have made significant progress on two major fronts. First, we have developed various high-power (nW-μW), on-chip, entangled photon sources in ultraviolet (UV) to NIR wavelengths using periodically poled lithium tantalate (ppLT) [11] or a shared periodically poled thin-film lithium niobate (TFLN) platform [12, 13]. These entangled photon sources are compact and powered by continuous wave (CW) lasers, while also exhibiting femtosecond temporal correlations comparable to classical ultrafast lasers. Second, we have systematically investigated the feasibility of entanglement-enabled microscopy techniques such as entangled fluorescence lifetime measurements [14] and entangled two-photon absorption (ETPA) microscopy [15, 16], and have identified entangled-FLIM as a major future development focus that will enable scalable, on-chip, nonlinear bioimaging and sensing applications.

Entangled photons are produced in a process known as spontaneous parametric down-conversion (SPDC). As a pump laser photon travels through a nonlinear crystal, it can spontaneously split into two lower-energy photons which are entangled in energy and time. It is well known that the inherent correlations between entangled photons lead to spectroscopic enhancements in signal-to-noise[17–22] and diffraction limits[23] as well as measurement techniques such as ghost imaging [24–31]. However, the improvement factors of these techniques fundamentally depend on the entangled state photon number, N. For the most common biphoton state ($N = 2$), the fundamental upper limit to noise improvement is 41.4% ($\sqrt{N} - 1$). In this work, I have taken two different approaches to explore quantum advantages for microscopy beyond the photon-number enhancement, namely, entangled single-photon FLIM and ETPA. These two techniques utilize the large amount of frequency modes of

broadband entangled photons to achieve wavelength tunability and multiplexing (in the case of FLIM), or potentially orders of magnitude enhancement in signal strength (in the case of ETPA).

An intuitive way to understand why ETPA or entangled-FLIM could have orders of magnitude enhancements is to think of the energy-time entanglement as a form of constraint which guarantees that the photons within the pair, if they arrive simultaneously and spatially overlap at a sample, will act akin to the original photon that they were created from. In other words, the quantum correlations lead to entangled photons "linearizing" multiphoton processes such as two-photon absorption (TPA) [32, 33], SHG [34], and sum-frequency generation (SFG) [35, 36]. However, the absolute magnitude of the quantum enhancement on the interaction cross section is still in debate [37–40]. In this work, I measure the quantum enhancements on TPA cross sections of organic fluorescent molecules using various spectrotemporally resolved methods. Similar to other recent reports, the linearized ETPA cross sections are now mainly measured to be in the 10^{-25} to 10^{-22} cm^2/molecule range [15, 16, 33, 36, 41, 42], in contrast to earlier reports in the 10^{-19} to 10^{-17} cm^2/molecule range [43–45]. The temporal correlations between entangled photons also theoretically allow for time-resolved fluorescence imaging [46–48], although experimental demonstrations and the exact performance metrics using a CW laser only emerged in 2023, as reported by our group [14] and two other groups [49, 50] within several months.

This work is a detailed description of the aforementioned results. First, Chapter 2 provides an overview of the field of entangled light-matter interactions from five years ago. Key hypotheses in this overview, including predictions on the quantum enhancement of ETPA cross sections and proposed schemes for time-resolved entangled spectroscopy, have formed the basis of my PhD research. Over the past five years, through experiments (and theories) including the ones described in Chapters 3-6, the landscape of the field has changed significantly as the reported ETPA enhancements became exceedingly weak for bioimaging applications, and a new research direction is needed to sustain the momentum of the field. Chapter 3 explains the design and performance of an early iteration of the on-chip entangled light source, based on bulk ppLT instead of TFLN [11]. Importantly, this light source achieved 125 nm of down-converted bandwidth and 57 fs of entangled correlation times with an unprecedented power of $\sim$ 100 nW in NIR, which was a crucial first step toward fully integrated, TFLN-based, visible to NIR entangled

photon sources later achieved by my colleagues [12, 13]. This light source was also used for subsequent spectroscopy/microscopy experiments in Chapters 4-6. Chapter 4 presents a novel method to measure fluorescence from ETPA using a spectrotemporally resolved Michelson interferometer. This method is a variation of the Hong-Ou-Mandel interferometer [51] and is good at eliminating false signals due to one-photon absorption and scattering. By attempting to measure ETPA signals from rhodamine 6G (R6G), I conclude that the ETPA signal was below the detection limit of the instrument and masked by one-photon scatter which had a cross section on the order of 10^{-21} cm^2 [16]. Chapter 5 extends the currently available ETPA samples to include real-state mediated two-photon excitations of indocyanine green (ICG). Although resonance-enhanced TPA is theoretically more susceptible to entanglement enhancement than virtual-state mediated TPA is, I show that experimentally this advantage was negligible and still below instrument detection limits [15]. Instead, an upper limit of $6(\pm 2) \times 10^{-23}$ cm^2 was placed on the resonance-enhanced ETPA cross section of ICG. Chapter 6 introduces our new research focus of on-chip entangled single-photon FLIM via a proof-of-principle experiment measuring the fluorescence lifetime of ICG in various solvents. Using entangled photons produced from a CW laser, our lifetime measurement scheme achieved a temporal resolution of 50 ps and a minimum measurable lifetime of 365 ps, which can be used to distinguish most biologically relevant fluorophores in the wavelength range of the light source [52]. This experiment opens the door to scalable, high-throughput, wavelength-multiplexed, and on-chip FLIM or lifetime measurements which could be used in label-free health monitoring technologies. In Chapter 7, *Conclusion and Outlook*, I summarize the results, elaborate on the potential impact of on-chip entangled FLIM, and discuss other plausible avenues for entanglement-enhanced bioimaging and sensing.

References

1. Wang, S., Li, B. & Zhang, F. Molecular Fluorophores for Deep-Tissue Bioimaging. *ACS Central Science*. https://doi.org/10.1021/acscentsci.0c00544 (2020).

2. Esquibel, C. R. *et al.* Second Harmonic Generation Imaging of Collagen in Chronically Implantable Electrodes in Brain Tissue. *Frontiers in Neuroscience* **14.** https://www.frontiersin.org/articles/10.3389/fnins.2020.00095 (2020).

3. Moester, M. J., Zada, L., Fokker, B., Ariese, F. & de Boer, J. F. Stimulated Raman scattering microscopy with long wavelengths for improved imaging

depth. *Journal of Raman Spectroscopy* **50,** 1321–1328. https://onlinelibrary.wiley.com/doi/abs/10.1002/jrs.5494 (2019).

4. Hill, A. H., Manifold, B. & Fu, D. Tissue imaging depth limit of stimulated Raman scattering microscopy. *Biomedical Optics Express* **11,** 762–774. https://opg.optica.org/boe/abstract.cfm?uri=boe-11-2-762 (2020).

5. Bright, F. V. & Munson, C. A. Time-resolved fluorescence spectroscopy for illuminating complex systems. *Analytica Chimica Acta. ANALYTICAL HORIZONS - An International Symposium celebrating the publication of Volume 500 of Analytica Chimica Acta* **500,** 71–104. https://www.sciencedirect.com/science/article/pii/S0003267003007232 (2003).

6. Cundall, R. *Time-Resolved Fluorescence Spectroscopy in Biochemistry and Biology* ISBN: 978-1-4757-1634-4 (Springer Science & Business Media, 2013).

7. Yizhar, O., Fenno, L. E., Davidson, T. J., Mogri, M. & Deisseroth, K. Optogenetics in Neural Systems. *Neuron* **71,** 9–34. https://www.cell.com/neuron/abstract/S0896-6273(11)00504-6 (2011).

8. Zong, W. *et al.* Miniature two-photon microscopy for enlarged field-of-view, multi-plane and long-term brain imaging. *Nature Methods* **18,** 46–49. http://www.nature.com/articles/s41592-020-01024-z (2021).

9. Todaro, B., Begarani, F., Sartori, F. & Luin, S. Is Raman the best strategy towards the development of non-invasive continuous glucose monitoring devices for diabetes management? *Frontiers in Chemistry* **10.** https://www.frontiersin.org/articles/10.3389/fchem.2022.994272 (2022).

10. Narayanamurthy, V. *et al.* Skin cancer detection using non-invasive techniques. *RSC Advances* **8,** 28095–28130. https://pubs.rsc.org/en/content/articlelanding/2018/ra/c8ra04164d (2018).

11. Szoke, S., He, M., Hickam, B. P. & Cushing, S. K. Designing High-Power, oOctave Spanning Entangled Photon Sources for Quantum Spectroscopy. *The Journal of Chemical Physics* **154,** 244201. https://aip.scitation.org/doi/10.1063/5.0053688 (2021).

12. Harper, N. A. *et al.* Highly efficient visible and near-IR photon pair generation with thin-film lithium niobate. *arXiv:2310.07046.* http://arxiv.org/abs/2310.07046 (2023).

13. Hwang, E. *et al.* Tunable and efficient ultraviolet generation with periodically poled lithium niobate. *Optics Letters* **48,** 3917–3920. https://opg.optica.org/ol/abstract.cfm?uri=ol-48-15-3917 (2023).

14. Harper, N., Hickam, B. P., He, M. & Cushing, S. K. Entangled Photon Correlations Allow a Continuous-Wave Laser Diode to Measure Single-Photon, Time-Resolved Fluorescence. *The Journal of Physical Chemistry Letters,* 5805–5811. https://doi.org/10.1021/acs.jpclett.3c01266 (2023).

15. He, M., Hickam, B. P., Harper, N. & Cushing, S. K. Experimental Upper Bounds for Resonance-Enhanced Entangled Two-Photon Absorption Cross Section of Indocyanine Green. *The Journal of Chemical Physics,* Accepted (2024).

16. Hickam, B. P., He, M., Harper, N., Szoke, S. & Cushing, S. K. Single-Photon Scattering Can Account for the Discrepancies among Entangled Two-Photon Measurement Techniques. *The Journal of Physical Chemistry Letters,* 4934–4940. https://pubs.acs.org/doi/10.1021/acs.jpclett.2c00865 (2022).

17. Casacio, C. A. *et al.* Quantum-enhanced nonlinear microscopy. *Nature* **594,** 201–206. https://www.nature.com/articles/s41586-021-03528-w (2021).

18. Jedrkiewicz, O. *et al.* Detection of Sub-Shot-Noise Spatial Correlation in High-Gain Parametric Down Conversion. *Physical Review Letters* **93,** 243601. https://link.aps.org/doi/10.1103/PhysRevLett.93.243601 (2004).

19. Bondani, M., Allevi, A., Zambra, G., Paris, M. G. A. & Andreoni, A. Sub-shot-noise photon-number correlation in a mesoscopic twin beam of light. *Physical Review A* **76,** 013833. https://link.aps.org/doi/10.1103/PhysRevA.76.013833 (2007).

20. Brida, G., Genovese, M. & Ruo Berchera, I. Experimental realization of sub-shot-noise quantum imaging. *Nature Photonics* **4,** 227–230. https://www.nature.com/articles/nphoton.2010.29 (2010).

21. Giovannetti, V., Lloyd, S. & Maccone, L. Advances in quantum metrology. *Nature Photonics* **5,** 222–229. https://www.nature.com/articles/nphoton.2011.35 (2011).

22. Ono, T., Okamoto, R. & Takeuchi, S. An entanglement-enhanced microscope. *Nature Communications* **4,** 2426. https://www.nature.com/articles/ncomms3426 (2013).

23. Boto, A. N. *et al.* Quantum Interferometric Optical Lithography: Exploiting Entanglement to Beat the Diffraction Limit. *Physical Review Letters* **85,** 2733–2736. https://link.aps.org/doi/10.1103/PhysRevLett.85.2733 (2000).

24. Lemos, G. B. *et al.* Quantum imaging with undetected photons. *Nature* **512,** 409–412. https://www.nature.com/articles/nature13586 (2014).

25. Bornman, N. *et al.* Ghost imaging using entanglement-swapped photons. *npj Quantum Information* **5,** 1–6. https://www.nature.com/articles/s41534-019-0176-5 (2019).

26. Aspden, R. S., Tasca, D. S., Boyd, R. W. & Padgett, M. J. EPR-based ghost imaging using a single-photon-sensitive camera. *New Journal of Physics* **15,** 073032. https://doi.org/10.1088%2F1367-2630%2F15%2F7%2F073032 (2013).

27. Kviatkovsky, I., Chrzanowski, H. M., Avery, E. G., Bartolomaeus, H. & Ramelow, S. Microscopy with undetected photons in the mid-infrared. *Science Advances.* https://www.science.org/doi/abs/10.1126/sciadv.abd0264 (2020).

28. Padgett, M. J. & Boyd, R. W. An introduction to ghost imaging: quantum and classical. *Philosophical Transactions of the Royal Society A: Mathematical, Physical and Engineering Sciences* **375,** 20160233. https://royalsocietypublishing.org/doi/10.1098/rsta.2016.0233 (2017).

29. Abouraddy, A. F., Stone, P. R., Sergienko, A. V., Saleh, B. E. A. & Teich, M. C. Entangled-Photon Imaging of a Pure Phase Object. *Physical Review Letters* **93,** 213903. https://link.aps.org/doi/10.1103/PhysRevLett.93.213903 (2004).

30. Pittman, T. B., Shih, Y. H., Strekalov, D. V. & Sergienko, A. V. Optical imaging by means of two-photon quantum entanglement. *Physical Review A* **52,** R3429–R3432. https://link.aps.org/doi/10.1103/PhysRevA.52.R3429 (1995).

31. Strekalov, D. V., Sergienko, A. V., Klyshko, D. N. & Shih, Y. H. Observation of Two-Photon "Ghost" Interference and Diffraction. *Physical Review Letters* **74,** 3600–3603. https://link.aps.org/doi/10.1103/PhysRevLett.74.3600 (1995).

32. Georgiades, N. P., Polzik, E. S., Edamatsu, K., Kimble, H. J. & Parkins, A. S. Nonclassical Excitation for Atoms in a Squeezed Vacuum. *Physical Review Letters* **75,** 3426–3429. https://link.aps.org/doi/10.1103/PhysRevLett.75.3426 (1995).

33. Tabakaev, D. *et al.* Spatial Properties of Entangled Two-Photon Absorption. *Physical Review Letters* **129,** 183601. https://link.aps.org/doi/10.1103/PhysRevLett.129.183601 (2022).

34. Spasibko, K. Y. *et al.* Multiphoton Effects Enhanced due to Ultrafast Photon-Number Fluctuations. *Physical Review Letters* **119,** 223603. https://link.aps.org/doi/10.1103/PhysRevLett.119.223603 (2017).

35. Dayan, B., Pe'er, A., Friesem, A. A. & Silberberg, Y. Nonlinear Interactions with an Ultrahigh Flux of Broadband Entangled Photons. *Physical Review Letters* **94,** 043602. https://link.aps.org/doi/10.1103/PhysRevLett.94.043602 (2005).

36. Landes, T. *et al.* Experimental feasibility of molecular two-photon absorption with isolated time-frequency-entangled photon pairs. *Physical Review Research* **3,** 033154. https://link.aps.org/doi/10.1103/PhysRevResearch.3.033154 (2021).

37. Landes, T. *et al.* Quantifying the enhancement of two-photon absorption due to spectral-temporal entanglement. *Optics Express* **29,** 20022–20033. https://opg.optica.org/oe/abstract.cfm?uri=oe-29-13-20022 (2021).

38. Drago, C. & Sipe, J. E. Aspects of two-photon absorption of squeezed light: The continuous-wave limit. *Physical Review A* **106,** 023115. https://link.aps.org/doi/10.1103/PhysRevA.106.023115 (2022).

39. Burdick, R. K. *et al.* Predicting and Controlling Entangled Two-Photon Absorption in Diatomic Molecules. *The Journal of Physical Chemistry A* **122,** 8198–8212. https://doi.org/10.1021/acs.jpca.8b07466 (2018).

40. Fei, H.-B., Jost, B. M., Popescu, S., Saleh, B. E. A. & Teich, M. C. Entanglement-Induced Two-Photon Transparency. *Physical Review Letters* **78,** 1679–1682. https://link.aps.org/doi/10.1103/PhysRevLett.78.1679 (1997).

41. Parzuchowski, K. M. *et al.* Setting Bounds on Entangled Two-Photon Absorption Cross Sections in Common Fluorophores. *Physical Review Applied* **15,** 044012. https://link.aps.org/doi/10.1103/PhysRevApplied.15.044012 (2021).

42. Mikhaylov, A. *et al.* Hot-Band Absorption Can Mimic Entangled Two-Photon Absorption. *The Journal of Physical Chemistry Letters* **13,** 1489–1493. https://doi.org/10.1021/acs.jpclett.1c03751 (2022).

43. Harpham, M. R., Suzer, O., Ma, C.-Q., Bauerle, P. & Goodson, T. Thiophene Dendrimers as Entangled Photon Sensor Materials. *Journal of the American Chemical Society* **131,** 973–979. https://doi.org/10.1021/ja803268s (2009).

44. Guzman, A. R., Harpham, M. R., Suzer, O., Haley, M. M. & Goodson, T. G. Spatial Control of Entangled Two-Photon Absorption with Organic Chromophores. *Journal of the American Chemical Society* **132,** 7840–7841. https://doi.org/10.1021/ja1016816 (2010).

45. Upton, L. *et al.* Optically Excited Entangled States in Organic Molecules Illuminate the Dark. *The Journal of Physical Chemistry Letters* **4,** 2046–2052. https://doi.org/10.1021/jz400851d (2013).

46. Scarcelli, G. & Yun, S. H. Entangled-photon coincidence fluorescence imaging. *Optics Express* **16,** 16189–16194. https://opg.optica.org/oe/abstract.cfm?uri=oe-16-20-16189 (2008).

47. Asban, S., Dorfman, K. E. & Mukamel, S. Interferometric spectroscopy with quantum light: Revealing out-of-time-ordering correlators. *The Journal of Chemical Physics* **154,** 210901. https://doi.org/10.1063/5.0047776 (2021).

48. Oka, H. Real-time analysis of two-photon excitation by correlated photons: Pulse-width dependence of excitation efficiency. *Physical Review A* **81,** 053837. https://link.aps.org/doi/10.1103/PhysRevA.81.053837 (2010).

49. Eshun, A. *et al.* Fluorescence lifetime measurements using photon pair correlations generated via spontaneous parametric down conversion (SPDC). *Optics Express* **31,** 26935–26947. https://opg.optica.org/oe/abstract.cfm?uri=oe-31-16-26935 (2023).

50. Li, Q. *et al.* Single-photon absorption and emission from a natural photosynthetic complex. *Nature* **619,** 300–304. https://www.nature.com/articles/s41586-023-06121-5 (2023).

51. Hong, C. K., Ou, Z. Y. & Mandel, L. Measurement of subpicosecond time intervals between two photons by interference. *Physical Review Letters* **59,** 2044–2046. https://link.aps.org/doi/10.1103/PhysRevLett.59.2044 (1987).

52. Berezin, M. Y. & Achilefu, S. Fluorescence Lifetime Measurements and Biological Imaging. *Chemical Reviews* **110,** 2641–2684. https://doi.org/10.1021/cr900343z (2010).

Chapter 2

ENTANGLED LIGHT-MATTER INTERACTIONS AND SPECTROSCOPY

ABSTRACT

Entangled photons exhibit non-classical light-matter interactions that create new opportunities in materials and molecular science. For example, in entangled two-photon absorption, the intensity-dependence scales linearly as if only one photon was present. The entangled two-photon absorption cross section approaches but does not match the one-photon absorption cross section. The entangled two-photon cross section also does not follow classical two-photon molecular design motifs. Questions such as these seed the rich but nascent field of entangled light-matter interactions. In this perspective, we use the experimental developments in entangled photon spectroscopy to outline the current status of the field. Now that the fundamental tools are outlined, it is time to start the exploration of how how materials, molecules, and devices can control or utilize interactions with entangled photons.

Most of this chapter has been adapted with permission from:

Szoke, S. *et al.* Entangled Light–Matter Interactions and Spectroscopy. *Journal of Materials Chemistry C* **8,** 10732–10741. http://pubs.rsc.org/en/content/articlelanding/2020/tc/d0tc02300k (2020).

2.1 Introduction

Entanglement is arguably one of the most nonintuitive and fascinating phenomena in the quantum world. Entanglement refers to a many-body quantum state that cannot be decomposed into the product of each individual particle's state in the system [1]. Entangled states can be generated and measured in systems of particles including photons, electrons, and atoms. When a subset of particles in an entangled system interact with external stimuli, the many-body wavefunction of the whole system undergoes decoherence. This decoherence and the associated wavefunction collapse lie at the foundation of many technologies utilizing entanglement as a resource, such as quantum computation, communication, and information sciences [2].

In addition to these technologies, an emerging trend is to explore how entangled light-matter interactions differ from classical interactions. For example, entangled photons lead to two-photon absorption and sum frequency processes that scale linearly as if they are one-photon processes [3–9]. Two-photon experiments should therefore be possible at over a million times lower fluxes than classical experiments. Theoretical predictions suggest the same will be true for three and higher photon processes, converting nonlinear optical processes into linear processes [10]. Entangled photons have also been proposed for the excitation and control of excited state superpositions for qubits and molecular polaritons [11–13]. However, the origin of entangled light-matter interactions and the structural motifs in material and molecular design remain largely unexplored.

The exploration of entangled light-matter interactions currently resides in spectroscopic studies [14]. The central idea is to use the non-classical interference patterns between entangled photon pairs to measure femtosecond and longer processes. Intriguingly, such measurements can be performed using only few-photon fluxes, allowing access to new intensity scalings and quantum phenomena [14]. Entangled photon spectroscopy also offers new possibilities when applied to more classical phenomena. For example, entangled photons can break classical noise limits [15–19] and are predicted to break Fourier reciprocal spectral and temporal precisions [20–23]. A 500 nm bandwidth of entangled biphoton pairs compressed to a few femtoseconds is predicted to only interact at the wavelength and linewidth specified by the input pump laser, usually <1 MHz for a modern Ti:Sapphire oscillator. A narrow excited state distribution can therefore be created with high temporal resolution, potentially allowing new forms of quantum control [21].

At its heart, entangled photon spectroscopy relies on measuring changes in the quantum correlations of photons. The ability of entangled photons to couple, or not, with multi-particle excitations in materials is an intriguing question, both spectroscopically and from an application point of view. Entanglement has been proposed as fundamental to electron–electron and electron–phonon interactions in processes ranging from many-body correlations to singlet–triplet splitting [24–26]. In addition to the linearization of nonlinear interactions, we believe the potential for quantum correlated photons to create or interact with correlations in materials is why entangled light–matter interactions deserve further investigation in this field.

This chapter will provide a perspective on the current status of entangled light–matter interactions. Spectroscopic developments are used to outline the broader questions of how materials and molecules interact with entangled photons. Experimental exploration to date is limited to a few materials systems, partially due to the nascent development of these spectroscopic techniques. For example, entangled two-photon absorption has only been studied in a handful of molecular fluorophores [6, 27–33]. However, the potential applications of entangled light–matter interactions make exploration and application in the materials field an intriguing possibility.

2.2 Hong–Ou–Mandel interference and biphotons

To better understand entangled photon light–matter interactions, it is insightful to look at the fundamentals of the Hong–Ou–Mandel (HOM) interference [34]. The HOM effect serves as the basis for most entangled spectroscopy methods. A step-by-step guide to constructing an HOM interferometer can be found in Ref. [35]. In general, one pump photon is down-converted to create two lower energy daughter photons through spontaneous parametric down-conversion (SPDC). The daughter photons are collectively termed a biphoton. After temporal and polarization compensation in one arm, the two photons are made to meet and interfere at a 50:50 beamsplitter. Two single photon avalanche detectors (SPADs) then measure whether the photons leave opposite or same sides of the beamsplitter.

Classically, there are four possible outcomes of transmission (T) and reflection (R) for the two photons, as depicted in Fig. 2.1(a): RR, TT, RT, TR. The indistinguishable character of the biphoton leads to the amplitudes of TT and RR destructively interfering in the entangled case [34], leaving the only measurable outcome of both photons leaving the same side of the beamsplitter. If the time delay or relative polarization between the photons is changed, or any other modification is made that

partially distinguishes the biphoton pair, the interference will decrease. The width and amplitude of the interference dip therefore carries a signature of the light–matter interaction that the entangled photons have witnessed [36]. Measuring these variations in the interference dip enable the possibility for spectroscopy. As an example, Fig. 2.1(b) and (c) show the modulation of the interference dip when absorption is introduced in one arm of the HOM interferometer [37].

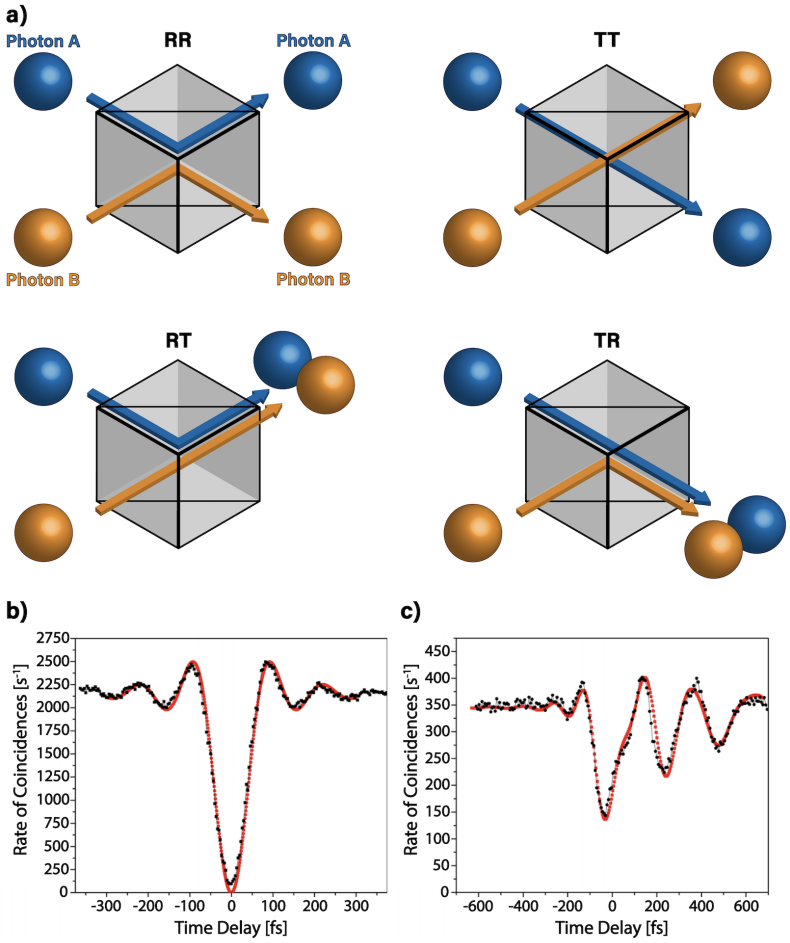

Figure 2.1: Hong–Ou–Mandel interference with photons. (a) Depiction of the four possible outcomes when two photons interact at a beamsplitter. When two entangled photons are present, the TT and RR outcomes cancel, and both photons leave the same side of the beam splitter. (b) This nonclassical interference leads to a dip in the coincidence counts. (c) HOM dip modulation due to a Nd:YAG crystal being placed in one arm of the HOM interferometer causing an entangled photon to interact with a sample with resonant states before the beam splitter. The excited state polarization is imprinted on the interference. Experimental results adapted from Ref. [37].

For a full mathematical derivation of the HOM dip, please refer to Ref. [38]. Briefly, the interference dip is explained mathematically as follows. Beamsplitter operators $\hat{B}_a$ and $\hat{B}_b$ are first defined which act on the bosonic mode operators to give a unitary transformation of an input state in ports a/b to the output in ports c/d.

$$\hat{a}^\dagger \xrightarrow{\hat{B}_a} \frac{1}{\sqrt{2}}\left(\hat{c}^\dagger + i\hat{d}^\dagger\right), \hat{b}^\dagger \xrightarrow{\hat{B}_b} \frac{1}{\sqrt{2}}\left(i\hat{c}^\dagger + \hat{d}^\dagger\right) \tag{2.1}$$

$$\hat{B}_a |1\rangle_a = \hat{B}_a \hat{a}^\dagger |0\rangle_a = \frac{1}{\sqrt{2}}(|1\rangle_c |0\rangle_d + i |0\rangle_c |1\rangle_d) \tag{2.2}$$

$$\hat{B}_b |1\rangle_b = \hat{B}_b \hat{b}^\dagger |0\rangle_b = \frac{1}{\sqrt{2}}(i |1\rangle_c |0\rangle_d + |0\rangle_c |1\rangle_d) \tag{2.3}$$

with $\hat{a}^\dagger$, $\hat{b}^\dagger$, $\hat{c}^\dagger$, and $\hat{d}^\dagger$ being the creation operators for the photons in ports a, b, c, and d, respectively, acting on the vacuum state $|0\rangle$. It is important to note that the beamsplitter operator introduces a $\pi/2$ phase shift in the reflected photon's output state. Next, assume a pair of entangled photons, each of which is defined by a singly occupied Fock state, is introduced into both input ports a and b:

$$\begin{aligned}\hat{B}_a\hat{B}_b |1\rangle_a |1\rangle_b &= \frac{1}{2}\left(\hat{c}^\dagger + i\hat{d}^\dagger\right)\left(i\hat{c}^\dagger + \hat{d}^\dagger\right)|0\rangle_c |0\rangle_d \\ &= \frac{1}{2}\left(i\hat{c}^{\dagger 2} + \hat{c}^\dagger\hat{d}^\dagger - \hat{d}^\dagger\hat{c}^\dagger + i\hat{d}^{\dagger 2}\right)|0\rangle_c |0\rangle_d .\end{aligned} \tag{2.4}$$

The phase shift leads to the commutator term between the two photon modes in Eqn. 2.4. Given that the photons are indistinguishable, the commutation relation for the creation operators equals zero,

$$[\hat{c}^\dagger, \hat{d}^\dagger] = [\hat{c}^\dagger\hat{d}^\dagger - \hat{d}^\dagger\hat{c}^\dagger] = 0 \tag{2.5}$$

and the only terms left are the RT and TR terms such that both photons must leave the same side, resulting in a N00N state as the output:

$$\frac{1}{2}\left(i\hat{c}^{\dagger 2} + i\hat{d}^{\dagger 2}\right)|0\rangle_c |0\rangle_d = \frac{1}{\sqrt{2}}\left(i |2\rangle_c |0\rangle_d + |0\rangle_c |2\rangle_d\right). \tag{2.6}$$

Consequently, only one of the two photon counting detectors will register a detection event. This results in the characteristic interference dip in the coincidence counting

scheme (Fig. 2.1(b)). Entangled photon spectroscopy can therefore be thought of as a measure of how light–matter interactions modify the commutator in Eqn. 2.5.

Before a discussion of the practical considerations of SPDC, a few technical points should be clarified. First, HOM interference should be more correctly viewed as 'biphoton interference' since it relies on the indistinguishability of the two bosons as well as the underlying entanglement between them. Second, an HOM interference for a two-photon entangled state is only possible if the entangled biphoton wavepacket has a symmetric spectrum about the frequency degenerate diagonal, irrespective of whether the two photons are frequency degenerate or non-degenerate. Without this condition being met, the interference vanishes, and the beamsplitter becomes transparent with respect to the two input photons. In the case of two independent single-photon wavepackets, the condition for HOM interference indeed becomes that the two single-photon wavepackets must be identical. In practice, this means that care must be taken how the two-photon states to be used are generated and how the two independent beam paths are optically treated [39].

2.3 Generation and detection of entangled photons

The two down-converted photons from SPDC display strong correlations in time, energy, and momentum due to the parametric mixing process. The time and energy correlations originate from the individual photons being generated simultaneously with energies that must sum to that of the pump photon. The momentum correlation is dictated by the phase matching condition. Energy-time entangled states can be viewed as the most general type of entangled states. Hyper-entangled photon states, e.g., entangled both in energy-time and in polarization, can lead to significant improvements in the experimental measurement statistics and the robustness of the spectroscopic setup [40, 41].

The simplest experimental approach to SPDC is using birefringent phase matching (BPM) in a χ^2 nonlinear crystal such as β-barium borate or lithium triborate [42, 43]. Generation rates of $\sim 10^3 - 10^4$ counts per s per mW are achieved with pump powers of a few tens of mW. Given that SPADs generally saturate at around $10^6 - 10^7$ counts per s, this generation rate is sufficient for coincidence counting experiments with most pulsed laser systems. However, due to the strict phase matching condition, the generated entangled photons have a narrow bandwidth. Other issues include cross-polarized pump/daughter photon combinations in Type-I and Type-II down-

conversion, beam walk-off issues due to birefringence, a limited wavelength mixing range, and reliance on weaker nonlinear tensor elements.

Quasi-phase matching (QPM) can generate broadband entangled photons more efficiently for spectroscopic applications. In this approach, a spatially periodic modulation of a ferroelectric nonlinear material is used to rectify the phase-mismatch of the three-wave mixing process, as illustrated in Fig. 2.2(a). This is achieved by using the additional momentum contribution from the crystal periodicity in the overall phase matching [44, 45]. The QPM approach makes it possible to take advantage of stronger elements of the nonlinear tensor, as well as to implement Type-0 phase-matching whereby all three waves are co-polarized [46]. The down-converted photon flux can be as high as 10^9 pairs per s per mW of the pump power by spatially confining the pump in chip-integrated photonic waveguides [47]. A particularly salient feature of QPM is that, since the crystal period can be arbitrarily chosen, it can be used to phase-match any desirable wavelength combinations. Further, by utilizing a longitudinally varying period, a collection of phase matching conditions can be used to create broadband SPDC fluxes [48–51]. Temperature controlled lithium niobate, lithium tantalate, and potassium titanyl phosphate are generally used given that they are transparent from the UV to mid-infrared wavelengths [52, 53].

Quasi-phase matching allows for two important advantages in spectroscopy. First, a sufficiently broadband flux of entangled photons can be used to increase average power levels without saturating the single photon per mode limit. As measured in our lab and others, almost microwatt fluxes of entangled photons spanning more than 500 nm can be created using QPM gratings [54]. The broad bandwidth allows for pulse-shaping and few-femtosecond resolutions. Second, the enhanced power levels allow spectrally and temporally resolved detection in reasonable time frames. In practice, this means that even microwatts of pump power would be enough to saturate a SPAD, suggesting that ultrafast entangled photon spectroscopy can be driven by a CW diode laser instead of expensive femtosecond laser amplifiers. Chip-integrated entangled photons are also easily fiber coupled. This provides alignment-free daily operations and an easy way to control and maintain the properties of entangled photons, such as spatial profile, over a broad bandwidth.

Multiplexed photon counting schemes are another area that could yield benefits in the application of entangled spectroscopy in materials science. Both EM-CCDs and SPAD arrays are coming to maturity, allowing spectral multiplexing of the photon counting process [55–58]. With a broadband, higher flux source, even a

simple USB spectrometer can be used to measure spectral changes. Higher fluxes also allow phase-sensitive HOM techniques to be used which measure both 2nd and 3rd order correlations [59]. The difference between an HOM interferometer and a phase-unlocked HOM interferometer is conceptually similar to the difference between an autocorrelator and a frequency resolved optical gating (FROG) setup in ultrafast optics – the former only measures the intensity autocorrelation while the latter contains additional phase information.

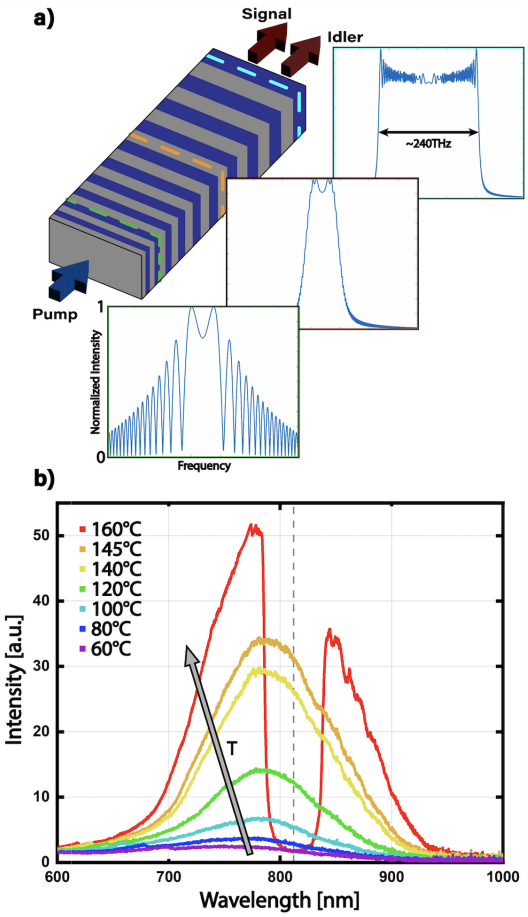

Figure 2.2: Periodic poling for generating broadband entangled photon pairs. (a) Cartoon of a periodically poled waveguide with linear chirp, where purple and gray represent domains of opposing poling. Insets show the simulated downconversion spectrum at three points along the lithium tantalate waveguide; (green)-start, (orange)-center, (cyan)-end. The effect of the chirp is to broaden the output to a bandwidth of $\sim$ 240 THz ($\sim$ 510 nm). (b) Experimental spectra of a periodically poled lithium tantalate grating where the working temperature of the crystal is tuned.

2.4 Spectroscopy with one entangled photon

One class of entangled photon spectroscopy utilizes the non-local nature of the entanglement. The general idea is that the interaction between the sample and one photon in the entangled pair can be revealed by measuring its entangled partner, even when it does not interact with the sample directly. Experimentally, one photon interaction can be introduced by placing a sample in one arm of the HOM interferometer shown in Fig. 2.3. The sample imparts phase and amplitude changes on the entangled photon it interacts with, which affects the biphoton indistinguishability and modulates the HOM dip [37].

While it seems trivial to measure absorption profiles with entangled photon interference, the technique allows spectroscopy and microscopy at one wavelength using vastly different wavelengths [60–62]. Spectroscopic signatures, such as absorption spectra are reconstructed by monitoring the changes to the coincidence counts when a sample is inserted into the signal arm of the HOM interferometer and resolving the wavelength of the idler arm [63–65]. For example, if the SPDC process creates an entangled IR and visible photon pair, the absorption of the photon at the IR wavelength can be inferred by measuring its visible partner [66]. This particular case has been demonstrated in CO_2 as shown in Fig. 2.3 [60]. This effect is predicted to work for any range of experiments, such as X-Ray [67, 68], THz, and electron spectroscopies, although practical limitations arise from generating such ultra-broadband SPDC sources.

Entangled one-photon spectroscopy has been applied to applications ranging from remote sensing to ghost imaging. For example, quantum ghost imaging relies on the coherence between the down-converted beams to record the image of an object with photons that do not interact with it directly [62, 69–75]. Quantum optical coherence tomography (QOCT) offers improved resolution and sensitivity by exploiting the dispersion cancelling properties of the entangled wavepacket, as well as the anticorrelation between entangled pairs, to construct quantum interference patterns corresponding to sample depth [76–78]. Entangled photons can also increase measurement sensitivities as compared with classical photons. The standard quantum limit for noise scales as $1/\sqrt{N}$, where N is the number of measurements. Using entangled photons, this improves to $1/N$ [79]. A prototypical example is using N00N states to enhance the measurement precision of the phase shift in an interferometer [80, 81]. Sub-shot-noise imaging of weak absorbing objects has also been achieved [17].

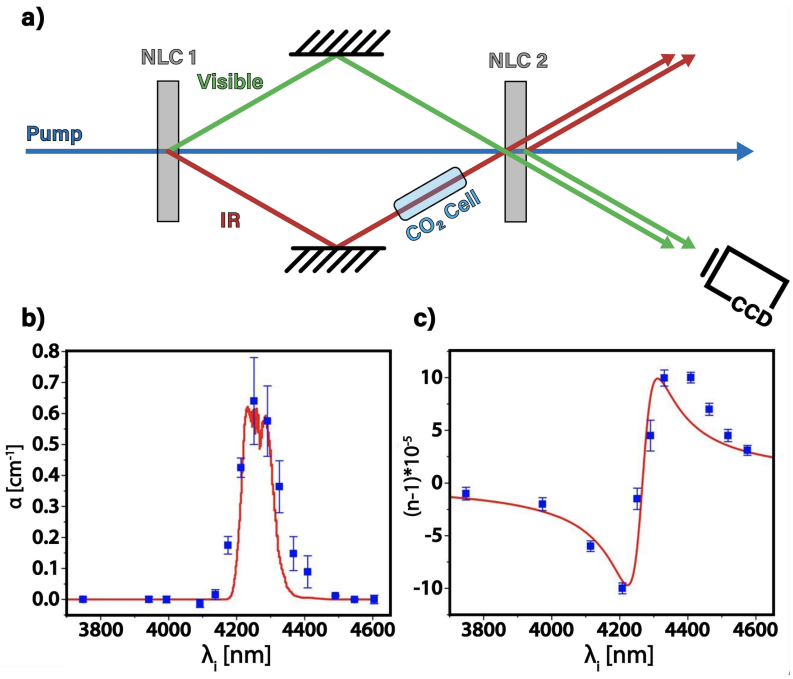

Figure 2.3: Measuring infrared absorption with visible photons. (a) Experimental layout. Entangled infrared (IR) and visible photons are generated through SPDC on the first nonlinear crystal (NLC1). A CO_2 cell is placed in the IR path to introduced absorption. The IR and visible photons cross at the second nonlinear crystal (NLC2) and interfere with the SPDC photons from NLC2. The interference pattern for the visible photons, which do not interact with the CO_2 are recorded. (b) IR absorption spectrum extracted from visible interference measurement. (c) Refractive index near the CO_2 resonance. Adapted from Ref. [60].

2.5 Spectroscopy with two or more entangled photons

Multiple entangled photon interactions can be split into two categories: the linearization of nonlinear interactions by preserving the correlations between the entangled photons (i.e., entangled two-photon absorption), and measurements in which a sample modifies the correlations between photons to measure excited state properties. Multiphoton entangled experiments are performed by replacing the beam splitter in an HOM interferometer so that both entangled photons interact with a sample. Whereas many one photon entangled interactions can be reproduced with shaped classical light, the interactions of two or more entangled photons with a sample lead to non-classical processes [14, 23, 82]. These interactions arise directly from the two-photon indistinguishability. Overly generalized, when the sample interacts with the biphoton pair, its response is as if only one photon were incident with the sum of

their energies. Before being spatially and temporally overlapped, the two entangled photons propagate in the material as if they were separate photons.

The two-photon interaction can therefore be modulated by time-delaying or shaping one side of the HOM interferometer. This allows for the measurement of excited state polarizations as well as populations. For example, multidimensional spectroscopy can be recreated by using three or more entangled photons or pulse shaping the entangled photons [14, 83, 84]. Compared to conventional multidimensional spectroscopy, entangled multidimensional spectroscopy is predicted to suppress the uncorrelated background levels and enhance the sensitivity to electronic couplings, manifested as pronounced off-diagonal cross-peaks in the 2D spectra, Fig. 2.4.

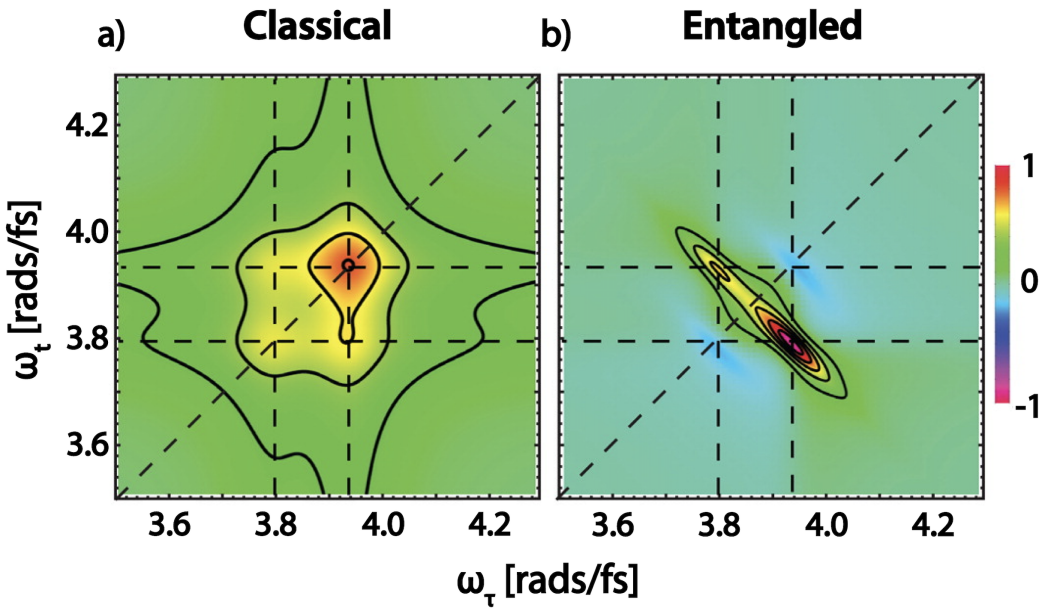

Figure 2.4: Simulated two-dimensional fluorescence spectra for electronically coupled molecular dimer with (a) classical light sources, and (b) entangled photon pairs. Multidimensional spectroscopy with entangled photons has improved sensitivity to the dimer conformation. Adapted from Ref. [83].

There are other distinct differences between nonlinear entangled and classical spectroscopy. First, the two entangled photons are predicted to act as one only if their coherence/entanglement time, represented by the width of the HOM dip, is shorter than the decoherence of the excited state being measured. The coherence/ entanglement time can therefore be used to alter and control the nonlinear process, allowing another route to multidimensional spectroscopy [85]. The measured spectrum is

again more sensitive to electronic coupling than in the classical case. Second, temporal dynamics in entangled photon experiments are measured via the correlations between the two entangled photons. Unlike pump probe spectroscopy, the temporal dynamics are not inferred from the sample's impulse response to a multiphoton pump pulse. Third, the entangled photons can measure whether an excited state superposition they excite in a qubit preserves their entanglement. Entangled photon interactions are therefore predicted to be sensitive probes for many-body dynamics and collective states [24, 86, 87].

Entangled photon spectroscopy also has the potential to measure ultrafast dynamics with higher spectral resolution than a classical approach. For entangled photon spectroscopy, the energy resolution is given by the down-converted pump source's linewidth. This is because the frequency–frequency photon distribution created by SPDC is correlated to the downconverted center frequency as shown in Fig. 2.5 [21]. This is compared with the Gaussian distribution commonly associated with a laser, in which any two photons can interact with the sample (Fig. 2.5(a) compared to Fig. 2.5(b)). In an entangled interaction, only the frequency conjugate pair will interact with the material, postselecting the photons along the frequency diagonal. All entangled photon interactions therefore add up to within the pump linewidth of the original pump laser source for the SPDC, and the frequency resolution is decoupled from the temporal resolution (Fig. 2.5(c) compared to Fig. 2.5(d)). Broadband entangled two-photon absorption in rubidium has already demonstrated a 3 to 5 orders of magnitude improvement on spectral and temporal resolution [88]. It has also been suggested that the creation of only conjugate electric fields optimizes the otherwise nonlinear interaction.

The temporal resolution of the entangled experiment is still proportional to the bandwidth of the down-converted photons. The width of the HOM dip can therefore be changed by modulating the relative time delay of the different frequencies using a pulse shaper [88]. Combining pulse-shaping and entangled photons is predicted to allow non-classical population distribution and novel photochemistry processes [88–91]. The decoupled temporal and spectral resolution has been predicted to create narrow bandwidth excited state populations from femtosecond bandwidths as shown in Fig. 2.5(e) compared to Fig. 2.5(f). Simulation also suggests that under entangled two-photon excitation, the intermediate single-exciton transport in the bacterial reaction center of Blastocholoris viridis can be suppressed and nonclassical control of two-exciton states can be achieved [89].

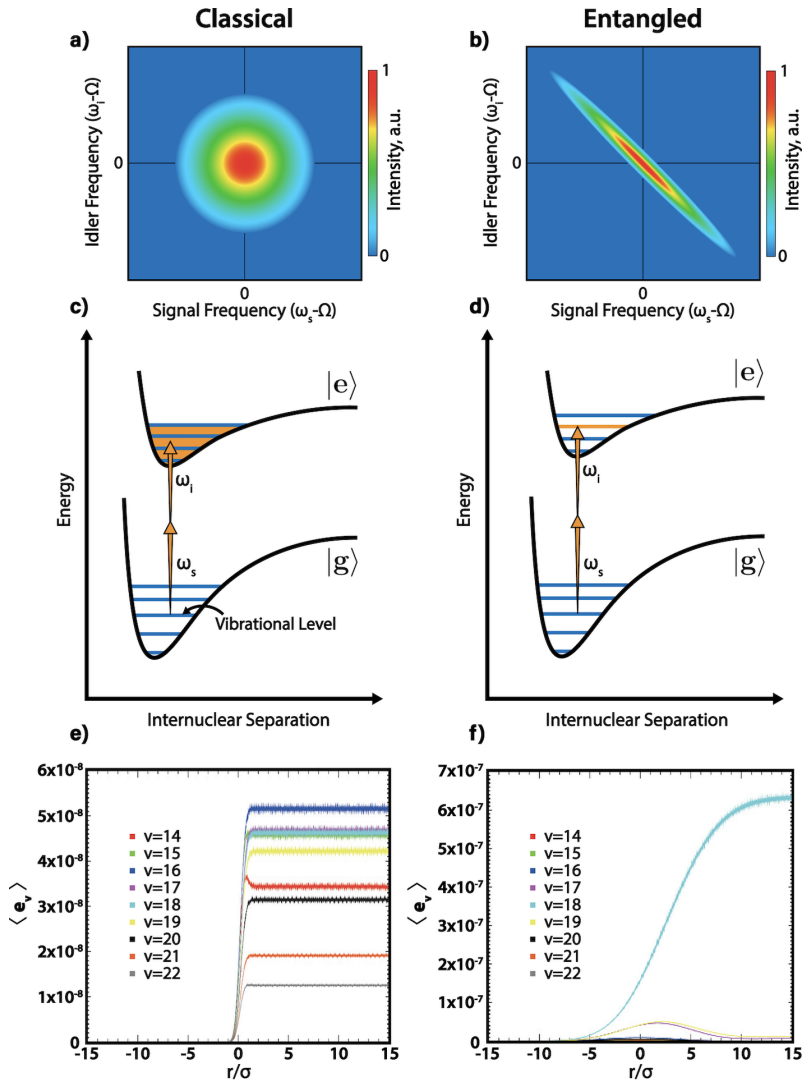

Figure 2.5: Spectral resolution in entangled two-photon spectroscopy. (a) Gaussian frequency distribution for uncorrelated photons as common from a classical laser. (b) Frequency anti-correlation for entangled photon pairs from SPDC. (c) The classical frequency distribution means that any combination of photons can excite the sample. A pulsed laser therefore excites an ensemble of vibrational states as predicted in (e). (d) The entangled photon frequency distribution means that transitions only occur that add up to the pump source's linewidth. Selective excitation of a single vibronic level therefore is predicted to occur independent of the SPDC bandwidth and temporal resolution (f). (e) Excited states population with pulsed laser excitation, where multiple vibronic levels are populated. Theoretical data (e) and (f) adapted from Ref. [21].

2.6 Current directions in entangled light-matter interactions

Several intriguing directions exist in exploring entangled light-matter interactions. One entangled photon interaction suggests that material and molecular interactions

can modulate the probability of measuring a second, non-interacting photon. The role this could have in transmuting material and chemical changes, as well as in processes like energy transfer, leave many open questions. Perhaps most intriguing are interactions with two or more entangled photons. Oversimplified, when two entangled photons are incident on a sample, they can appear as one photon with their summed energy. Nonlinear, multiphoton interactions up to N photons are therefore predicted to scale linearly [10]. The linearity of two photon entangled process was previously measured in sodium and cesium [7, 8] and has now been repeated in some molecular and solid-state systems (Fig. 6) [4, 6, 7, 9, 32, 33]. Similar to the beamsplitter in the HOM interferometer, the strong amplitude and phase correlation [92] within the entangled photon pair of SPDC suppresses higher order interaction terms [88].

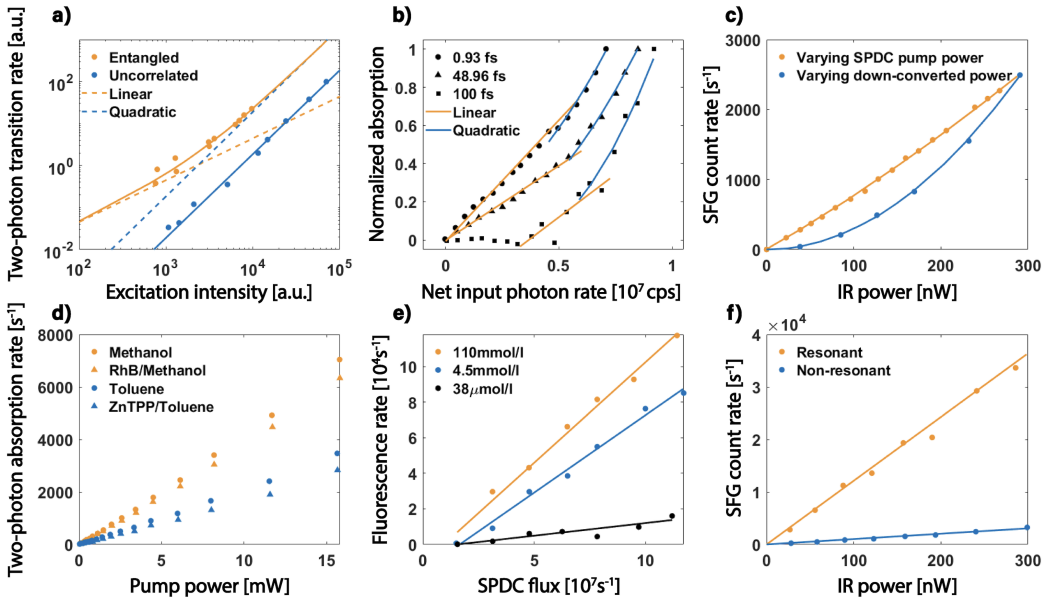

Figure 2.6: The linearity of various entangled two-photon processes as a function of power. (a) Two-photon transition rate in trapped cesium with entangled and coherent light. Transition rate for uncorrelated coherent excitation is reduced by a factor of 10 for comparison. (b) Power dependence of ETPA rate in porphyrin dendrimer under 3 different entanglement times. (c) Power dependence of sum-frequency generation with entangled photons. (d) ETPA rate for RhB and ZnTPP in solvent. (e) ETPA-induced fluorescence rate for Rh6G in ethanol under different concentration. (f) Resonantly enhanced sum-frequency generation with entangled photons. Data presented are adapted from Refs. [4, 6, 7, 9, 32, 33].

While the entangled two-photon intensity scaling can be understood, the cross section of the process raises many questions. The entangled photon cross sections

measured to date in molecular systems fall within the $10^{-17} - 10^{-18}$ cm^2 range [6]. This cross section is closer to that of a single photon absorption event, 10^{-16} cm^2, and orders of magnitude larger than that of a classical two-photon absorption event, 10^{-47} cm^{4}s. Why the entangled two-photon absorption cross section does not match the classical one photon cross section, despite both processes being linear, is an open question. The entangled two-photon absorption cross section also does not appear to follow classical two-photon absorption rules in organic porphyrin dendrimers [6].

In practice, the entangled two-photon absorption will compete with the semiclassical two-photon absorption. Their relative contribution is quantified by the ratio between the entangled absorption rate αI and the uncorrelated two-photon absorption rate βI^2, where α and β are associated cross sections. An entangled process is more efficient ($I < \alpha/\beta$) for fluxes lower than a GW for currently measured cross sections. The ratio can also be used to see that, for example, a one mW entangled photon flux has the same excitation rate as a million times more powerful classical laser. When calculating these ratios, it is important to include the conversion from W to photons per s through the ratio of $1J = 6.242 * 10^{18}$ eV for the βI^2. This must be done to cancel the cm^{4}s units when going to photons per s.

To study ultrafast material dynamics, an important factor in entangled two-photon absorption is the coherence (entanglement time) relative to the decoherence of the excited state. Studies on several diatomic molecules and organic porphyrin dendrimers have suggested that transitions involving virtual states respond to entangled two-photon excitations at a different timescale than transitions involving other mechanisms, such as excited state charge transfer [6, 93]. The entangled two-photon absorption cross section may therefore vary drastically between different transitions, exhibiting nonmonotonic dependence on the entanglement time, even if two systems classical cross sections are similar.

However, few experimental systems have been measured to date to confirm these rules. Measurements have yet to be repeated in condensed matter, low dimensional materials, or other common molecules — leaving many open questions as to how two or more photon entangled interactions can be optimized. The primary questions can be summarized as: (1) how do intermediate states control the entangled photon interaction, (2) what structural motifs can increase or decrease the strength of the entangled photon interaction, (3) how does excited state coupling with spins, vibrations, and electrons preserve or decrease the entangled light–matter interactions, and (4) more generally, how to utilize entanglement to reveal and engineer novel ma-

terials and device responses that are not accessible with traditional methods. Other open questions, such as how selection rules are modified by polarization entangled photons and how photonic enhancement techniques will modify the interactions [94–102], promise for intriguing expansions to existing fields.

Controlling the entangled multiphoton interactions has practical as well as fundamental motivation. Entangled two-photon processes can occur at the same rate as a pulsed-laser-induced two-photon excitations but at over a million times lower fluxes, accounting for the intensity scaling between quadratic and linear processes. If the material and molecular design parameters can be optimized, optoelectronic and biomedical applications using two-photon processes could be driven by a CW laser diode instead of a pulsed laser. Theory has also shown that due to the linear scaling, the spectrally overlapped simulated Raman scattering and two-photon absorption can be separated and selectively excited by tuning the entanglement properties of the pump [103]. For imaging applications, entangled two-photon fluorescence is suitable for in-depth imaging of photosensitive tissues at low flux. The linear scaling and enhanced cross section are predicted to occur for N-photon interactions, potentially bringing linearization to a family of nonlinear optical techniques [10]. Entangled multiphoton interactions have also been predicted to increase resonance energy transfer by several orders of magnitude [104] — and it can be extrapolated that the entangled effects will extend to most applications of multiphoton processes.

2.7 New opportunities in materials science

The key distinction of entangled photon excitation, aside from the linearization of nonlinear processes, is that the entangled photons can be made to show quantum correlations in multiple variables (polarization, energy, OAM, etc.) [105]. By interfering these entangled states of light with the quantum correlated excitations of a material, new properties and applications are to be expected [106]. Or, it may be possible to dynamically form correlations between two independent excitations that are not regularly present [107–111]. This key difference may lead to new insights in spectroscopy, but perhaps more excitingly, new degrees of control in quantum materials. In this section, we outline a few potential directions that entangled light-matter interactions could have an immediate benefit in.

First and foremost, the study and understanding of entangled light-matter interactions could become critical in the age of quantum computing and information systems [112, 113]. How the entangled photon correlations are modified, favor-

ably or not, by material elements is key for coupling qubit systems together as well as for investigating the types of control schemes that could be applicable to complex quantum systems [114]. Perhaps even more fundamentally, entanglement is suggested to be at the heart of quantum materials, which display strong electronic and nucleon correlations [115]. The inclusion of correlations in any Hamiltonian is the key to describing complex phenomena and for accurate calculations [116]. Many such Hamiltonians are also proposed to include entanglement, such as singlet–triplet scattering [25]. While the Fermi liquid theory and the Hubbard model have been used with great success, the direct experimental measurement of these strong interactions remains a difficult challenge [117–119]. The change in entangled photon correlations interacting with such systems may prove key, complementing approaches like ultracold atoms in optical lattices [120] and second quanta scans in multidimensional spectroscopy [121].

The ability of entangled photons to perform nonlinear optics with low power CW lasers should also prove transformative for photonics and electro-optical devices. Common components such as frequency mixers, saturable absorbers, or phase shifters can operate without a pulsed laser input, while wide band gap materials can be interacted with via photons at half the band gap energy. Additional functionality can be implemented in such devices relying on the preservation or change of the entangled photon correlations. An experiment that demonstrates this concept is to create polarization entangled biphoton states and couple one of the photons into a plasmonic metamaterial [122]. The coupled polarization state is determined and modulated by detecting the polarization of its partner. By altering the coupled polarization non-locally, the plasmonic device could in principle operate from perfect absorption to full transmission. The general idea of manipulating the material's functions non-locally via entanglement could lead to multifunctional integrated devices such as quantum logic gates, but also has fundamental advantages in processes like resonant energy transfer [104, 123].

An important goal in materials science is the on-demand manipulation of electrons in solids via the application of external stimuli [124]. The coupling of the entangled photon pair's quantum correlations to strongly correlated materials could result in novel, exotic responses. One example would be in the field of valleytronics [125, 126]. In two-dimensional semiconductors such as MoS_2, distinct valleys can be populated under a resonant excitation by circularly polarized light [125]. The circularly polarized excitation photon can be replaced by an entangled photon

pair. More precisely, a cross-polarized pair could be generated via Type-II down-conversion, after which the biphoton is split into its orthogonal polarization modes via a polarizing beamsplitter. A subsequent change in basis to circular polarization can be achieved by a pair of quarter–waveplates in both arms of the HOM type setup. The entangled photon energies could be set to select one or both valley excitations. The superposition between the spin state and the entangled photons would allow measurements of spin decoherence and coupling between the valleys. A similar idea could be used to test the ability of topological insulators to maintain spin correlations relative to photonic correlations.

Entangled photons could also find applications in material fabrication and lithography. Proposed techniques such as quantum photolithography aim to utilize entangled photons prepared in a N00N state to overcome the diffraction limit by a factor of $1/N$, alleviating the need to go to shorter UV wavelengths [127]. The enhanced cross section for entangled multiphoton absorption could allow simplified photolithography and growth schemes, techniques that use below band gap light for patterning, or even additional degrees of freedom by using two or more entangled states. The microscopic chemical processes that govern photopolymerization or photocatalytic growth processes might similarly be tuned by entanglement.

2.8 Outlook

While much work has gone into exploring entangled photons for quantum information and computational applications, the basics of entangled light–matter interactions and the potential applications in chemistry and material science are largely unexplored. In general, the field is advancing rapidly on the theoretical front, but most experimental questions remain open. How materials and molecular design can control entangled light–matter interactions remains mostly unknown, especially in materials and condensed matter systems. Given the relative ease of high-flux entangled photon generation, the simplicity of the optical schemes, and the various potential advantages of using non-classical light, we foresee entangled light–matter interactions being a rapidly growing field in the near future.

References

1. Horodecki, R., Horodecki, P., Horodecki, M. & Horodecki, K. Quantum entanglement. *Reviews of Modern Physics* **81,** 865–942. https://link.aps.org/doi/10.1103/RevModPhys.81.865 (2009).

2. Nielsen, M. A. & Chuang, I. Quantum Computation and Quantum Information. *American Journal of Physics* **70,** 558–559. https://aapt.scitation.org/doi/10.1119/1.1463744 (2002).

3. Javanainen, J. & Gould, P. L. Linear intensity dependence of a two-photon transition rate. *Physical Review A* **41,** 5088–5091. https://link.aps.org/doi/10.1103/PhysRevA.41.5088 (1990).

4. Dayan, B., Pe'er, A., Friesem, A. A. & Silberberg, Y. Nonlinear Interactions with an Ultrahigh Flux of Broadband Entangled Photons. *Physical Review Letters* **94,** 043602. https://link.aps.org/doi/10.1103/PhysRevLett.94.043602 (2005).

5. Dayan, B. Theory of two-photon interactions with broadband down-converted light and entangled photons. *Physical Review A* **76,** 043813. https://link.aps.org/doi/10.1103/PhysRevA.76.043813 (2007).

6. Lee, D.-I. & Goodson, T. Entangled Photon Absorption in an Organic Porphyrin Dendrimer. *The Journal of Physical Chemistry B* **110,** 25582–25585. https://pubs.acs.org/doi/10.1021/jp066767g (2006).

7. Georgiades, N. P., Polzik, E. S., Edamatsu, K., Kimble, H. J. & Parkins, A. S. Nonclassical Excitation for Atoms in a Squeezed Vacuum. *Physical Review Letters* **75,** 3426–3429. https://link.aps.org/doi/10.1103/PhysRevLett.75.3426 (1995).

8. Teich, M. C., Schroeer, J. M. & Wolga, G. J. Double-Quantum Photoelectric Emission from Sodium Metal. *Physical Review Letters* **13,** 611–614. https://link.aps.org/doi/10.1103/PhysRevLett.13.611 (1964).

9. Sensarn, S., Ali-Khan, I., Yin, G. Y. & Harris, S. E. Resonant Sum Frequency Generation with Time-Energy Entangled Photons. *Physical Review Letters* **102,** 053602. https://link.aps.org/doi/10.1103/PhysRevLett.102.053602 (2009).

10. Peřina, J., Saleh, B. E. A. & Teich, M. C. Multiphoton absorption cross section and virtual-state spectroscopy for the entangled n-photon state. *Physical Review A* **57,** 3972–3986. https://link.aps.org/doi/10.1103/PhysRevA.57.3972 (1998).

11. Matsukevich, D. N. *et al.* Entanglement of a Photon and a Collective Atomic Excitation. *Physical Review Letters* **95,** 040405. https://link.aps.org/doi/10.1103/PhysRevLett.95.040405 (2005).

12. Xiang, B. *et al.* Manipulating optical nonlinearities of molecular polaritons by delocalization. *Science Advances* **5,** eaax5196. https://advances.sciencemag.org/lookup/doi/10.1126/sciadv.aax5196 (2019).

13. Ribeiro, R. F., Martínez-Martínez, L. A., Du, M., Campos-Gonzalez-Angulo, J. & Yuen-Zhou, J. Polariton chemistry: Controlling molecular dynamics with optical cavities. *Chemical Science* **9,** 6325–6339. https://pubs.rsc.org/en/content/articlelanding/2018/sc/c8sc01043a (2018).

14. Dorfman, K. E., Schlawin, F. & Mukamel, S. Nonlinear optical signals and spectroscopy with quantum light. *Reviews of Modern Physics* **88,** 045008. https://link.aps.org/doi/10.1103/RevModPhys.88.045008 (2016).

15. Kuzmich, A. & Mandel, L. Sub-shot-noise interferometric measurements with two-photon states. *Quantum and Semiclassical Optics: Journal of the European Optical Society Part B* **10,** 493–500. http://stacks.iop.org/1355-5111/10/i=3/a=008?key=crossref.fd33afd748cabc2e17dfba547b16192e (1998).

16. Slussarenko, S. *et al.* Unconditional violation of the shot-noise limit in photonic quantum metrology. *Nature Photonics* **11,** 700–703. https://www.nature.com/articles/s41566-017-0011-5 (2017).

17. Brida, G., Genovese, M. & Ruo Berchera, I. Experimental realization of sub-shot-noise quantum imaging. *Nature Photonics* **4,** 227–230. https://www.nature.com/articles/nphoton.2010.29 (2010).

18. Hosten, O., Engelsen, N. J., Krishnakumar, R. & Kasevich, M. A. Measurement noise 100 times lower than the quantum-projection limit using entangled atoms. *Nature* **529,** 505–508. https://www.nature.com/articles/nature16176 (2016).

19. Giovannetti, V., Lloyd, S. & Maccone, L. Quantum-Enhanced Measurements: Beating the Standard Quantum Limit. *Science* **306,** 1330–1336. https://www-science-org.caltech.idm.oclc.org/doi/full/10.1126/science.1104149 (2004).

20. Oka, H. Enhanced vibrational-mode-selective two-step excitation using ultrabroadband frequency-entangled photons. *Physical Review A* **97,** 063859. https://link.aps.org/doi/10.1103/PhysRevA.97.063859 (2018).

21. Oka, H. Selective two-photon excitation of a vibronic state by correlated photons. *The Journal of Chemical Physics* **134,** 124313. http://aip.scitation.org/doi/10.1063/1.3573565 (2011).

22. Schlawin, F., Dorfman, K. E., Fingerhut, B. P. & Mukamel, S. Manipulation of two-photon-induced fluorescence spectra of chromophore aggregates with entangled photons: A simulation study. *Physical Review A* **86,** 023851. https://link.aps.org/doi/10.1103/PhysRevA.86.023851 (2012).

23. Schlawin, F., Dorfman, K. E. & Mukamel, S. Entangled Two-Photon Absorption Spectroscopy. *Accounts of Chemical Research* **51,** 2207–2214. https://doi.org/10.1021/acs.accounts.8b00173 (2018).

24. Bittner, E. R., Li, H., Piryatinski, A., Srimath Kandada, A. R. & Silva, C. Probing exciton/exciton interactions with entangled photons: Theory. *The Journal of Chemical Physics* **152,** 071101. https://aip.scitation.org/doi/10.1063/1.5139197 (2020).

25. Buscemi, F., Bordone, P. & Bertoni, A. Entanglement dynamics of electron-electron scattering in low-dimensional semiconductor systems. *Physical Review A* **73,** 052312. https://link.aps.org/doi/10.1103/PhysRevA.73.052312 (2006).

26. Huang, Z. & Kais, S. Entanglement as measure of electron–electron correlation in quantum chemistry calculations. *Chemical Physics Letters* **413,** 1–5. https://www.sciencedirect.com/science/article/pii/S0009261405010651 (2005).

27. Eshun, A., Cai, Z., Awies, M., Yu, L. & T. Goodson, I. I. I. Investigations of Thienoacene Molecules for Classical and Entangled Two-Photon Absorption. *The Journal of Physical Chemistry A* (2018).

28. Guzman, A. R., Harpham, M. R., Suzer, O., Haley, M. M. & Goodson, T. G. Spatial Control of Entangled Two-Photon Absorption with Organic Chromophores. *Journal of the American Chemical Society* **132,** 7840–7841. https://doi.org/10.1021/ja1016816 (2010).

29. Harpham, M. R., Suzer, O., Ma, C.-Q., Bauerle, P. & Goodson, T. Thiophene Dendrimers as Entangled Photon Sensor Materials. *Journal of the American Chemical Society* **131,** 973–979. https://doi.org/10.1021/ja803268s (2009).

30. Varnavski, O., Pinsky, B. & Goodson, T. Entangled Photon Excited Fluorescence in Organic Materials: An Ultrafast Coincidence Detector. *The Journal of Physical Chemistry Letters* **8,** 388–393. https://doi.org/10.1021/acs.jpclett.6b02378 (2017).

31. Villabona-Monsalve, J. P., Varnavski, O., Palfey, B. A. & Goodson, T. I. Two-Photon Excitation of Flavins and Flavoproteins with Classical and Quantum Light. *Journal of the American Chemical Society* **140,** 14562–14566. https://doi.org/10.1021/jacs.8b08515 (2018).

32. Tabakaev, D. *et al.* Energy-time-entangled two-photon molecular absorption. *Physical Review A* **103,** 033701. https://link.aps.org/doi/10.1103/PhysRevA.103.033701 (2021).

33. Villabona-Monsalve, J. P., Calderón-Losada, O., Nuñez Portela, M. & Valencia, A. Entangled Two Photon Absorption Cross Section on the 808 nm Region for the Common Dyes Zinc Tetraphenylporphyrin and Rhodamine B. *The Journal of Physical Chemistry A* **121,** 7869–7875. https://doi.org/10.1021/acs.jpca.7b06450 (2017).

34. Hong, C. K., Ou, Z. Y. & Mandel, L. Measurement of subpicosecond time intervals between two photons by interference. *Physical Review Letters* **59,** 2044–2046. https://link.aps.org/doi/10.1103/PhysRevLett.59.2044 (1987).

35. Galvez, E. J. *et al.* Interference with correlated photons: Five quantum mechanics experiments for undergraduates. *American Journal of Physics* **73,** 127–140. https://aapt.scitation.org/doi/10.1119/1.1796811 (2005).

36. Gianani, I. Robust spectral phase reconstruction of time-frequency entangled bi-photon states. *Physical Review Research* **1,** 033165. https://link.aps.org/doi/10.1103/PhysRevResearch.1.033165 (2019).

37. Kalashnikov, D. A. *et al.* Quantum interference in the presence of a resonant medium. *Scientific Reports* **7,** 1–8. https://www.nature.com/articles/s41598-017-11694-z (2017).

38. Scully, M. O. & Zubairy, M. S. *Quantum Optics* ISBN: 978-0-521-43595-6. https://www.cambridge.org/core/books/quantum-optics/08DC53888452CBC6CDC0FD8A1A1A4DD7 (Cambridge University Press, Cambridge, 1997).

39. Lavoie, J. *et al.* Phase-Modulated Interferometry, Spectroscopy, and Refractometry using Entangled Photon Pairs. *Advanced Quantum Technologies* **3,** 1900114. http://onlinelibrary.wiley.com/doi/abs/10.1002/qute.201900114 (2020).

40. Barreiro, J. T., Langford, N. K., Peters, N. A. & Kwiat, P. G. Generation of Hyperentangled Photon Pairs. *Physical Review Letters* **95,** 260501. https://link.aps.org/doi/10.1103/PhysRevLett.95.260501 (2005).

41. Kwiat, P. G. Hyper-entangled states. *Journal of Modern Optics* **44,** 2173–2184. https://www.tandfonline.com/doi/abs/10.1080/09500349708231877 (1997).

42. Trojek, P., Schmid, C., Bourennane, M., Weinfurter, H. & Kurtsiefer, C. Compact source of polarization-entangled photon pairs. *Optics Express* **12,** 276–281. https://www.osapublishing.org/oe/abstract.cfm?uri=oe-12-2-276 (2004).

43. Volz, J., Kurtsiefer, C. & Weinfurter, H. Compact all-solid-state source of polarization-entangled photon pairs. *Applied Physics Letters* **79,** 869–871. http://aip.scitation.org/doi/10.1063/1.1389835 (2001).

44. Fejer, M. M. in *Guided Wave Nonlinear Optics* (eds Ostrowsky, D. B. & Reinisch, R.) 133–145 (Springer Netherlands, Dordrecht, 1992). ISBN: 978-94-011-2536-9. https://doi.org/10.1007/978-94-011-2536-9_9.

45. Armstrong, J. A., Bloembergen, N., Ducuing, J. & Pershan, P. S. Interactions between Light Waves in a Nonlinear Dielectric. *Physical Review* **127,** 1918–1939. https://link.aps.org/doi/10.1103/PhysRev.127.1918 (1962).

46. Byer, R. L. Quasi-Phasematched Nonlinear Interactions and Devices. *Journal of Nonlinear Optical Physics & Materials* **06,** 549–592. https://www.worldscientific.com/doi/10.1142/S021886359700040X (1997).

47. Jechow, A., Heuer, A. & Menzel, R. High brightness, tunable biphoton source at 976 nm for quantum spectroscopy. *Optics Express* **16,** 13439–13449. https://www.osapublishing.org/oe/abstract.cfm?uri=oe-16-17-13439 (2008).

48. Sensarn, S., Yin, G. Y. & Harris, S. E. Generation and Compression of Chirped Biphotons. *Physical Review Letters* **104,** 253602. https://link.aps.org/doi/10.1103/PhysRevLett.104.253602 (2010).

49. Harris, S. E. & Sensarn, S. *Toward Single-Cycle Biphotons* in *Conference on Coherence and Quantum Optics (2007), paper CMD1* (Optical Society of America, 2007), CMD1. https://www.osapublishing.org/abstract.cfm?uri=CQO-2007-CMD1.

50. Harris, S. E. Chirp and Compress: Toward Single-Cycle Biphotons. *Physical Review Letters* **98,** 063602. https://link.aps.org/doi/10.1103/PhysRevLett.98.063602 (2007).

51. Carrasco, S. *et al.* Enhancing the axial resolution of quantum optical coherence tomography by chirped quasi-phase matching. *Optics Letters* **29,** 2429–2431. https://www.osapublishing.org/ol/abstract.cfm?uri=ol-29-20-2429 (2004).

52. Hum, D. S. & Fejer, M. M. Quasi-phasematching. *Comptes Rendus Physique. Recent advances in crystal optics* **8,** 180–198. https://www.sciencedirect.com/science/article/pii/S1631070506002349 (2007).

53. León-Montiel, R. d. J., Svozilík, J., Torres, J. P. & U'Ren, A. B. Temperature-Controlled Entangled-Photon Absorption Spectroscopy. *Physical Review Letters* **123,** 023601. https://link.aps.org/doi/10.1103/PhysRevLett.123.023601 (2019).

54. Nasr, M. B. *et al.* Ultrabroadband Biphotons Generated via Chirped Quasi-Phase-Matched Optical Parametric Down-Conversion. *Physical Review Letters* **100,** 183601. https://link.aps.org/doi/10.1103/PhysRevLett.100.183601 (2008).

55. Lubin, G. *et al.* Quantum correlation measurement with single photon avalanche diode arrays. *Optics Express* **27,** 32863–32882. https://www.osapublishing.org/oe/abstract.cfm?uri=oe-27-23-32863 (2019).

56. Reichert, M., Defienne, H. & Fleischer, J. W. Massively Parallel Coincidence Counting of High-Dimensional Entangled States. *Scientific Reports* **8,** 7925. http://www.nature.com/articles/s41598-018-26144-7 (2018).

57. Moreau, P.-A., Mougin-Sisini, J., Devaux, F. & Lantz, E. Realization of the purely spatial Einstein-Podolsky-Rosen paradox in full-field images of spontaneous parametric down-conversion. *Physical Review A* **86,** 010101. https://link.aps.org/doi/10.1103/PhysRevA.86.010101 (2012).

58. Edgar, M. P. *et al.* Imaging high-dimensional spatial entanglement with a camera. *Nature Communications* **3,** 1–6. https://www.nature.com/articles/ncomms1988 (2012).

59. Abouraddy, A. F., Yarnall, T. M. & Di Giuseppe, G. Phase-unlocked Hong-Ou-Mandel interferometry. *Physical Review A* **87,** 062106. https://link.aps.org/doi/10.1103/PhysRevA.87.062106 (2013).

60. Kalashnikov, D. A., Paterova, A. V., Kulik, S. P. & Krivitsky, L. A. Infrared spectroscopy with visible light. *Nature Photonics* **10,** 98–101. https://www.nature.com/articles/nphoton.2015.252 (2016).

61. Lindner, C., Wolf, S., Kiessling, J. & Kühnemann, F. Fourier transform infrared spectroscopy with visible light. *Optics Express* **28,** 4426–4432. https://www.osapublishing.org/oe/abstract.cfm?uri=oe-28-4-4426 (2020).

62. Kviatkovsky, I., Chrzanowski, H. M., Avery, E. G., Bartolomaeus, H. & Ramelow, S. Microscopy with undetected photons in the mid-infrared. *Science Advances.* https://www.science.org/doi/abs/10.1126/sciadv.abd0264 (2020).

63. Kalachev, A. A. *et al.* Biphoton spectroscopy of YAG:Er3+ crystal. *Laser Physics Letters* **4,** 722. https://iopscience.iop.org/article/10.1002/lapl.200710061/meta (2007).

64. Kalachev, A. A. *et al.* Biphoton spectroscopy in a strongly nondegenerate regime of SPDC. *Laser Physics Letters* **5,** 600–602. https://onlinelibrary.wiley.com/doi/abs/10.1002/lapl.200810044 (2008).

65. Yabushita, A. & Kobayashi, T. Spectroscopy by frequency entangled photon pairs. *Physical Review A* **69,** 013806. http://arxiv.org/abs/quant-ph/0306154 (2004).

66. Paterova, A., Yang, H., An, C., Kalashnikov, D. & Krivitsky, L. Measurement of infrared optical constants with visible photons. *New Journal of Physics* **20,** 043015. https://doi.org/10.1088%2F1367-2630%2Faab5ce (2018).

67. Adams, B. W. *et al.* X-ray quantum optics. *Journal of Modern Optics* **60,** 2–21. https://doi.org/10.1080/09500340.2012.752113 (2013).

68. Shwartz, S. & Harris, S. E. Polarization Entangled Photons at X-Ray Energies. *Physical Review Letters* **106,** 080501. https://link.aps.org/doi/10.1103/PhysRevLett.106.080501 (2011).

69. Padgett, M. J. & Boyd, R. W. An introduction to ghost imaging: quantum and classical. *Philosophical Transactions of the Royal Society A: Mathematical, Physical and Engineering Sciences* **375,** 20160233. https://royalsocietypublishing.org/doi/10.1098/rsta.2016.0233 (2017).

70. Abouraddy, A. F., Stone, P. R., Sergienko, A. V., Saleh, B. E. A. & Teich, M. C. Entangled-Photon Imaging of a Pure Phase Object. *Physical Review Letters* **93,** 213903. https://link.aps.org/doi/10.1103/PhysRevLett.93.213903 (2004).

71. Bornman, N. *et al.* Ghost imaging using entanglement-swapped photons. *npj Quantum Information* **5,** 1–6. https://www.nature.com/articles/s41534-019-0176-5 (2019).

72. Pittman, T. B., Shih, Y. H., Strekalov, D. V. & Sergienko, A. V. Optical imaging by means of two-photon quantum entanglement. *Physical Review A* **52,** R3429–R3432. https://link.aps.org/doi/10.1103/PhysRevA.52.R3429 (1995).

73. Strekalov, D. V., Sergienko, A. V., Klyshko, D. N. & Shih, Y. H. Observation of Two-Photon "Ghost" Interference and Diffraction. *Physical Review Letters* **74,** 3600–3603. https://link.aps.org/doi/10.1103/PhysRevLett.74.3600 (1995).

74. Aspden, R. S., Tasca, D. S., Boyd, R. W. & Padgett, M. J. EPR-based ghost imaging using a single-photon-sensitive camera. *New Journal of Physics* **15,** 073032. https://doi.org/10.1088%2F1367-2630%2F15%2F7%2F073032 (2013).

75. Lane, T. J., Lane, T. J., Ratner, D. & Ratner, D. What are the advantages of ghost imaging? Multiplexing for x-ray and electron imaging. *Optics Express* **28,** 5898–5918. https://www.osapublishing.org/oe/abstract.cfm?uri=oe-28-5-5898 (2020).

76. Teich, M. C., Saleh, B. E. A., Wong, F. N. C. & Shapiro, J. H. Variations on the theme of quantum optical coherence tomography: a review. *Quantum Information Processing* **11,** 903–923. https://doi.org/10.1007/s11128-011-0266-6 (2012).

77. Mazurek, M. D., Schreiter, K. M., Prevedel, R., Kaltenbaek, R. & Resch, K. J. Dispersion-cancelled biological imaging with quantum-inspired interferometry. *Scientific Reports* **3,** 1–5. https://www.nature.com/articles/srep01582 (2013).

78. Okano, M. *et al.* 0.54 μm resolution two-photon interference with dispersion cancellation for quantum optical coherence tomography. *Scientific Reports* **5,** 18042. https://www.nature.com/articles/srep18042 (2015).

79. Giovannetti, V., Lloyd, S. & Maccone, L. Advances in quantum metrology. *Nature Photonics* **5,** 222–229. https://www.nature.com/articles/nphoton.2011.35 (2011).

80. Xiang, G. Y., Higgins, B. L., Berry, D. W., Wiseman, H. M. & Pryde, G. J. Entanglement-enhanced measurement of a completely unknown optical phase. *Nature Photonics* **5,** 43–47. https://www.nature.com/articles/nphoton.2010.268 (2011).

81. Okamoto, R. *et al.* Beating the standard quantum limit: Phase super-sensitivity of N-photon interferometers. *New Journal of Physics* **10,** 073033. https://doi.org/10.1088%2F1367-2630%2F10%2F7%2F073033 (2008).

82. Stefanov, A. On the role of entanglement in two-photon metrology. *Quantum Science and Technology* **2,** 025004. https://doi.org/10.1088/2058-9565/aa6ae1 (2017).

83. Raymer, M. G., Marcus, A. H., Widom, J. R. & Vitullo, D. L. P. Entangled Photon-Pair Two-Dimensional Fluorescence Spectroscopy (EPP-2DFS). *The Journal of Physical Chemistry B* **117,** 15559–15575. https://doi.org/10.1021/jp405829n (2013).

84. Otten, M., Kenneweg, T., Hensen, M., Gray, S. K. & Pfeiffer, W. Coherent photon coincidence spectroscopy of single quantum systems. *Physical Review A* **102,** 043118. https://link.aps.org/doi/10.1103/PhysRevA.102.043118 (2020).

85. Roslyak, O. & Mukamel, S. Multidimensional pump-probe spectroscopy with entangled twin-photon states. *Physical Review A* **79,** 063409. https://link.aps.org/doi/10.1103/PhysRevA.79.063409 (2009).

86. Li, R. L. *et al.* Controlled growth of imine-linked two-dimensional covalent organic framework nanoparticles. *Chemical Science* **10,** 3796–3801. https://pubs.rsc.org/en/content/articlelanding/2019/sc/c9sc00289h (2019).

87. Lachance-Quirion, D. *et al.* Entanglement-based single-shot detection of a single magnon with a superconducting qubit. *Science* **367,** 425–428. https://science.sciencemag.org/content/367/6476/425 (2020).

88. Dayan, B., Pe'er, A., Friesem, A. A. & Silberberg, Y. Two Photon Absorption and Coherent Control with Broadband Down-Converted Light. *Physical Review Letters* **93,** 023005. https://link.aps.org/doi/10.1103/PhysRevLett.93.023005 (2004).

89. Schlawin, F., Dorfman, K. E., Fingerhut, B. P. & Mukamel, S. Suppression of population transport and control of exciton distributions by entangled photons. *Nature Communications* **4,** 1–7. https://www.nature.com/articles/ncomms2802 (2013).

90. Lever, F., Ramelow, S. & Gühr, M. Effects of time-energy correlation strength in molecular entangled photon spectroscopy. *Physical Review A* **100,** 053844. https://link.aps.org/doi/10.1103/PhysRevA.100.053844 (2019).

91. Oka, H. Entangled two-photon absorption spectroscopy for optically forbidden transition detection. *The Journal of Chemical Physics* **152,** 044106. https://doi.org/10.1063/1.5138691 (2020).

92. Bergli, J., Adenier, G., Thörn, A. P. & Vistnes, A. I. Frequency and phase relations of entangled photons observed by a two-photon interference experiment. *Physical Review A* **100,** 023850. https://link.aps.org/doi/10.1103/PhysRevA.100.023850 (2019).

93. Burdick, R. K. *et al.* Predicting and Controlling Entangled Two-Photon Absorption in Diatomic Molecules. *The Journal of Physical Chemistry A* **122,** 8198–8212. https://doi.org/10.1021/acs.jpca.8b07466 (2018).

94. Pirandola, S., Bardhan, B. R., Gehring, T., Weedbrook, C. & Lloyd, S. Advances in photonic quantum sensing. *Nature Photonics* **12,** 724–733. https://www.nature.com/articles/s41566-018-0301-6 (2018).

95. Fan, W., Lawrie, B. J. & Pooser, R. C. Quantum plasmonic sensing. *Physical Review A* **92,** 053812. https://link.aps.org/doi/10.1103/PhysRevA.92.053812 (2015).

96. Pooser, R. C. & Lawrie, B. Plasmonic Trace Sensing below the Photon Shot Noise Limit. *ACS Photonics* **3,** 8–13. https://doi.org/10.1021/acsphotonics.5b00501 (2016).

97. Lee, C. L. D. & Hewitt, K. C. First demonstration of surface enhanced-stimulated Raman spectroscopy (SE-SRS) using low-power CW sources. *Faraday Discussions* **205,** 227–232. http://xlink.rsc.org/?DOI=C7FD00137A (2017).

98. Oka, H. Highly-efficient entangled two-photon absorption with the assistance of plasmon nanoantenna. *Journal of Physics B: Atomic, Molecular and Optical Physics* **48,** 115503. https://doi.org/10.1088%2F0953-4075%2F48%2F11%2F115503 (2015).

99. Osaka, Y., Yokoshi, N., Nakatani, M. & Ishihara, H. Enhanced Up-Conversion of Entangled Photons and Quantum Interference under a Localized Field in Nanostructures. *Physical Review Letters* **112,** 133601. https://link.aps.org/doi/10.1103/PhysRevLett.112.133601 (2014).

100. Basiri-Esfahani, S., Myers, C. R., Armin, A., Combes, J. & Milburn, G. J. Integrated quantum photonic sensor based on Hong-Ou-Mandel interference. *Optics Express* **23,** 16008–16023. https://www.osapublishing.org/oe/abstract.cfm?uri=oe-23-12-16008 (2015).

101. Lee, Y.-S., Lee, S. M., Kim, H. & Moon, H. S. Highly bright photon-pair generation in Doppler-broadened ladder-type atomic system. *Optics Express* **24,** 28083. http://arxiv.org/abs/1609.02378 (2016).

102. Kalashnikov, D. A., Pan, Z., Kuznetsov, A. I. & Krivitsky, L. A. Quantum Spectroscopy of Plasmonic Nanostructures. *Physical Review X* **4,** 011049. https://link.aps.org/doi/10.1103/PhysRevX.4.011049 (2014).

103. Roslyak, O., Marx, C. A. & Mukamel, S. Nonlinear spectroscopy with entangled photons: Manipulating quantum pathways of matter. *Physical Review A* **79,** 033832. https://link.aps.org/doi/10.1103/PhysRevA.79.033832 (2009).

104. Avanaki, K. N. & Schatz, G. C. Entangled Photon Resonance Energy Transfer in Arbitrary Media. *The Journal of Physical Chemistry Letters* **10,** 3181–3188. https://doi.org/10.1021/acs.jpclett.9b00902 (2019).

105. Pan, J.-W. *et al.* Multiphoton entanglement and interferometry. *Reviews of Modern Physics* **84,** 777–838. https://link.aps.org/doi/10.1103/RevModPhys.84.777 (2012).

106. Mukamel, S. *et al.* Roadmap on Quantum Light Spectroscopy. *Journal of Physics B: Atomic, Molecular and Optical Physics.* http://iopscience.iop.org/10.1088/1361-6455/ab69a8 (2020).

107. Gao, W. B., Fallahi, P., Togan, E., Miguel-Sanchez, J. & Imamoglu, A. Observation of entanglement between a quantum dot spin and a single photon. *Nature* **491,** 426–430. https://www.nature.com/articles/nature11573 (2012).

108. Bayer, M. *et al.* Coupling and Entangling of Quantum States in Quantum Dot Molecules. *Science* **291,** 451–453. https://www.science.org/doi/10.1126/science.291.5503.451 (2001).

109. Lee, K. C. *et al.* Entangling Macroscopic Diamonds at Room Temperature. *Science* **334,** 1253–1256. http://science.sciencemag.org/content/334/6060/1253 (2011).

110. Muthukrishnan, A., Agarwal, G. S. & Scully, M. O. Inducing Disallowed Two-Atom Transitions with Temporally Entangled Photons. *Physical Review Letters* **93,** 093002. https://link.aps.org/doi/10.1103/PhysRevLett.93.093002 (2004).

111. Prochaska, L. *et al.* Singular charge fluctuations at a magnetic quantum critical point. *Science* **367,** 285–288. https://www.science.org/doi/10.1126/science.aag1595 (2020).

112. Bouwmeester, D. & Zeilinger, A. in *The Physics of Quantum Information: Quantum Cryptography, Quantum Teleportation, Quantum Computation* (eds Bouwmeester, D., Ekert, A. & Zeilinger, A.) 1–14 (Springer, Berlin, Heidel-

berg, 2000). ISBN: 978-3-662-04209-0. https://doi.org/10.1007/978-3-662-04209-0_1.

113. Kimble, H. J. The quantum internet. *Nature* **453,** 1023–1030. https://www.nature.com/articles/nature07127 (2008).

114. Chang, D. E., Douglas, J. S., González-Tudela, A., Hung, C.-L. & Kimble, H. J. Colloquium: Quantum matter built from nanoscopic lattices of atoms and photons. *Reviews of Modern Physics* **90,** 031002. https://link.aps.org/doi/10.1103/RevModPhys.90.031002 (2018).

115. Keimer, B. & Moore, J. E. The physics of quantum materials. *Nature Physics* **13,** 1045–1055. https://www.nature.com/articles/nphys4302 (2017).

116. Jones, R. O. Density functional theory: Its origins, rise to prominence, and future. *Reviews of Modern Physics* **87,** 897–923. https://link.aps.org/doi/10.1103/RevModPhys.87.897 (2015).

117. Scalapino, D. J. A common thread: The pairing interaction for unconventional superconductors. *Reviews of Modern Physics* **84,** 1383–1417. https://link.aps.org/doi/10.1103/RevModPhys.84.1383 (2012).

118. Löhneysen, H. v., Rosch, A., Vojta, M. & Wölfle, P. Fermi-liquid instabilities at magnetic quantum phase transitions. *Reviews of Modern Physics* **79,** 1015–1075. https://link.aps.org/doi/10.1103/RevModPhys.79.1015 (2007).

119. Basov, D. N., Averitt, R. D., van der Marel, D., Dressel, M. & Haule, K. Electrodynamics of correlated electron materials. *Reviews of Modern Physics* **83,** 471–541. https://link.aps.org/doi/10.1103/RevModPhys.83.471 (2011).

120. Bloch, I., Dalibard, J. & Nascimbène, S. Quantum simulations with ultracold quantum gases. *Nature Physics* **8,** 267–276. https://www.nature.com/articles/nphys2259 (2012).

121. Dorfman, K. E. & Mukamel, S. Multidimensional spectroscopy with entangled light: loop vs ladder delay scanning protocols. *New Journal of Physics* **16,** 033013. https://doi.org/10.1088%2F1367-2630%2F16%2F3%2F033013 (2014).

122. Altuzarra, C. *et al.* Coherent Perfect Absorption in Metamaterials with Entangled Photons. *ACS Photonics* **4,** 2124–2128. https://doi.org/10.1021/acsphotonics.7b00514 (2017).

123. Li, Y., Nemilentsau, A. & Argyropoulos, C. Resonance energy transfer and quantum entanglement mediated by epsilon-near-zero and other plasmonic waveguide systems. *Nanoscale* **11,** 14635–14647. https://pubs.rsc.org/en/content/articlelanding/2019/nr/c9nr05083c (2019).

124. Basov, D. N., Averitt, R. D. & Hsieh, D. Towards properties on demand in quantum materials. *Nature Materials* **16,** 1077–1088. https://www.nature.com/articles/nmat5017 (2017).

125. Mak, K. F., He, K., Shan, J. & Heinz, T. F. Control of valley polarization in monolayer MoS2 by optical helicity. *Nature Nanotechnology* **7,** 494–498. https://www.nature.com/articles/nnano.2012.96 (2012).

126. Xu, X., Yao, W., Xiao, D. & Heinz, T. F. Spin and pseudospins in layered transition metal dichalcogenides. *Nature Physics* **10,** 343–350. https://www.nature.com/articles/nphys2942 (2014).

127. Boto, A. N. *et al.* Quantum Interferometric Optical Lithography: Exploiting Entanglement to Beat the Diffraction Limit. *Physical Review Letters* **85,** 2733–2736. https://link.aps.org/doi/10.1103/PhysRevLett.85.2733 (2000).

Chapter 3

DESIGNING HIGH-POWER, OCTAVE SPANNING ENTANGLED PHOTON SOURCES FOR QUANTUM SPECTROSCOPY

ABSTRACT

Entangled photon spectroscopy is a nascent field that has important implications for measurement and imaging across chemical, biology, and materials fields. Entangled photon spectroscopy potentially offers improved spatial and temporal-frequency resolutions, increased cross sections for multiphoton and nonlinear measurements, and new abilities in inducing or measuring quantum correlations. A critical step in enabling entangled photon spectroscopies is the creation of high-flux entangled sources that can use conventional detectors, as well as provide redundancy for the losses in realistic samples. Here, we report a periodically poled, chirped, lithium tantalate platform that generates entangled photon pairs with a $\sim 10^{-7}$ efficiency. For a near watt level diode laser, this results in a near μW-level flux. The single photon per mode limit that is necessary to maintain non-classical photon behavior is still satisfied by distributing this power over up to an octave-spanning bandwidth. The spectral-temporal photon correlations are observed via a Michelson-type interferometer that measures the broadband Hong-Ou-Mandel two-photon interference. A coherence time of 245 fs for a 10 nm bandwidth in the collinear case and a 62 fs for a 125 nm bandwidth in the non-collinear case is measured using a CW pump laser, and, essentially, collecting the full photon cone. We outline in detail the numerical methods used for designing and tailoring the entangled photons source, such as changing center wavelength or bandwidth, with the ultimate aim of increasing the availability of high-flux UV-Vis entangled photon sources in the optical spectroscopy community.

Most of this chapter has been reproduced with permission from:

Szoke, S. *et al.* Designing High-Power, oOctave Spanning Entangled Photon Sources for Quantum Spectroscopy. *The Journal of Chemical Physics* **154,** 244201. `https://aip.scitation.org/doi/10.1063/5.0053688` (2021).

3.1 Introduction

An entangled photon pair is generated by splitting a single photon into two photons via spontaneous parametric down conversion (SPDC) [1]. The quantum correlations between the two photons have several effects. First, when coherently recombined in time and space, the two entangled photons behave as the initial pump photon. In other words, the two entangled photons can be thought of as acting like a single photon in light-matter interactions [2]. As a result, two entangled photons leave the same side of a beamsplitter [3] and diffract from a grating at the wavelength of the pump photon [4–6]. Entangled photon pairs also linearize multiphoton and nonlinear spectroscopy, as has been well-studied in two-photon absorption and fluorescence [7–13]. Entangled photons also have non-Fourier reciprocal spectral-temporal resolutions and are able to yield spatial resolutions which scale inversely with the number of correlated entangled photons N [14–18].

These properties, plus the more well known sub-shot noise and classical light rejection behaviors, make entangled photons tempting for use in ultrafast laser spectroscopy [19, 20]. The fragility of the entangled states, and the difficulty and expense associated with single photon counting, necessitates a need for high flux (nW-μW) entangled photon sources that would easily interface with existing ultrafast optics setups [21]. However, commonly used nonlinear crystals (BBO, KDP), usually have entangled photon creation efficiencies in the 10^{-10} to 10^{-12} range [22–24]. Reliance on 'birefringent phase matching' limits the highest usable nonlinear coefficients of the crystal as well as the bandwidth of entangled photons that can be created [25–27]. The possible phase-matching conditions result in bandwidths in the tens of nanometers range, which corresponds to 100s of femtoseconds to picoseconds in correlation times in experiments. Given the current assumption that the entangled photon correlation time must be less than a molecule or material's de-phasing time to allow a nonlinear or multiphoton enhancement, the narrow bandwidth of birefringent phase matching presents critical limits on entangled spectroscopy's feasibility [19, 28, 29].

In contrast, the ferroelectric properties of materials such as KTP and lithium niobate allow the crystals to be periodically poled and utilize a 'quasi phase-matching' (QPM) technique [30–32]. Quasi-phase-matching allows the use of Type-0 collinear phase matching [33], SPDC efficiencies of 10^{-6} to 10^{-10} [34, 35], a broadly tunable center wavelength (set by the grating period instead of crystal angle) [36], and easy implementation of waveguides that can saturate single photon detectors with

~mW of CW diode laser input power [37]. Broad bandwidth phase matching is achieved by introducing a chirp into the poling period of the structure. The nonlinear poling allows for more wavelengths to be phase matched, while also retaining the benefits associated with longer crystals, namely a larger downconverted photon flux. The increased bandwidth directly affects the effective temporal resolution of experiments [38–40].The broad bandwidth also allows increased power densities, as the the single photon per wavelength mode occupation limit necessary for non-classical effects is not exceeded (calculated as the flux in photons/s divided by the bandwidth in Hz) [41, 42]. While KTP and lithium niobate have been the primary workhorse for entangled photon generation in quantum information system settings, they have limitations with regards to their damage thresholds and UV cut-offs. In contrast, lithium tantalate is more ideal for physical chemistry and materials research because it has higher power handling capabilities (240 MW/cm^2) [43] and a lower UV absorption edge ($\approx$ 280 nm) [44, 45].

To accelerate the adoption of entangled photon techniques, we outline how to create an entangled photon source that can achieve near μW powers of entangled photons down to UV wavelengths with temporal resolutions of tens of femtoseconds. These entangled photon fluxes are high enough to be visible by eye when starting from a 1W CW pump laser, greatly facilitating the alignment of entangled experiments. Here, the generated photon pairs are centered around a degenerate wavelength of 812 nm, resulting from a 406 nm pump source, but this wavelength can be tuned as outlined by the formulas in the paper. The 8% MgO doped congruent lithium tantalate (CLT) gratings use a Type-0, collinear quasi-phase matching configuration. A Michelson type interferometric scheme [46] measures the fourth-order interference of the entangled photons and gives coherence times of 245 fs for a bandwidth of 10 nm and 62 fs for a bandwidth of 125 nm. Of course, simply producing a broad bandwidth of entangled photons is not the same as carrying out experiments using them. We discuss our attempts to utilize the full SPDC cone and bandwidth in subsequent experiments, emphasizing where optics development is still needed to achieve maximum temporal resolution and flux. Using the full cone is in contrast to most experiments where irises are used to select two points from the SPDC cone, thereby severely reducing the total photon flux at the gain of state purity. The paper aims to give quick access to the sources needed for the emerging field of nonlinear entangled photon optics as well as outlining the next steps needed in the field.

3.2 Theory

Designing broadband SPDC in a chirped nonlinear materials

Prior to quantifying the experimental behavior of the SPDC sources, we lay out the theoretical and numerical details used in their design.

In SPDC, the creation of two entangled photons arises from the quantum mechanical process of a single pump photon mixing with the underlying vacuum state. The two down-converted daughter photons display strong correlations in time, energy, and momentum due to the parametric mixing process [1, 47]. The time and energy correlations originate from the individual photons being generated simultaneously from the pump photon:

$$E_p\left(\omega_p\right) = E_s\left(\omega_s\right) + E_i\left(\omega_i\right) \tag{3.1}$$

$$\therefore \;\; \omega_i = \omega_p - \omega_s \tag{3.2}$$

where ω_p, ω_s, and ω_i are the frequencies of the pump, signal, and idler photon, respectively. The momentum correlation is dictated by the phase matching condition, which is a consequence of the wave-like nature of the interacting fields. Each field has a corresponding wave vector defined via its respective phase velocity $v_p = c/n\left(\omega, T\right)$ in the medium:

$$k\left(\omega, T\right) = \frac{\omega n\left(\omega, T\right)}{c} \tag{3.3}$$

with $n\left(\omega, T\right)$ being the frequency and temperature dependent refractive index of the material. The following vector sum, the longitudinal component of which is depicted in Fig. 3.1, should be satisfied in order to ensure that a proper phase relationship between the interacting waves is maintained throughout the nonlinear crystal.

$$\begin{aligned}\Delta\boldsymbol{k}\left(\omega_p, \omega_s, \omega_i\right) = \boldsymbol{k}_p\left(\omega_p, n_p\left(\omega_p, T\right)\right) - \boldsymbol{k}_s\left(\omega_s, n_s\left(\omega_s, T\right)\right) \\ -\boldsymbol{k}_i\left(\omega_i, n_i\left(\omega_i, T\right)\right).\end{aligned} \tag{3.4}$$

It is only when this relationship holds true ($\Delta k = 0$) that constructive interference between the propagating waves can occur and energy is transferred dominantly in one direction, rather than oscillating back and forth between the two optical modes [48].

A natural extension of this phase-matching principle, termed quasi-phase-matching, is apparent if one considers the duality between position and momentum space.

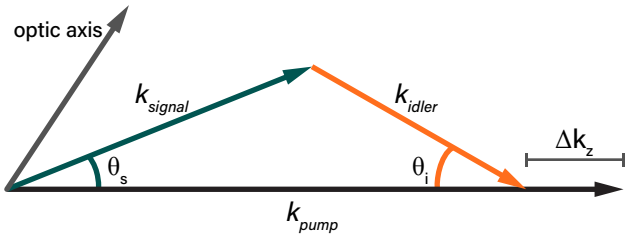

Figure 3.1: Phase-matching diagram for a two-photon down conversion process, showing the longitudinal phase-mismatch component Δk_z. The entangled photons (signal and idler) are each shown to have their distinct wave vectors k and emission angles θ. The phase-mismatch component must be compensated to create entangled photons by spontaneous parametric down conversion (SPDC).

A periodic lattice in position space directly corresponds to a well-defined wave vector $\boldsymbol{k}$ in momentum space via a Fourier transform. Therefore, if the nonlinear dielectric tensor domains of ferroelectric nonlinear crystal are modulated with a specific periodicity Λ, a quasi-momentum term $\Gamma(\Lambda)$ arises, which can be used to satisfy a non-phase-matched nonlinear interaction.

$$\Delta\tilde{\boldsymbol{k}}\left(\omega_p, \omega_s, \omega_i\right) = \Delta\boldsymbol{k}\left(\omega_p, \omega_s, \omega_i\right) - \Gamma(\Lambda) \tag{3.5}$$

The quasi-phase-matching term $\Gamma(\Lambda)$ also has an additional advantage, in that it can be chosen to be higher-*order*. Here, the order of the configuration is defined by m.

$$\Gamma(\Lambda) = \frac{2\pi m}{\Lambda},\ m \in 2\mathbb{Z} + 1\ (\neg 0) \tag{3.6}$$

This serves a particular experimental benefit as it allows for nonlinear interactions to be phase-matched (albeit with lower efficiency), even if the required 1^{st} order periodicity is too small to be fabricated [49].

We now describe the design of a grating in congruent lithium tantalate with the design goal of a 406 nm pump wavelength that creates a >400 nm bandwidth around the degenerate 812 nm SPDC point. The source must also be capable of creating near μW powers given a 1 W input power. The first step is to obtain the Sellmeier equations that describe the frequency and temperature dependent refractive indices of the material [50]. The numeric values and a representative plot are found in the supplementary information. Using the Sellmeier equations, the phase mismatch (Eq. 3.5) is then evaluated for a wide range of pump-signal/idler wavelength configurations while keeping one entangled photon frequency a constant. External conditions such as the desired temperature range and minimum achievable

poling periodicity are also enforced such that the parameter space remains within experimentally realistic boundaries. The root of Eq. 3.5 can then be found by a root-finding algorithm. For the congruent lithium tantalate and a 406-812 SPDC process, and imposing a realistic $< 200℃$ temperature condition, solving for the root of Eq. 3.5 yields a poling period of 9.5 μm at 133℃ (see fig. A.2 for the graphical solution).

Quasi-phase-matching is a strongly temperature dependent technique. By solving Eq. 3.5 for a range of temperatures near the calculated degeneracy point (133℃), the splitting and tuning of the SPDC spectrum can be calculated. Tuning the SPDC spectrum via the crystal temperature is useful for controlling what intermediate states are involved in, the magnitude of, and the temporal resolution of an entangled two photon process. The temperature dependent behavior is shown in Fig. 3.2. Here, the transition between the degenerate and non-degenerate domains is clearly observable, with lower temperatures corresponding to a weaker degenerate emission profile. The lower plot of Fig. 3.2 also clearly shows a very strong narrowing of the signal and idler bandwidths as one temperature tunes further away from degeneracy.

Additionally, both signal and idler have an inherent angular emission property determined by the momentum conservation condition in Eq. 3.5. The strong frequency dependence of the outgoing angles can be numerically calculated from the momentum conservation equation if one decomposes the wave vectors into their longitudinal and transverse components, and solves the trigonometric equations for transverse phase-matching. Subsequently computing the emission angle for each frequency of interest, in conjunction with the frequency dependent refractive index of the nonlinear crystal, the SPDC cone's spectral characteristic for various crystal temperatures can be plotted (Fig. 3.3). As predicted, at the degenerate emission temperature of 133℃, the plot shows that the emission angle of the 812 nm signal and idler photons is 0℃. More importantly however, comparing the results to those in Fig. 3.2, the shaded non-degenerate region also corresponds to a collinear emission profile. Vice versa, temperatures below 133℃ display a (albeit weak) degenerate, non-collinear character.

In a chirped crystal, the bandwidth of the down-converted entangled photons is increased by changing the poling period throughout the crystal. The increasing width elements correspond to different phase-matched wavelength configurations of Eq. 3.5 (Fig. 3.4). The photons still add up to the narrow linewidth of the pump laser but the temporal resolution is given by the temporal alignment and down-converted

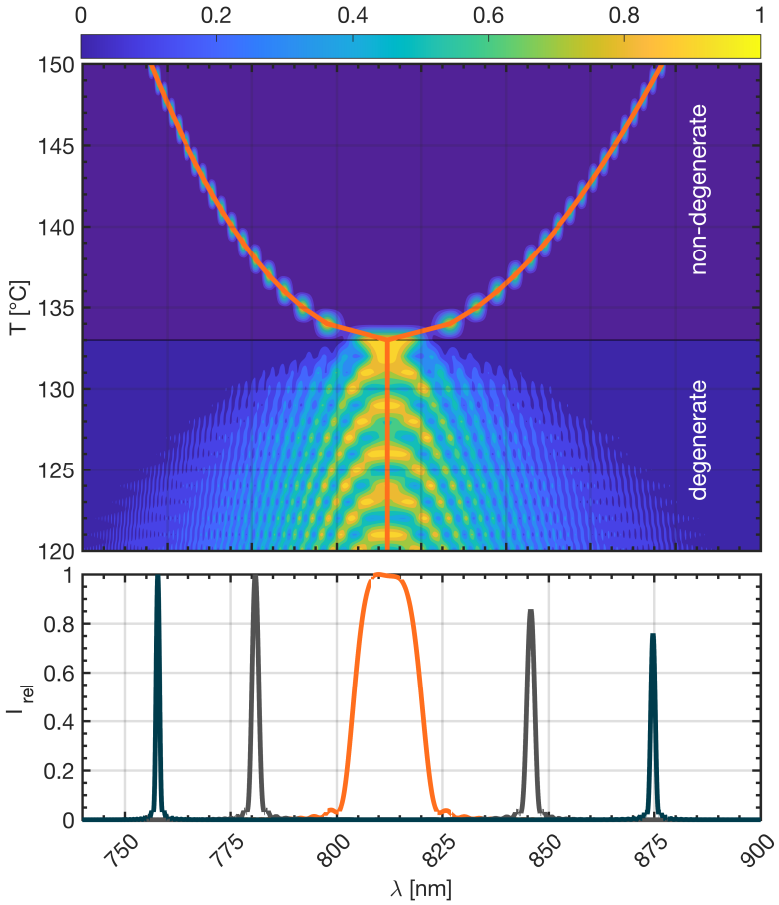

Figure 3.2: SPDC emission spectrum for ppCLT at various phase-matching temperatures showing transition from degenerate to non-degenerate down conversion. Bottom plot showing spectra at three temperatures corresponding to cross sections of the 2D plot. The phase matching temperature results in the broadest bandwidth.

bandwidth of the entangled photons. This is why entangled photon experiments are said to have independent spectral and temporal resolutions. The importance of the pump laser's linewidth in determining the entangled photon state's purity, and thus the access to non-classical spectroscopic properties, is discussed in the supplementary information.

Following a similar treatment to [51], the crystal can be decomposed into its individual domains, in each of which the downconversion amplitude follows the usual *sinc* function-like phase-matching dependence [52]. This is attributed to the Fourier transform of a rectangular function in real-space representing the probability of a downconversion event occurring inside the crystal element.

$$A_n\left(\omega_s, \omega_i\right) = L_n sinc\left(\frac{L_n \Delta k}{2}\right) \tag{3.7}$$

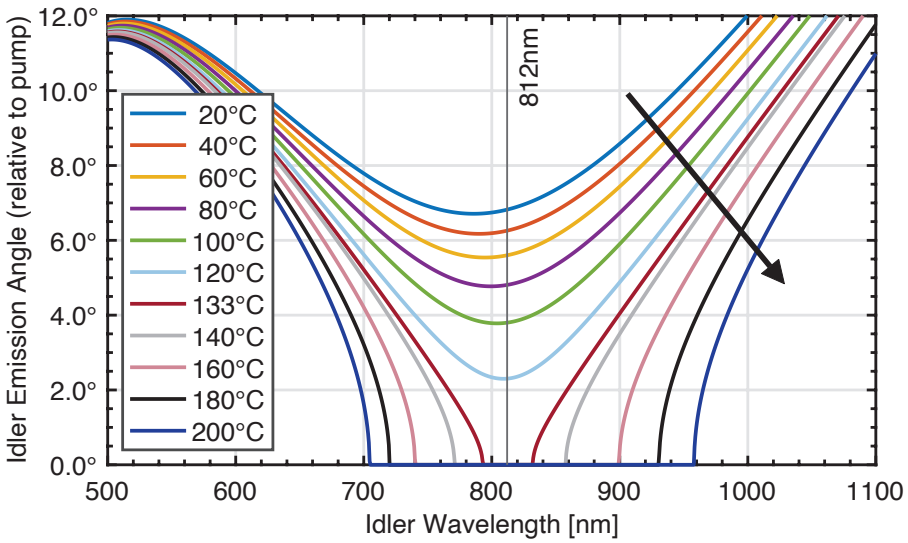

Figure 3.3: Broadband signal/idler emission angles in ppCLT with 9.5 μm poling period, showing how the SPDC source does not act as an ideal dipole emitter when broadband entangled photon pairs are desired. Points where curves reach a value of zero correspond to collinear, non-degenerate emission. Note that at certain temperatures, there need not be any SPDC emission in certain directions, governed by the spectral emission characteristics in Fig. 3.2. Arrow indicating direction of increasing temperature.

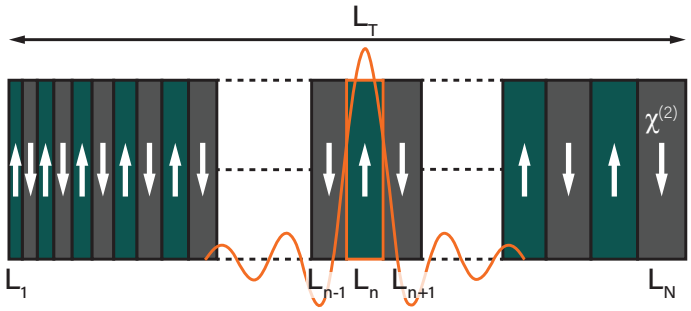

Figure 3.4: Depiction of a chirped periodically poled crystal with total length L_T. Each crystal segment of length L_n is associated with a *sinc*-shaped downconversion amplitude around a different center wavelength. Equivalently to a normal periodically poled crystal, the domain orientation is reversed in adjacent elements.

With L_n being the length of the n^{th} crystal element. Similarly, a cumulative-phase term can be defined, which is related to a forward propagating wave with phase-

mismatch Δk traversing a crystal length L_{prop} after it has been generated in the SPDC process at crystal element n.

$$\varphi = \Delta k L_{prop} = \Delta k \left(\frac{L_n}{2} + \sum_{m=n+1}^{N} L_m \right) \tag{3.8}$$

Carrying out a sum over all individual crystal elements then allows for the resulting SPDC spectrum to be calculated (Eq. 3.9) and thereby observe the effects of different chirping parameters. For lithium tantalate, this is shown in Fig. 3.5. In the case of CLT, a ±10% chirp around the degenerate poling periodicity calculated above yields a full octave spanning SPDC bandwidth. Trivially, in the limit of no chirp, where all crystal elements are equal in size, the solution for a periodically poled crystal of length L is recovered.

$$\begin{aligned} A\left(\omega_s, \omega_i\right) = \chi_0 \sum_{n=1}^{N} (-1)^n L_n sinc\left(\frac{L_n \Delta k}{2}\right) \\ \times e^{-i\Delta k\left(\frac{L_n}{2} + \sum_{m=n+1}^{N} L_m\right)}. \end{aligned} \tag{3.9}$$

By plotting the solution of Eq. 3.9 as a function of the position inside the crystal along the propagation direction, we can gain some intuition for how the constructive interference results in a broadened spectrum. In the case of CLT, a ±10% chirp around the degenerate poling periodicity calculated above yields a full octave spanning SPDC bandwidth as shown in Fig. 3.6. Here we used a total grating length of 18 mm equal to the chip used in subsequent experiments.

The 2D plot in Fig. 3.6 provides some additional insight into how modulation of the poling period affects the build-up of the emitted spectrum. In particular, it's important to note that while the first 8mm length of the crystal appears to show no downconversion taking place, this is indeed not the case. While all crystal elements in this region satisfy a particular phase-matching condition, it is only after a certain propagation length that the phases of each spectral mode coherently sum to a strong enough amplitude that would be perceivable on the plot. Furthermore, the broadening of the downconverted bandwidth does have a particular drawback, in that the frequencies close to degeneracy become weaker in intensity. This is best observed in the line cuts for positions L3 and L4, where instead of a constant intensity across all frequencies, the emission spectrum peaks at the lower and higher cut-offs but begins to droop more severely as the bandwidth increases. Thus, increasing the chirping of the poling period indefinitely does not necessarily yield a flat power

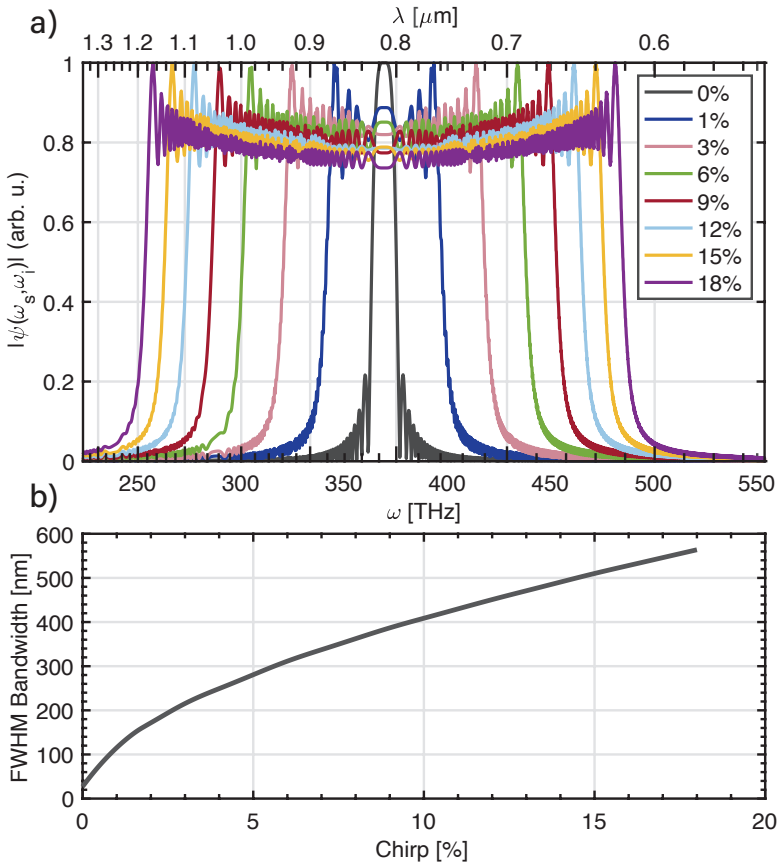

Figure 3.5: SPDC emission bandwidth broadening. (a) SPDC emission bandwidth broadening as a function of chirp parameter, defined as total percentage deviation from the degenerate poling period. (b) Numerically calculated FWHM bandwidth trend as a function of poling period chirp.

spectral density. It should be pointed out that this issue can be addressed via chirp profiles which follow not a linear but some higher order functional form [53].

In contrast to narrowband SPDC where the emission angles for the photon pairs are well confined within the two narrow arcs satisfying momentum conservation, such extremely broadband downconversion poses inherent difficulties in the spatial degree of freedom due angular (chromatic) dispersion of the resulting beam. As Fig. 3.3 shows, the emission angles increase quickly away from degeneracy. This presents several experimental issues, as the beam no longer represents an ideal point source, which will be discussed in the experimental section below. Taking into account the physical dimensions of the grating cross section (detailed in the experimental section below), it is easy to see that the output aperture of the grating can at most only accommodate $\arctan(0.15\text{ mm}/9\text{ mm}) \approx 1^\circ$ of emission in the

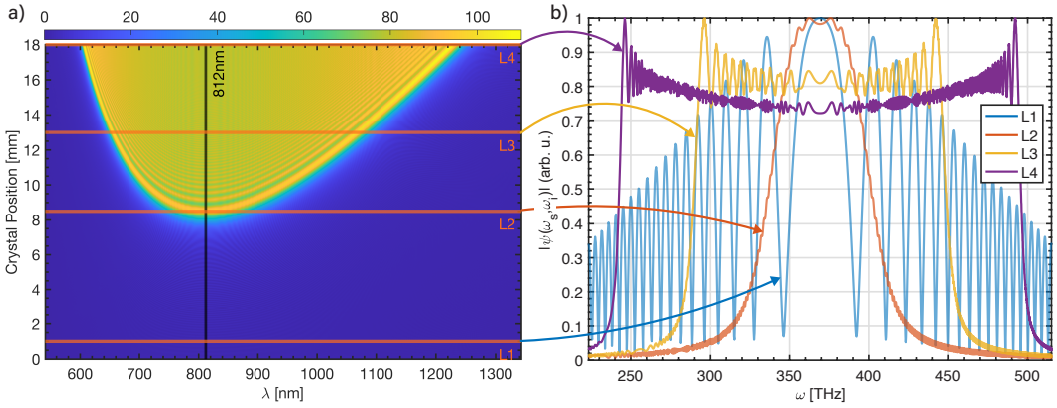

Figure 3.6: SPDC buildup in a ppCLT grating. (a) Build up of the collective SPDC spectrum as a function of the position inside a chirped ppCLT grating in the direction of propagation. (b) Line cuts across the 2D spectrum plot in (b) showing the normalized spectrum (in frequency space) at the positions designated as L1, L2, L3, and L4, respectively.

horizontal axis, and $\arctan(0.5\text{ mm}/9\text{ mm}) \approx 3.2°$ along the vertical axis relative to the center point of the crystal where we focus. Beyond this, large parts of the SPDC emission cone will begin to interact with the domain boundaries which form the grating channel. While in principle the refractive index is the same for both un-poled and poled crystal regions, the periodic poling process causes some stress at the domain walls. Therefore, the edge of the each pattern in the lateral direction acts as a kind of scattering center, possibly resulting in unwanted interference patterns. Therefore special attention should be paid to accommodate the spatial distribution of the cone as it diverges inside the channel.

A final point to consider is the total length of the grating is to be chosen by considering two interlinked criteria. Firstly, the expected power spectral density of the entangled photons at the output scales as L^2. Emission intensity can therefore be significantly increased by utilizing longer structures. Conversely, the expected power spectral density also depends on a $sinc\left(\frac{L_n \Delta k}{2}\right)$ multiplicative factor. Hence, longer gratings result in narrower emission bandwidths. This 'dual'-argument also applies to poling patterns which have a chirp, as while increasing the amount of variation in the poling periodicity serves to broaden the emission bandwidth, each spectral component will be less populated with photons and thus less brilliant. Particularly for entangled photon spectroscopy, the optimal flux is around the single photon per mode limit. Above this, the quantum and entangled effects will start to blur out due to classical effects. So, to maximize the entangled flux such that it remains

within the single photon per mode limit, it is crucial that higher total fluxes (due to increased grating lengths) are spread out across broader bandwidths (via stronger chirps). An unchirped or bulk crystal will blur out quantum effects quicker than the chirped crystal with increasing length. The length reported here is to balance these effects.

3.3 Experiment and results

SPDC Characterization

The periodically poled congruent lithium tantalate gratings were manufactured by HC Photonics. The unchirped chip consists of 8 gratings with different poling periods (8.5, 9, 9.5, 10, 10.5, 11, 11.5, 12 μm). It is 20 mm long and each channel has a 0.9 mm by 0.5 mm cross section. The chirped chip consists of 6 gratings with varying chirp parameters and entrance poling periods (Table 3.1). Each grating is 18 mm long and has a 1 mm by 0.3 mm cross section. The gratings are AR-coated on both input and output faces at 406 nm (R< 0.5%)/812 nm (R< 0.5%).

Grating	$\Lambda_1[\mu m]$	$\Lambda_c[\mu m]$	$\Lambda_2[\mu m]$	Chirp
1	9.000	9.45	9.900	10%
2	9.048	9.50	9.952	10%
3	9.095	9.55	10.005	10%
4	9.143	9.60	10.057	10%
5	9.190	9.65	10.110	10%
6	9.238	9.70	10.162	10%

Table 3.1: Chip parameters

The experimental setup, as illustrated in Fig. 3.8, consisted of a computer-tunable, CW Ti:Sapphire laser (M2 SolsTiS) and an external SHG cavity to act as the pump source. The maximal output power of the SHG at 406 nm was 1.15 W with a 0.89 nm linewidth. The pump beam is focused through the ppCLT grating using an aspheric lens with a 40 cm focal length. This focal length is chosen such that the size of the focused beam was smaller than the grating's cross sectional dimension and further optimized for peak SPDC brightness. The position of the crystal can be finely adjusted in the XYZ directions using a piezoelectric stage, which is critical for maximizing the entangled photon flux. The angular deviation of the grating's long axis relative to the input beam was not as crucial as the X-Y centering of the chip around the focused beam and the z-control over exact focal point positioning. The

temperature of the crystal is controlled by a ceramic heater and PID loop (Covesion) to an accuracy of 10 mK.

To measure the SPDC spectrum as well as the power of the downconverted flux, the output of the grating is passed through a total of three OD-4 500 nm longpass filters (Edmund Optics) to eliminate the residual 406 nm pump. The SPDC cone is collimated with an off-axis parabolic mirror and then focused into a USB spectrometer (Thorlabs). For more detailed characterization, the SPDC cone is collimated with a telephoto lens and then focused into a spectrometer (Princeton Instruments IsoPlane) with a 15cm focal length lens. In this configuration, spectral and power measurements are performed with an electron multiplying intensified CCD camera (emICCD, Princeton Instruments MAX4). For the broadband spectral measurements, spectra are collected and stitched together as a 800 nm blazed grating with 150 grooves/mm is scanned across several center wavelengths. These spectra are then background corrected, quantum efficiency corrected according to the detection efficiency of the emICCD camera, and normalized.

Fig. 3.7 (a) depicts the SPDC spectra for the 9.50 μm unchirped grating as the temperature of the crystal is varied from 60℃ to 160℃. Above 150℃, the shift from degenerate to non-degenerate emission conditions is apparent from the decrease in intensity around the degenerate wavelength region of 812 nm (gray dashed line). In comparison, as shown in Fig. 3.7 (b), at 145℃, the chirped chip (blue curve) exhibits much broader and flatter emission than the unchirped counterpart (red curve). The ratio of the flux produced by the chirped grating to that produced by the unchirped grating is $\sim$1.7. This increased flux is due to the lower wavelength components, as shown in Fig. 3.7b. The occupation per spatial mode was not estimated here because of the difficulty of collimating the full SPDC cone.

Two-Photon Interference

The fourth-order interference between entangled photon pairs was quantified with a two-photon Michelson interferometer, depicted in Fig. 3.8. The Michelson interferometer is chosen because the configuration allows a broader bandwidth of the SPDC cone to be easily utilized, in contrast to a Mach-Zehnder configuration. Following the end of the ppLT chip, the entangled photons are collimated with an off-axis parabolic mirror and a cylindrical lens. These photons are directed through a broadband nonpolarizing 50:50 beamsplitter (BS1, Layertec) which separates the incident photons into two paths. In the reflected path, the photons pass through an

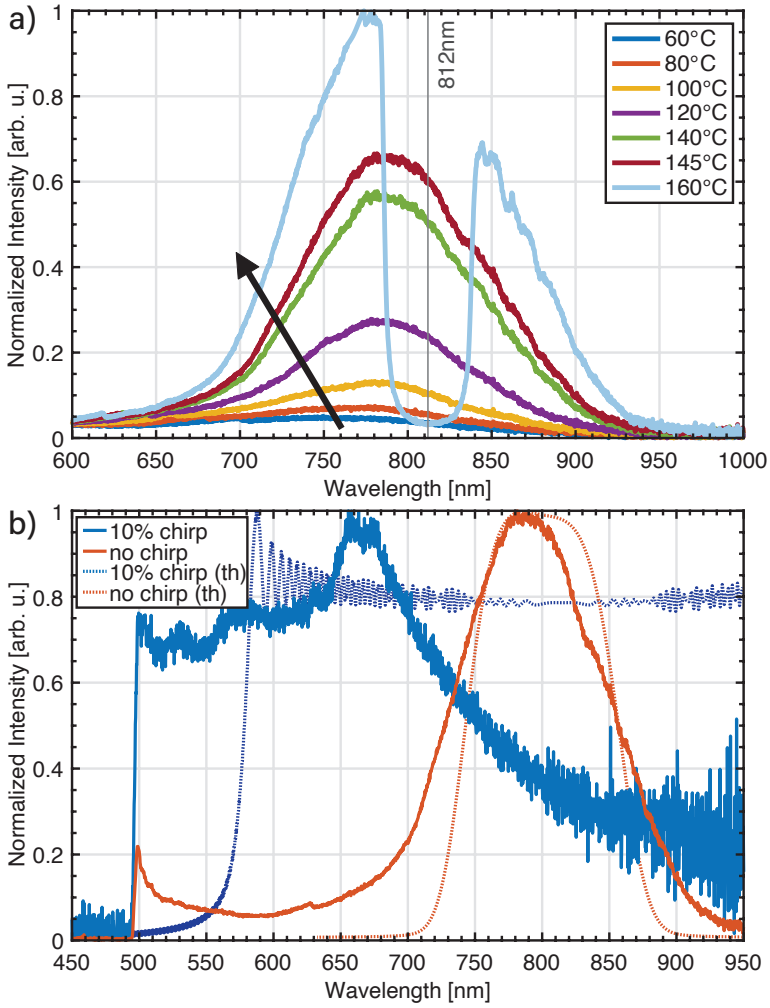

Figure 3.7: Simulated and measured SPDC spectra for chirped and unchirped gratings. (a) SPDC spectra for a 9.50 µm unchirped grating, gray reference line marks the degenerate wavelength of 812 nm. Arrow a guide in the direction of increasing temperature. (b) Experimental (solid) and theoretical (dashed) SPDC spectra for a chirped grating with a 9.50 µm center poling period and 10% chirp rate. Both spectra taken at a temperature of 145°C. The chirped emission is broader and has a flatter top than the unchirped emission. Note the detector cut-off at 900 nm.

achromatic quarter-wave plate (Thorlabs) twice to rotate their polarizations. The optical path length difference between the two arms is adjusted by scanning a mirror mounted to a linear stage in the transmitted arm. Coincidence counts vs. optical path length difference are then collected at one of the output arms of BS1. The coincidence counting setup consists of a second broadband 50:50 beamsplitter (BS2, Layertec), and two free-space-to-fiber coupling setups connecting to single-photon avalanche diodes (SPADs, Laser Component COUNT) and time-tagging

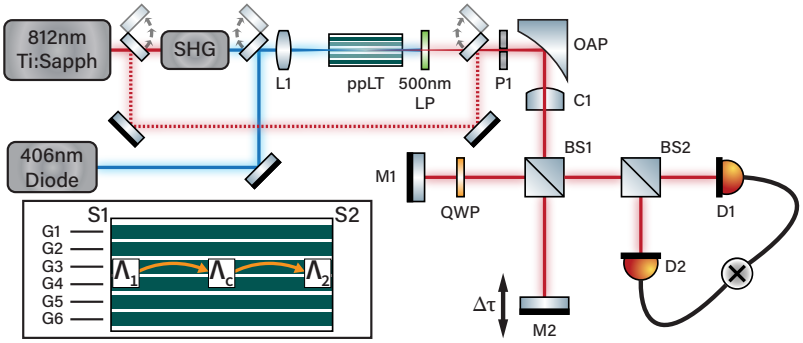

Figure 3.8: Entangled photon pair Michelson interferometer used to measure the fourth order interference. SHG: second harmonic generation unit, L1: focusing lens, ppLT: periodically poled lithium tantalate chip, LP: longpass filter, OAP: off-axis parabolic mirror, C1: cylindrical lens, BS1 and BS2: 50:50 beamsplitters, M1 and M2: mirrors, QWP: quarter-wave plate, D1 and D2: multimode fiber coupled single photon avalanche diodes connected to coincidence counting unit. The flip mirrors allow re-configuring such that the Ti:Sapph output is picked off and used for aid in alignment of downstream optics. A 406 nm diode laser is used as an alternate pump source. (Inset) Chip diagram showing the grating layout and their corresponding entrance (Λ_1), center (Λ_c), and end (Λ_2) poling periodicity locations in reference to Table.3.1.

electronics (PicoHarp 300). Because of the high SPDC flux, the pump beam must first be dimmed by three orders of magnitude to avoid SPAD saturation (counting rate 10^6 photons/s). Full counting rate experiments can be completed using the CCD alone [54, 55] but were not implemented at the time of writing this paper.

The free-space-to-fiber coupling setups each consist of 2 mirrors to align the beamsplitter outputs through a 4.51 mm focal length asphere, which then focuses the beam into a multimode fiber (105μm core diameter, 0.22 NA) connected to the SPADs. For these measurements, the coincidence time-bin resolution is set to 8 ps and coincidences are summed within a 10 ns window. Fourth-order interferograms were measured for different bandwidths of entangled photon pairs. For the first experiment, bandpass filters centered at 810 nm with a 10 nm FWHM are mounted to the front of each of the fiber coupling units. Note that this filter is not at the 812nm degenerate wavelength and reduces the degree of entanglement. For the second experiment, the 810 nm bandpass filters are removed to couple the broadband, collinear SPDC into the SPADs. Finally, the oven is allowed to cool to the non-collinear but degenerate temperature of 150℃, and broadband two-photon interference was measured again. Note that due to the large bandwidth of the SPDC,

the fiber coupling efficiency of the non-degenerate photons is also poor at less than 10% of total power. Thus, 42% of the overall SPDC flux was lost before reaching the fibers connecting to the SPADs. Over 20% of the loss was due to the high angular dispersion of the beam, while the other ~ 20% of the loss was due to the reflective optics such as the aluminum OAP and silver mirrors. As discussed at the end of this section, optics development is still needed similar to using classical broadband ultrafast lasers.

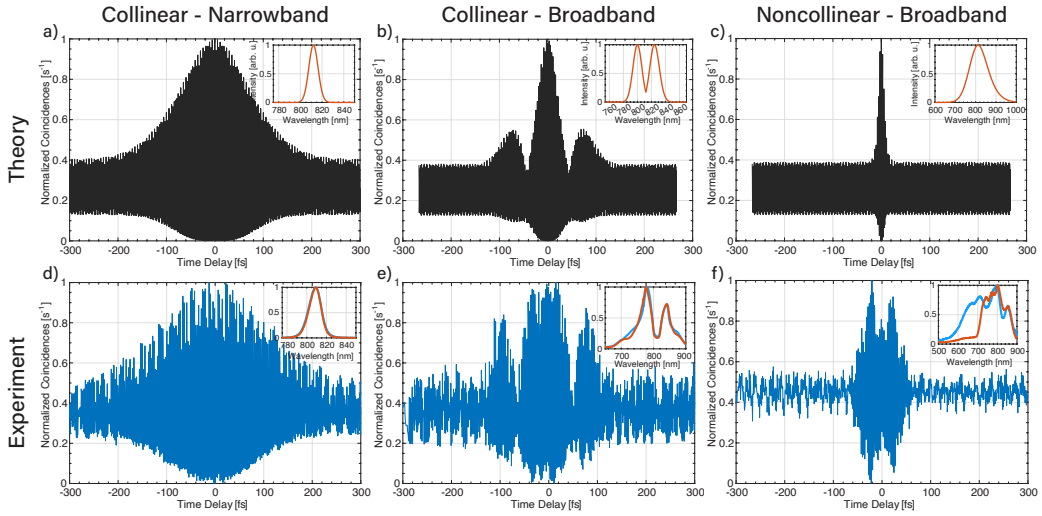

Figure 3.9: Simulated (top row) and measured (bottom row) fourth-order interference for narrowband collinear (a,d), broadband collinear (b,e), and broadband non-collinear (c,f) entangled photons. Coincidence counts are measured with 15 s integration time. The insets in each figure depict the SPDC spectra used to simulate or measure the corresponding interference in each detector arm. For simulations, Gaussian functions are used to approximate SPDC spectral envelopes. As shown in Table 3.2, the theoretical and measured coherence times are 200 fs and 245 fs for collinear narrowband, 45 fs and 57.4 fs for collinear broadband, 18 fs and 62 fs for non-collinear broadband. The growing difference between expected time resolution from the SPDC bandwidth and the measured interference is due to the difficulty with fiber coupling the full cone emission profile.

Fig. 3.9 shows the simulated fourth-order interferences using the produced bandwidth of the SPDC source and then the measured fourth-order interferences for two collinear bandwidths and a third non-collinear, full spectrum measurement. When the quarter-wave plate is set to 0°, the photons arriving at BS1 have the same polarization, and interfere coherently as correlated pairs. The interference pattern is robust against pump power fluctuations. When the quarter-wave plate is rotated to 45°, the reflected arm becomes perpendicularly polarized to the transmitted arm, the

interference pattern disappears, and the coincidence counts follow the average pump power reading collected before and after the coincidence detection (Figs. A.8,A.9). The resulting coherence length of the total flux can be determined from the width of the interference peak. Table 3.2 summarizes the theoretical and measured coherence lengths.

	Collinear narrowband	Collinear broadband	Non-collinear broadband
Theoretical coherence time [fs]	200	45	18
Measured coherence time [fs]	245	57.4	62

Table 3.2: Coherence times of different configurations and bandwidths of SPDC

For the measurement with 810-(10) nm bandpass filters mounted to the front of the fiber coupling units, shown in Fig. 3.9(d), the coherence length is approximately 73μm (or 245 fs). The simulated interference pattern as well as the coherence length of 60μm (200 fs), shown in Fig. 3.9(a), agree fairly with the measurement given that the 10nm bandpass filter is offset from the degenerate wavelength of 812 nm. Note that the measured bandwidth after the fiber is roughly double what it actually is because the spectrometer slit had to be run wide to get sufficient flux for spectral analysis after the fiber coupling. The theoretical plot uses the correct bandwidth. Fig. 3.9(e) shows the interference from collinear broadband SPDC flux without bandpass filters. The bandwidth is reduced and the SPDC spectrum is split (nondegenerate) because the phase matching temperature is maintained at the elevated collinear emission (Fig. 3.2). From the width of the center peak, the coherence length is approximately 17.2μm (or 57.4 fs). For reference, the simulated coherence length is approximately 13μm (45 fs). Similarly, Fig. 3.9(f) shows the lower temperature non-collinear broadband interference. Here, the full 200 nm bandwidth of the SPDC source is attempted to be used (expected temporal width 8 fs). However the spectrum reaching the detector is limited to 125 nm because of collimation issues, upstream optics, and fiber coupling. The coherence length calculated from the measured width of the peak is 18.9μm (or 62 fs). This indicates that the degree of entanglement has degraded due to poor fiber coupling at non-collinear temperatures and other upstream optics. For example, the spectrum after the multiple beamsplitters is not balanced (Fig. 3.9(f), inset) as compared to

the other cases. The increased temporal width is also indicative of the need for dispersion management upstream, just as is similar to a broadband ultrafast laser pulse of an expected 20 fs pulse. The same would be true for the chirped (> 200 nm) SPDC source so an interferogram is not shown here. Note that the measured broadband spectra in the insets do not well match the theoretical spectra. This is because 1) fiber coupling of the broad bandwidth was not optimal and 2) the free space spectrometer slit was opened wide to increase the measurement fluxes which leads to a spectral broadening by a factor of 2.

The lack of fiber coupling efficiency in the broadband, non-collinear case is not simply one of input optics. Immediately following the chip, the spatial profile of the entangled photons is cone-like with a wavelength-dependent distribution (Fig. 3.10 left). The measured angular deviation with wavelength matches the simulated entangled photon emission. Within a non-degenerate pair, the idler photon has a larger emission angle than the signal photon. The wavelength-dependent angular emission cone present a challenge in the implementation of free-space broadband entangled photon setups because the emission does not act like single point source. We attempted to collimate the emission cone using a variety of free-space optical configurations and found that a telephoto lens or an off-axis parabolic mirror (sometimes with an additional cylindrical lens for beam shaping) provides the best long range spatial profiles. After a propagation length of 45 cm into the far field, the entangled photon cone collapses (Fig. 3.10 middle). This spatial profile collapse is most likely due to the interference of photon pairs created along the length of the crystal and scattering effects near the domain boundaries of the grating. The end result shows characteristics of somewhere between a Laguerre and a Hermite mode which would match the circular emission in a square profile created by the source. The beam profile will likely be improved by using adaptive optics. The far field effects could also be reduced by using a waveguide instead of a grating; however, nanophotonic implementations cannot handle the high input powers used in this paper and fiber coupling of the broadband emission spectrum from waveguides is not yet well developed. Another obvious option is, instead of using fiber coupled SPADs for the detection, is to move to emICCD photon counting techniques that would not require focusing of the collapsed beam profile. However, this approach still needs exploration and requires an emICCD even more costly than SPADs. A necessary future development for the broadband entangled photon source is the clean-up of the SPDC spatial mode. Following the output of the bulk crystal, several possible improvements can be implemented including a spatial light modulator

(SLM) to imprint phase and intensity shifts on the SPDC cone [56]. Alternatively, a combination of diffraction gratings and lenses could be used to correct the angular dispersion of the broadband wavelengths. The SPDC output could also be coupled into a broad bandwidth photonic crystal fiber such that the photons are propagating in a single spatial mode. Further, the spatial mode of the input pump beam could be modulated with an SLM or combinations of lenses/axicons to achieve the desired output SPDC spatial mode. Further investigation into the creation and collimation of broadband entangled photons is critical for the implementation of short temporal length, high flux entangled photon spectroscopy.

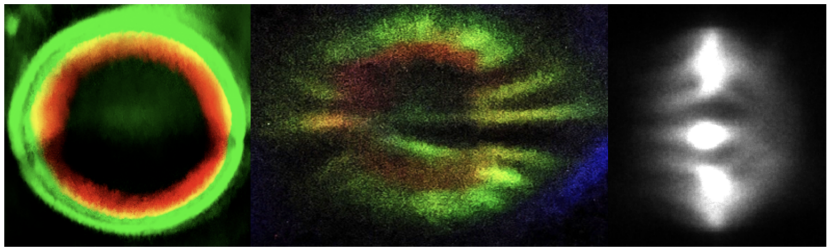

Figure 3.10: Images of collimated SPDC emission cone at 145℃ in the near field (left), far field (middle) after collimation with an off axis parabolic mirror, and far field after collimation and focusing by a 15.45 cm focal length lens (right). The left and middle images are collected with a standard cell-phone camera, the right image is collected with an emICCD.

3.4 Conclusion

Quasi-phase-matching in periodically poled crystals offers significant benefits in the experimental implementation of broadband entangled photon sources for use in spectroscopy. Simulated parameters for unchirped, periodically poled lithium tantalate gratings were utilized to design and construct a broadband entangled photon source spanning nearly an octave in frequency. This broadband source was characterized by measuring the output spectra of the grating and the fourth order interference by a two-photon Michelson interferometer. The two-photon Michelson interferometer was used to emphasize where further optics and detector development is still need to utilize the broadband and short temporal width sources. As in, the SPDC spectrum can be reliably created from the designed chip, however, the downstream optics and detectors still need development to fully utilize this source. Given the theoretical and experimentally demonstrated advantages of entangled photons in studies of chemical, biological, and material systems, we anticipate the widespread applicability of this particular energy-time entangled photon source.

References

1. Burnham, D. C. & Weinberg, D. L. Observation of Simultaneity in Parametric Production of Optical Photon Pairs. *Physical Review Letters* **25,** 84–87. https://link.aps.org/doi/10.1103/PhysRevLett.25.84 (1970).

2. Szoke, S., Liu, H., Hickam, B. P., He, M. & Cushing, S. K. Entangled Light–Matter Interactions and Spectroscopy. *Journal of Materials Chemistry C* **8,** 10732–10741. http://pubs.rsc.org/en/content/articlelanding/2020/tc/d0tc02300k (2020).

3. Hong, C. K., Ou, Z. Y. & Mandel, L. Measurement of subpicosecond time intervals between two photons by interference. *Physical Review Letters* **59,** 2044–2046. https://link.aps.org/doi/10.1103/PhysRevLett.59.2044 (1987).

4. Mitev, V., Balet, L., Torcheboeuf, N., Renevey, P. & Boiko, D. L. Discrimination of entangled photon pair from classical photons by de Broglie wavelength. *Scientific Reports* **10,** 7087. https://www.nature.com/articles/s41598-020-63833-8 (2020).

5. Shimizu, R., Edamatsu, K. & Itoh, T. Quantum diffraction and interference of spatially correlated photon pairs generated by spontaneous parametric down-conversion. *Physical Review A* **67,** 041805. https://link.aps.org/doi/10.1103/PhysRevA.67.041805 (2003).

6. Abouraddy, A. F., Saleh, B. E. A., Sergienko, A. V. & Teich, M. C. Double-slit interference of biphotons generated in spontaneous parametric downconversion from a thick crystal. *Journal of Optics B: Quantum and Semiclassical Optics* **3,** S50. https://dx.doi.org/10.1088/1464-4266/3/1/359 (2001).

7. Javanainen, J. & Gould, P. L. Linear intensity dependence of a two-photon transition rate. *Physical Review A* **41,** 5088–5091. https://link.aps.org/doi/10.1103/PhysRevA.41.5088 (1990).

8. Dayan, B., Pe'er, A., Friesem, A. A. & Silberberg, Y. Nonlinear Interactions with an Ultrahigh Flux of Broadband Entangled Photons. *Physical Review Letters* **94,** 043602. https://link.aps.org/doi/10.1103/PhysRevLett.94.043602 (2005).

9. Villabona-Monsalve, J. P., Burdick, R. K. & Goodson, T. I. Measurements of Entangled Two-Photon Absorption in Organic Molecules with CW-Pumped Type-I Spontaneous Parametric Down-Conversion. *The Journal of Physical Chemistry C* **124,** 24526–24532. https://doi.org/10.1021/acs.jpcc.0c08678 (2020).

10. Raymer, M. G., Marcus, A. H., Widom, J. R. & Vitullo, D. L. P. Entangled Photon-Pair Two-Dimensional Fluorescence Spectroscopy (EPP-2DFS). *The*

Journal of Physical Chemistry B **117,** 15559–15575. https://doi.org/10.1021/jp405829n (2013).

11. Tabakaev, D. *et al.* Energy-time-entangled two-photon molecular absorption. *Physical Review A* **103,** 033701. https://link.aps.org/doi/10.1103/PhysRevA.103.033701 (2021).

12. Li, T., Li, F., Altuzarra, C., Classen, A. & Agarwal, G. S. Squeezed light induced two-photon absorption fluorescence of fluorescein biomarkers. *Applied Physics Letters* **116,** 254001. https://aip.scitation.org/doi/10.1063/5.0010909 (2020).

13. Kang, G. *et al.* Efficient Modeling of Organic Chromophores for Entangled Two-Photon Absorption. *Journal of the American Chemical Society* **142,** 10446–10458. https://doi.org/10.1021/jacs.0c02808 (2020).

14. Boto, A. N. *et al.* Quantum Interferometric Optical Lithography: Exploiting Entanglement to Beat the Diffraction Limit. *Physical Review Letters* **85,** 2733–2736. https://link.aps.org/doi/10.1103/PhysRevLett.85.2733 (2000).

15. Steuernagel, O. On the concentration behaviour of entangled photons. *Journal of Optics B: Quantum and Semiclassical Optics* **6,** S606–S609. https://iopscience.iop.org/article/10.1088/1464-4266/6/6/021 (2004).

16. Oka, H. Selective two-photon excitation of a vibronic state by correlated photons. *The Journal of Chemical Physics* **134,** 124313. http://aip.scitation.org/doi/10.1063/1.3573565 (2011).

17. Oka, H. Enhanced vibrational-mode-selective two-step excitation using ultrabroadband frequency-entangled photons. *Physical Review A* **97,** 063859. https://link.aps.org/doi/10.1103/PhysRevA.97.063859 (2018).

18. Schlawin, F., Dorfman, K. E. & Mukamel, S. Entangled Two-Photon Absorption Spectroscopy. *Accounts of Chemical Research* **51,** 2207–2214. https://doi.org/10.1021/acs.accounts.8b00173 (2018).

19. Dorfman, K. E., Schlawin, F. & Mukamel, S. Nonlinear optical signals and spectroscopy with quantum light. *Reviews of Modern Physics* **88,** 045008. https://link.aps.org/doi/10.1103/RevModPhys.88.045008 (2016).

20. MacLean, J.-P. W., Schwarz, S. & Resch, K. J. Reconstructing ultrafast energy-time-entangled two-photon pulses. *Physical Review A* **100,** 033834. https://link.aps.org/doi/10.1103/PhysRevA.100.033834 (2019).

21. Nasr, M. B., Giuseppe, G. D., Saleh, B. E. A., Sergienko, A. V. & Teich, M. C. Generation of high-flux ultra-broadband light by bandwidth amplification in spontaneous parametric down conversion. *Optics Communications* **246,**

521–528. https://www.sciencedirect.com/science/article/pii/S0030401804011162 (2005).

22. Kwiat, P. G. *et al.* New High-Intensity Source of Polarization-Entangled Photon Pairs. *Physical Review Letters* **75,** 4337–4341. https://link.aps.org/doi/10.1103/PhysRevLett.75.4337 (1995).

23. Friberg, S., Hong, C. K. & Mandel, L. Measurement of Time Delays in the Parametric Production of Photon Pairs. *Physical Review Letters* **54,** 2011–2013. https://link.aps.org/doi/10.1103/PhysRevLett.54.2011 (1985).

24. Kwiat, P. G., Waks, E., White, A. G., Appelbaum, I. & Eberhard, P. H. Ultrabright source of polarization-entangled photons. *Physical Review A* **60,** R773–R776. https://link.aps.org/doi/10.1103/PhysRevA.60.R773 (1999).

25. Karan, S. *et al.* Phase matching in β-barium borate crystals for spontaneous parametric down-conversion. *Journal of Optics* **22,** 083501. https://dx.doi.org/10.1088/2040-8986/ab89e4 (2020).

26. Nikogosyan, D. N. Beta barium borate (BBO). *Applied Physics A* **52,** 359–368. https://doi.org/10.1007/BF00323647 (1991).

27. Midwinter, J. E. & Warner, J. The effects of phase matching method and of crystal symmetry on the polar dependence of third-order non-linear optical polarization. *British Journal of Applied Physics* **16,** 1667. https://dx.doi.org/10.1088/0508-3443/16/11/307 (1965).

28. Roslyak, O. & Mukamel, S. Multidimensional pump-probe spectroscopy with entangled twin-photon states. *Physical Review A* **79,** 063409. https://link.aps.org/doi/10.1103/PhysRevA.79.063409 (2009).

29. Lerch, S. & Stefanov, A. Experimental requirements for entangled two-photon spectroscopy. *The Journal of Chemical Physics* **155,** 064201. https://aip.scitation.org/doi/10.1063/5.0050657 (2021).

30. Wang, S., Pasiskevicius, V., Hellström, J., Laurell, F. & Karlsson, H. First-order type II quasi-phase-matched UV generation in periodically poled KTP. *Optics Letters* **24,** 978–980. https://www.osapublishing.org/ol/abstract.cfm?uri=ol-24-14-978 (1999).

31. Yu, N. E., Ro, J. H., Cha, M., Kurimura, S. & Taira, T. Broadband quasi-phase-matched second-harmonic generation in MgO-doped periodically poled $LiNbO_3$ at the communications band. *Optics Letters* **27,** 1046–1048. https://opg.optica.org/ol/abstract.cfm?uri=ol-27-12-1046 (2002).

32. Lin, J. *et al.* Broadband Quasi-Phase-Matched Harmonic Generation in an On-Chip Monocrystalline Lithium Niobate Microdisk Resonator. *Physical Review Letters* **122,** 173903. https://link.aps.org/doi/10.1103/PhysRevLett.122.173903 (2019).

33. Chen, J., Pearlman, A. J., Ling, A., Fan, J. & Migdall, A. L. A versatile waveguide source of photon pairs for chip-scale quantum information processing. *Optics Express* **17,** 6727. https://www.osapublishing.org/oe/abstract.cfm?uri=oe-17-8-6727 (2009).

34. Bock, M., Lenhard, A., Chunnilall, C. & Becher, C. Highly efficient heralded single-photon source for telecom wavelengths based on a PPLN waveguide. *Optics Express* **24,** 23992. https://opg.optica.org/abstract.cfm?URI=oe-24-21-23992 (2016).

35. Shi, B.-S. & Tomita, A. Highly efficient generation of pulsed photon pairs with bulk periodically poled potassium titanyl phosphate. *Journal of the Optical Society of America B* **21,** 2081–2084. https://opg.optica.org/josab/abstract.cfm?uri=josab-21-12-2081 (2004).

36. Armstrong, J. A., Bloembergen, N., Ducuing, J. & Pershan, P. S. Interactions between Light Waves in a Nonlinear Dielectric. *Physical Review* **127,** 1918–1939. https://link.aps.org/doi/10.1103/PhysRev.127.1918 (1962).

37. Tanzilli, S. *et al.* Highly efficient photon-pair source using periodically poled lithium niobate waveguide. *Electronics Letters* **37,** 26. https://digital-library.theiet.org/content/journals/10.1049/el_20010009 (2001).

38. Nasr, M. B. *et al.* Ultrabroadband Biphotons Generated via Chirped Quasi-Phase-Matched Optical Parametric Down-Conversion. *Physical Review Letters* **100,** 183601. https://link.aps.org/doi/10.1103/PhysRevLett.100.183601 (2008).

39. Pe'er, A., Dayan, B., Friesem, A. A. & Silberberg, Y. Temporal Shaping of Entangled Photons. *Physical Review Letters* **94,** 073601. https://link.aps.org/doi/10.1103/PhysRevLett.94.073601 (2005).

40. Ou, Z. Y. & Lu, Y. J. Cavity Enhanced Spontaneous Parametric Down-Conversion for the Prolongation of Correlation Time between Conjugate Photons. *Physical Review Letters* **83,** 2556–2559. https://link.aps.org/doi/10.1103/PhysRevLett.83.2556 (1999).

41. Hadfield, R. H. Single-photon detectors for optical quantum information applications. *Nature Photonics* **3,** 696–705. https://www.nature.com/articles/nphoton.2009.230 (2009).

42. Lerch, S. & Stefanov, A. Observing the transition from quantum to classical energy correlations with photon pairs. *Communications Physics* **1,** 1–6. https://www.nature.com/articles/s42005-018-0027-2 (2018).

43. Zverev, G. M., Levchuk, E. A., Pashkov, V. A. & Poryadin, Y. D. Laser-Radiation-Induced Damage to the Surface of Lithium Niobate and Tantalate Single Crystals. *Soviet Journal of Quantum Electronics* **2,** 167. https://io

pscience.iop.org/article/10.1070/QE1972v002n02ABEH004409/meta (1972).

44. Antonov, V. A., Arsenev, P. A., Linda, I. G. & Farstendiker, V. L. Colour centres in single crystals of lithium tantalate. *physica status solidi (a)* **28,** 673–676. https://onlinelibrary.wiley.com/doi/abs/10.1002/pssa.2210280234 (1975).

45. Meyn, J.-P. & Fejer, M. M. Tunable ultraviolet radiation by second-harmonic generation in periodically poled lithium tantalate. *Optics Letters* **22,** 1214–1216. https://opg.optica.org/ol/abstract.cfm?uri=ol-22-16-1214 (1997).

46. Lopez-Mago, D. & Novotny, L. Coherence measurements with the two-photon Michelson interferometer. *Physical Review A* **86,** 023820. https://link.aps.org/doi/10.1103/PhysRevA.86.023820 (2012).

47. Klyshko, D. N., Penin, A. N. & Polkovnikov, B. F. Parametric Luminescence and Light Scattering by Polaritons. *Journal of Experimental and Theoretical Physics Letters* **11,** 11–14 (1970).

48. Boyd, R. W. *Nonlinear Optics* ISBN: 978-0-08-048596-6 (Elsevier, 2008).

49. Fejer, M. M., Magel, G. A., Jundt, D. H. & Byer, R. L. Quasi-phase-matched second harmonic generation: tuning and tolerances. *IEEE Journal of Quantum Electronics* **28,** 2631–2654 (1992).

50. Moutzouris, K., Hloupis, G., Stavrakas, I., Triantis, D. & Chou, M.-H. Temperature-dependent visible to near-infrared optical properties of 8 mol% Mg-doped lithium tantalate. *Optical Materials Express* **1,** 458–465. https://www.osapublishing.org/ome/abstract.cfm?uri=ome-1-3-458 (2011).

51. Di Giuseppe, G. *et al.* Entangled-photon generation from parametric down-conversion in media with inhomogeneous nonlinearity. *Physical Review A* **66,** 013801. https://link.aps.org/doi/10.1103/PhysRevA.66.013801 (2002).

52. Burlakov, A. V. *et al.* Interference effects in spontaneous two-photon parametric scattering from two macroscopic regions. *Physical Review A* **56,** 3214–3225. https://link.aps.org/doi/10.1103/PhysRevA.56.3214 (1997).

53. Brańczyk, A. M., Fedrizzi, A., Stace, T. M., Ralph, T. C. & White, A. G. Engineered optical nonlinearity for quantum light sources. *Optics Express* **19,** 55–65 (2011).

54. Reichert, M., Defienne, H. & Fleischer, J. W. Massively Parallel Coincidence Counting of High-Dimensional Entangled States. *Scientific Reports* **8,** 7925. http://www.nature.com/articles/s41598-018-26144-7 (2018).

55. Zhang, Y. *et al.* Multidimensional quantum-enhanced target detection via spectrotemporal-correlation measurements. *Physical Review A* **101,** 053808. https://link.aps.org/doi/10.1103/PhysRevA.101.053808 (2020).

56. Bessire, B., Bernhard, C., Feurer, T. & Stefanov, A. Versatile shaper-assisted discretization of energy–time entangled photons. *New Journal of Physics* **16,** 033017. https://dx.doi.org/10.1088/1367-2630/16/3/033017 (2014).

Chapter 4

SINGLE PHOTON SCATTERING CAN ACCOUNT FOR THE DISCREPANCIES BETWEEN ENTANGLED TWO-PHOTON MEASUREMENT TECHNIQUES

ABSTRACT

Entangled photon pairs are predicted to linearize and increase the efficiency of two-photon absorption, allowing continuous wave laser diodes to drive ultrafast time-resolved spectroscopy and nonlinear processes. Despite a range of theoretical studies and experimental measurements, inconsistencies persist about the value of the entanglement enhanced interaction cross section. A spectrometer is constructed that can temporally and spectrally characterize the entangled photon state before, during, and after any potential two-photon excitation event. Specifically, this instrument is based upon an interferometric design that probabilistically separates the entangled photon pairs and monitors the resulting transmitted signal, as well as the spectrally-resolved 90-degree signal from the sample. For the molecule Rhodamine 6G, which has a virtual state pathway, any entangled two-photon interaction is found to be equal to or lower than classical, single photon scattering events. This result can account for the discrepancies between the wide variety of entangled two-photon absorption cross sections reported from different measurement techniques. The reported instrumentation represents a major development in the field due to its ability to unambiguously separate classical and entangled effects and therefore is of importance for the growing field of nonlinear and multiphoton entangled spectroscopy.

Most of this chapter has been adapted with permission from:

Hickam, B. P. *et al.* Single-Photon Scattering Can Account for the Discrepancies among Entangled Two-Photon Measurement Techniques. *The Journal of Physical Chemistry Letters,* 4934–4940. `https://pubs.acs.org/doi/10.1021/acs.jpclett.2c00865` (2022).

4.1 Introduction

It is well known that the inherent correlations between entangled photons lead to spectroscopic enhancements in signal-to-noise [1–4], and diffraction limits [5] as well as measurement techniques such as ghost imaging [6–12]. A new and quickly growing field of entangled two-photon spectroscopy exploits these correlations in a different manner: enhancing excited state and multiphoton interactions [13–16]. For example, early experiments purported that entangled photons can linearize two-photon processes to achieve near one-photon absorption cross sections [17]. This finding would have far-reaching implications in optics and photonics as low power, continuous wave (CW) laser systems could replace pulsed lasers in spectroscopic techniques such as nonlinear bioimaging and ultrafast spectroscopy [18–20]. Combined with nanophotonic platforms that are capable of generating and manipulating entangled photon pairs [21, 22], ultrafast measurements could achieve unprecedented accessibility and availability.

While the entangled photons' linearization of two-photon processes can be derived theoretically [23–25], intense debate exists over the enhancement factor compared to classical two-photon absorption. Naively, one would expect the entangled two-photon absorption (ETPA) cross section to be close to that of a single photon process, given the linearization of the absorption. However, as shown in Fig. 4.1, the reported range of ETPA cross sections varies from near single photon levels to non-existent or barely higher than classical two-photon absorption at the same photon flux [17, 19, 26–38]. Complicating this debate is the disparate measurement techniques based on transmission, coincidence counting, and fluorescence that have been used. An agreed upon measurement process does not exist, and even those that are proposed rely on intensity counting methods instead of temporally and spectrally characterizing the entangled photon state during a proposed interaction event.

In this paper, we construct a spectrometer that temporally and spectrally measures the entangled photon state before, during, and after a proposed entangled two-photon event. The spectrometer is used to measure the proposed ETPA of a prototypical molecular dye, Rhodamine 6G (R6G), which has a well characterized, virtual state-mediated classical two-photon absorption pathway [40, 41]. To enhance the chances of measuring a two-photon fluorescence signal, the spectrometer uses a custom, high-flux (20 nW) entangled photon source with a tunable bandwidth and correlation time down to 20 fs [42]. By measuring the temporal and spectral characteristics of the entangled state in transmission, and the 90-degree signal relative to the cuvette,

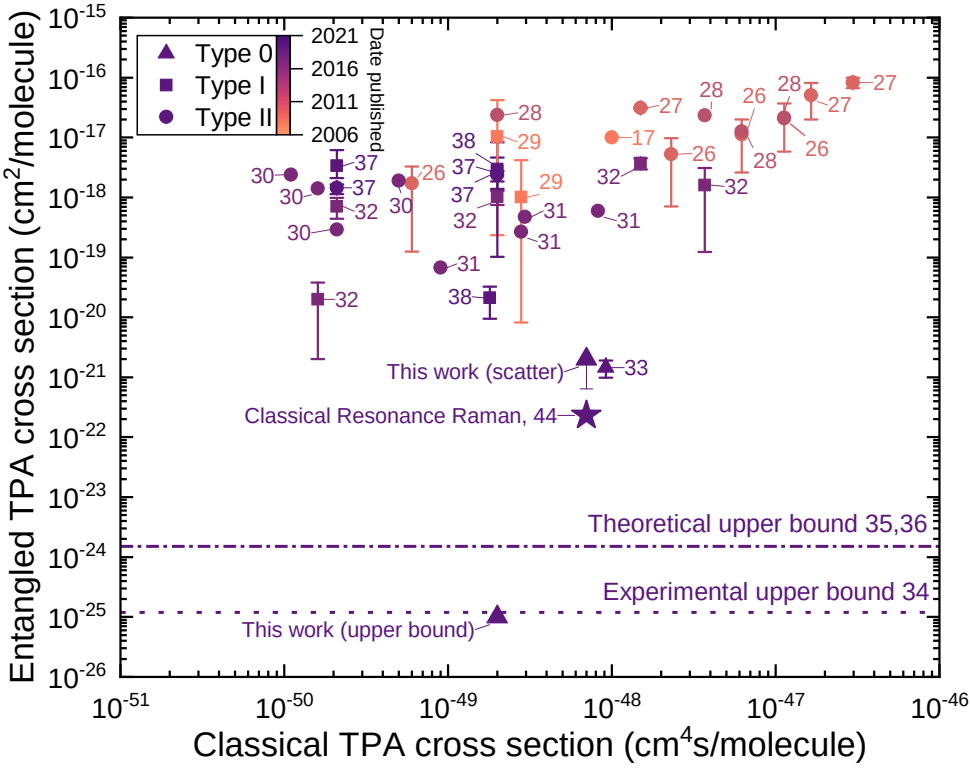

Figure 4.1: Reported experimental ETPA cross sections vs. classical TPA cross sections compiled from all ETPA studies conducted prior to January 2022 [17, 19, 26–38]. The shape of the data point reflects the polarization type of the entangled photons. Reported ETPA cross sections for the same compound at varying concentrations are represented as an average with vertical error bars indicating the highest and lowest reported bounds. The dashed lines represent ETPA upper bounds that were previously reported [34–36]. The shading of the points indicates the year in which the results were published, with darker colors representing more recent data. Classical resonance Raman cross section is also included [39].

we determine that if any entangled enhancement to the virtual-state mediated two-photon absorption is present, it has a cross section smaller than that of single photon (resonant) scattering ($\sim 10^{-21}$ cm^2/molecule).

The conclusion is based on the facts that: 1) the entangled state is nearly identical before and after transmission, with only a slight amplitude loss, and 2) the scattered signal temporally follows the pattern of one-photon interference instead of entangled two-photon interference, with spectral components far from the fluorescence spectrum of the dye. The single photon scattering explains the past discrepancies in

measured cross sections between different techniques. Moreover, the paper presents a blueprint for a spectrometer that can unambiguously determine entangled photon excited state effects in the rapidly growing field of entangled nonlinear and multiphoton spectroscopy. The scattering limited cross section for R6G also bolsters current theories that suggest virtual state pathways have cross sections that are beyond noise limits of single photon detectors and that real intermediate states may be necessary for entangled two-photon excitation events with high cross sections [43, 44].

4.2 Experimental overview

Entangled photons are generated from a periodically poled 8% MgO doped congruent lithium tantalate (CLT) bulk crystal. The design and spectral characterization of the entangled photon source have previously been reported [42]. The crystal is optimized for type-0 energy-time entanglement by spontaneous parametric down-conversion (SPDC). A bandwidth of $\sim$ 200 nm is produced by down-conversion of a 406 nm CW diode laser with a 1.5 nm linewidth. The large bandwidth and 10^{-8} conversion efficiency allow for a flux in the sub-μW range without exceeding the single-pair-per-mode quantum limit, as calculated by total photon pairs per second divided by the frequency bandwidth in Hz. The available photon flux is a significant improvement compared with the pW powers in most previous reports that use traditional bulk crystals such as beta barium borate (β-BBO) [17, 26, 31]. The broad bandwidth also results in a $\sim$ 20 fs correlation time (entanglement time) as measured after the sample. The entanglement time is not transform limited due to the group delay dispersion in the periodically poled chip and further optics. The high flux and tunable correlation times, from tens of femtoseconds to picoseconds, maximize the likelihood of measuring any entangled event [35, 36]. The entangled photon bandwidth can be varied by tuning the temperature of the bulk crystal. For experiments in this paper, two distinct entangled photon bandwidths centered at 812 nm were utilized: a non-degenerate "split" SPDC spectrum spanning $\sim$ 200 nm in wavelength and a degenerate "unsplit" SPDC spectrum (more details in B). The two SPDC spectra are used to emphasize the scattering that can happen both close to and far from resonance of a molecule's absorption.

Rhodamine 6G was selected for this study because of its absorption near the SPDC pump laser wavelength [40], its purely virtual two-photon classical absorption, as well as its high fluorescence quantum yield [45]. There are also several references of the proposed R6G ETPA from different measurement techniques [33, 34]. A concentration of 5 mM R6G in ethanol is used for experiments; the classical single-

photon fluorescence spectrum for this concentration is depicted in Fig. 4.4. Solvent effects and molecular dimerization at high sample concentration accounts for the redshifted spectrum [46]. Previously reported one-photon absorption cross sections for R6G in ethanol are on the order of 10^{-16} – 10^{-17} cm^2/molecule and the two-photon absorption cross section is $70(\pm 10.5) * 10^{-50}$ cm^{4}s/molecule [40]. A higher 110 mM sample was also tested with the same conclusions. The 110 mM sample would have a 10-times higher fluorescence after the drop in quantum yield and self-absorption effects are taken into account, but the results of the paper were unchanged.

A custom two-photon Michelson-type interferometer, shown in Fig. 4.2, is used to characterize the entangled photon state. Specifically, the fourth-order interference, spectral characteristics, and entanglement (coherence) time of the broadband entangled photons are determined [47, 48]. Type-0 SPDC was chosen because it utilizes the highest second-order nonlinear coefficient of $LiTaO_3$ [49]. The two-photon Michelson-type interferometer allows the broad, collinear SPDC bandwidth to be more easily directed onto the sample. More specifically, the photon pairs are focused (beam waist 500 μm) onto the center of the cuvette. The measurement protocol is as follows: first, a cuvette containing pure ethanol is placed at the output of the Michelson interferometer. Second, the fourth-order interference is measured by collecting coincidences as a function of an optical time delay. The coincidence counting detection setup consists of a broadband 50:50 beamsplitter and two single photon avalanche photodiodes (SPADs, Laser Components). The fourth-order interference measurements are then repeated with the cuvette filled with R6G solution. Simultaneous to the coincidence counting measurement, a single photon counting EMICCD spectrometer (Princeton Instruments) is placed at 90 degrees relative to the excitation beam to measure any scatter or fluorescence. The collection efficiency including the spectrometer is $\sim 10^{-4}$, calculated from the measured classical single photon fluorescence and quantum yield of R6G. By monitoring the timescale and spectral features of the 90-degree signal, one can differentiate one-photon events, such as scattering, from an entangled two-photon absorption or fluorescence event [33, 34, 50]. A complete mathematical description of the interferometer output can be found in the supplementary information.

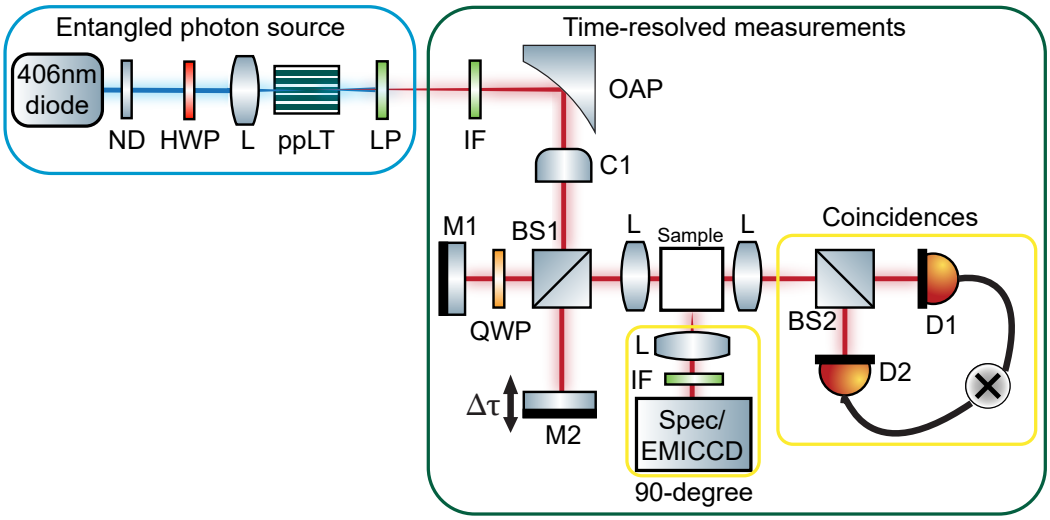

Figure 4.2: Experimental setup used to measure the proposed entangled two-photon absorption and 90-degree signal. The entangled photon source consists of a continuous wave diode laser pumping a periodically poled lithium tantalate crystal. The resultant entangled photon cone is collimated before the two-photon Michelson interferometer. The fourth-order interference of the entangled photon pairs is measured with a coincidence counting configuration and the time-resolved 90-degree signal was imaged onto a spectrometer/EMICCD. ND: continuous neutral density filter wheel, HWP: half-wave plate, L: lens, ppLT: periodically poled lithium tantalate chip, LP: 500 nm longpass filter, IF: interference filter, OAP: off-axis parabolic mirror, C1: cylindrical lens, QWP: quarter-wave plate, BS1 and BS2: 50:50 plate beamsplitters, M1 and M2: mirrors, D1 and D2: multimode fiber coupled single photon avalanche diodes connected to a coincidence circuit, Spec/EMICCD: Spectrometer and electron multiplying intensified charge coupled device.

4.3 Results: Fourth-order interference measurements

Fig. 4.3 shows the fourth-order interference of the entangled photon state before and after interacting with 5 mM R6G/ethanol as well as the signal collected at 90-degrees to the excitation pathway during the interaction. Corresponding theoretical fitting is included in the supplementary information. The top trace is the measured coincidences through a cuvette filled with pure ethanol. In a two-photon Michelson interferogram, the degree of entanglement can be qualitatively inferred by examining the amplitude ratio above and below the oscillation baseline. A "top-heavy" feature, for example shown in Fig. 4.3 top trace, indicates photon bunching. Given the $> 95\%$ visibility measured here and the fact that SPDC with a CW laser inherently creates an entangled state, we can reasonably confirm that our input source is entangled. For this experiment, the coherence/entanglement time is < 20 fs and the

interference visibility is 0.94. When the cuvette is filled with R6G (middle trace in Fig. 4.3), the visibility of the interference slightly decreases to 0.86, but the interferogram retains the spectral and temporal features shown with ethanol (with a slight shift in temporal patterns due to the change in refractive index. If ETPA does occur, then the photon bunching feature will diminish and the classical component will change spectrally due to the added fluorescence signal (or a nonuniform single photon absorption process).

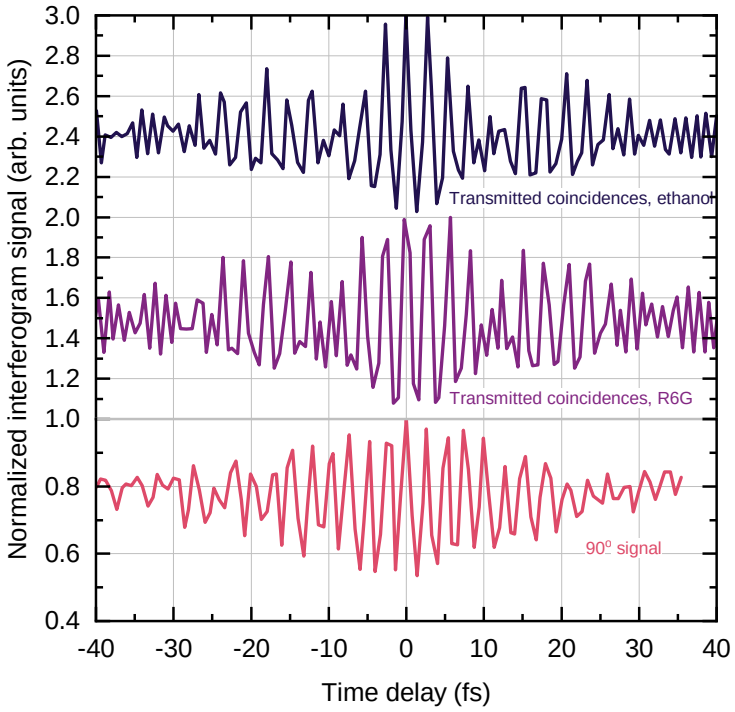

Figure 4.3: Photon counts versus time delay for broadband entangled photons traveling through a two-photon Michelson interferometer. The top trace is transmitted coincidence counts through ethanol, the middle trace is transmitted coincidence counts through R6G in ethanol, and the bottom trace is summed EMICCD counts of the 90-degree signal. Comparison of these three signals indicates that only single photon events, and not an entangled two-photon event, is present for the R6G. The y axis has been scaled and shifted for visualization.

To simulate fourth-order interferograms, the Fourier-transformed spectra of experimental interferograms are fitted to Gaussian peaks (Fig. B.1). The fitted spectrum is then used as the input spectrum for an entangled two-photon Michelson simulation (Fig. B.2). The bottom trace in Fig. 4.3 shows the summed spectrum collected at 90-degrees by the EMICCD. The interferogram follows that of a one-photon in-

terference from a single Gaussian peak, also depicted in Fig. B.1. If the collected signal originated from an entangled two-photon event, it would follow the pattern of the input state and exhibit a matching two-photon interference as the molecule would act similar to a coincidence counter [50].

4.4 Results: Wavelength-resolved measurements of Rhodamine 6G

The one-photon nature of the scattered signal is further confirmed by looking at the wavelength spectrum collected at 90-degrees (Fig. 4.4). The measured single photon fluorescence of R6G is shown for reference in purple. For the non-degenerate entangled photon spectrum (Fig. B.4), a scattered signal is measured that correlates with the wings of the spectrum, well away from the expected fluorescence spectrum. When a degenerate spectrum with a bandwidth centered at 800 nm is used, farther away from the R6G absorption tail, a reduced amplitude scatter at 800 nm is measured. The scattered spectrum that is measured is a convolution of the wavelength dependent molecular scattering cross section and the SPDC signal which is why it does not appear identical to Fig. B.4. As a control, zinc tetraphenylporphyrin (ZnTPP) was measured because it has a narrow-band absorption at 400 nm that is $\sim$ 200 nm from the SPDC spectrum as well as a much weaker absorption near 550 nm (aligned with R6G). No scattered signal was measured for ZnTPP within the sensitivity limit of our spectrometer, which may be expected because ZnTPP has a lower absorption cross section than R6G, but other factors regarding the nature of the scattering process may come into play. All light is transmitted within our error bars and Fig. B.7 represents the dark count fluctuations of the EMICCD. At this point, the exact nature of the scattering mechanism is unknown, but the scattered spectrum and its single-photon time dependence are clearly measured.

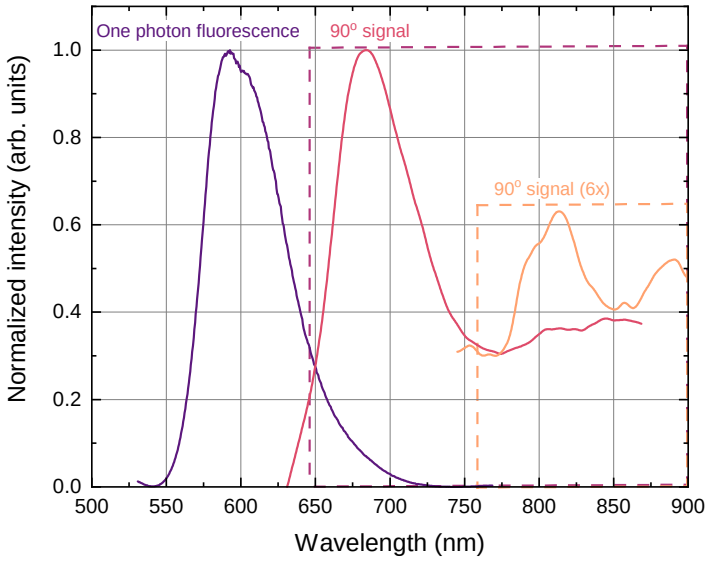

Figure 4.4: One photon fluorescence (purple trace) and the measured scatter spectra from 5mM R6G in ethanol for non-degenerate (pink trace) and degenerate (orange trace) entangled photons. The spectra have been normalized and scaled such that they can be displayed on similar scales. The scattered signal matches the entangled photon spectrum indicating that a one-photon process is present, and not fluorescence from an entangled two-photon process.

4.5 Results: Measured entangled photon interaction cross sections

The scattered cross section is calculated using the equation [33]:

$$S_E = \gamma * N_E * c * 10^{-6} * l * N_a * \sigma_E \tag{4.1}$$

where S_E is the collected scatter signal, γ is the collection efficiency, N_E is the incident entangled photon flux, c is the concentration in mM, l is the pathlength in cm, N_A is Avogadro's number, and σ_E is the entangled two-photon absorption cross section. The resulting scattered cross section is $2 \pm 1 * 10^{-21}$ cm^2/molecule. For comparison, the measured attenuation from a transmission spectrum (Fig. 4.5), the standard method of the field, yields a cross section of $4 \pm 1 * 10^{-21}$ cm^2/molecule cross section (See the supplementary information for more information on the measurement). The agreement between the measured scattered cross section and the measured attenuation cross section further confirms that no entanglement enhanced two-photon absorption or fluorescence is measured.

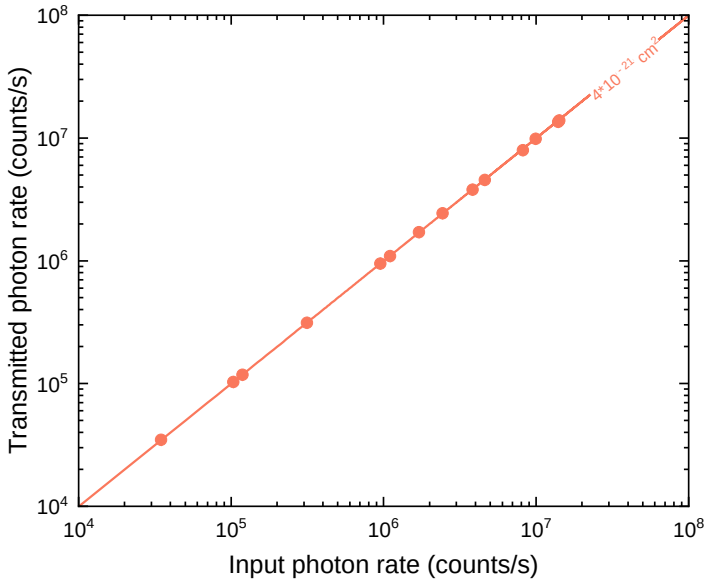

Figure 4.5: Measured transmitted photon rate (orange data points) and fit (orange solid line) vs input photon rate for 5mM Rhodamine 6G in water. Using the method standard in literature, the ETPA cross section from the measured absorption rate would be $4 \pm 1 * 10^{-21}$ cm^2/molecule. However, from these experiments, the linear relationship is determined to not be from ETPA, but rather from a single photon scattering process. Note that the error bars for each data point are on the order of the graph point size.

4.6 Conclusion

Our measurements indicate that off- or near-resonant scattering can lead to inflated absorption cross sections in intensity counting transmission, coincidence, or fluorescence experiments. The measured values are also above the maximum theoretical ETPA cross sections for R6G from quantum-mechanical derivations ($3 * 10^{-24}$ cm^2/molecule, dashed line in Fig. 4.1) [36]. The results are also in-line with the measurements of Parzuchowski et al. [34], where no signal was measured after extensive filtering and an ETPA cross section upper limit of $1.2 * 10^{-25}$ cm^2/molecule was established for R6G. Note again that our spectrometer is capable of measuring cross sections down to the 10^{-25} cm^2/molecule range, so if present, a fluorescence event would be detectable by these guidelines. The 10^{-25} cm^2/molecule sensitivity is estimated based on the noise floor of the detector and the maximum possible photon count before detector saturation. At this sensitivity, we estimate the maximum fluorescence count rate, including collection efficiency, to be approximately 5-10 photons/s. The linear dependence measurement of Fig. 4.5 also covers input

powers spanning four orders of magnitude, well beyond the intensity range reported in most manuscripts. The slope over this range is not completely linear but also not completely quadratic. If measured over a smaller range, the slope would appear linear, in agreement with previous reports. The scattered signal at 90 degrees, if not properly filtered, and measured sparsely, would also represent a signal that appears to match the entanglement time — emphasizing the importance of spectral and temporal measurements.

The measurements in this paper are performed on a virtual-state mediated two-photon excitable molecule. Recently, theoretical and experimental measurements have emphasized the importance of resonant or near resonant real states to achieve large two-photon entangled interactions [43, 44, 51]. The results of this paper indicate that caution must be taken when measuring entangled two-photon events because single-photon scattering and other reported single-photon processes such as hot band absorption [52] will mimic linear absorption at low power. Only by characterizing the entangled state, instead of relying solely on intensity measurements, can a definitive conclusion be reached. As the field of excited state entangled interactions continues to be explored, and molecules are synthesized to maximize entangled interactions, a standardized measurement scheme, such the one as presented here, is vital.

4.7 Experimental details

Broadband energy-time entangled photon pairs are generated via spontaneous parametric down-conversion of pump photons in a custom made periodically poled 8% MgO doped congruent lithium tantalate (CLT) bulk crystal (HC Photonics). The grating design is optimized for the Type-0 collinear quasi-phase matching condition and the poling period is 9.5 μm. The design and characterization of the grating has been previously reported [42]. The crystal is pumped by a continuous wave diode laser that outputs 400 mW of 406 nm light with a linewidth of 1.5 nm (Coherent OBIS). The polarization state of the diode laser is conditioned with a polarization beamsplitter and half-wave plate (Thorlabs) before the beam is focused into the crystal with a UV fused silica plano-convex lens. The temperature of the ppLT grating is maintained at phase-matching temperatures to an accuracy of 10 mK with a heater and PID loop (Covesion). After creation, the entangled photon pairs are passed through a total of three OD-4 500nm longpass filters (Edmund Optics) to eliminate any residual 406 nm pump photons.

For the static transmission and 90-degree signal measurements, the SPDC flux is focused into a cuvette containing Rhodamine 6G and the transmission or 90-degree signal is collected with a lens system to image with a spectrometer and an electron multiplying intensified CCD camera (PIMAX4, Princeton Instruments). The pump power is varied with a continuously variable ND wheel (Thorlabs) and monitored with a power meter (Newport). Additional longpass filters ensured that stray pump photons did not reach the EMICCD.

Time-resolved entangled state characterization was performed by first collimating the entangled photon pairs with an off-axis parabolic mirror and cylindrical lens. Following the collimation optics, the entangled pairs are directed into a two-photon Michelson interferometer [47, 48]. This configuration is chosen over the Mach-Zehnder configuration as it enables a broader bandwidth of entangled photon pairs to be utilized in a simpler collinear geometry. A broadband, dispersion compensating beamsplitter (BS1, Layertec) probabilistically separates the entangled photon pairs and directs them to two sets of mirrors, which then reflect the photons such that they are spatially overlapped on the beamsplitter. In one arm, an achromatic quarter-wave plate (Thorlabs) rotates the polarization state of the entangled pairs. In the other arm, the optical path length is adjusted by scanning a mirror mounted on a translation stage (Newport), with a minimum 0.1 μm resolution that translates to a temporal resolution of 0.33 fs.

Coincidence counts are collected using a second broadband, dispersion compensating beamsplitter (Layertec) and two free-space-to-fiber setups that couple entangled photon pairs into single photon avalanche photodiodes (SPADs, Laser Component COUNT) connected to time-tagging electronics (PicoHarp 300). The free-space-to-fiber setups each consist of two mirrors to align the output paths of the second beamsplitter into a 4.51 mm focal length asphere (Thorlabs), which then focuses the SPDC into a multimode fiber (105 μm core diameter, 0.22 NA). A 500 nm longpass filter is placed before the asphere to ensure that stray pump light is not collected. For fourth-order interference measurements, the coincidence time-bin resolution is set to 8 ps and a coincidence histogram is collected at each stage position over an integration time of 5 seconds. Accidental coincidence counts are calculated by averaging the tail of each histogram and subtracting the average value from the entire histogram. The coincidence counts are then summed within a 14 ns window.

A volumetric pipette (Eppendorf) was used to add absolute ethanol (Sigma-Aldrich) to a vial containing powdered Rhodamine 6G (Sigma-Aldrich) to achieve desired concentrations.

References

1. Jedrkiewicz, O., Blanchet, J.-L., Brambilla, E., Di Trapani, P. & Gatti, A. Detection of the Ultranarrow Temporal Correlation of Twin Beams via Sum-Frequency Generation. *Physical Review Letters* **108,** 253904. https://link.aps.org/doi/10.1103/PhysRevLett.108.253904 (2012).

2. Bondani, M., Allevi, A., Zambra, G., Paris, M. G. A. & Andreoni, A. Sub-shot-noise photon-number correlation in a mesoscopic twin beam of light. *Physical Review A* **76,** 013833. https://link.aps.org/doi/10.1103/PhysRevA.76.013833 (2007).

3. Brida, G., Genovese, M. & Ruo Berchera, I. Experimental realization of sub-shot-noise quantum imaging. *Nature Photonics* **4,** 227–230. https://www.nature.com/articles/nphoton.2010.29 (2010).

4. Giovannetti, V., Lloyd, S. & Maccone, L. Advances in quantum metrology. *Nature Photonics* **5,** 222–229. https://www.nature.com/articles/nphoton.2011.35 (2011).

5. Boto, A. N. *et al.* Quantum Interferometric Optical Lithography: Exploiting Entanglement to Beat the Diffraction Limit. *Physical Review Letters* **85,** 2733–2736. https://link.aps.org/doi/10.1103/PhysRevLett.85.2733 (2000).

6. Bornman, N. *et al.* Ghost imaging using entanglement-swapped photons. *npj Quantum Information* **5,** 1–6. https://www.nature.com/articles/s41534-019-0176-5 (2019).

7. Aspden, R. S., Tasca, D. S., Boyd, R. W. & Padgett, M. J. EPR-based ghost imaging using a single-photon-sensitive camera. *New Journal of Physics* **15,** 073032. https://doi.org/10.1088%2F1367-2630%2F15%2F7%2F073032 (2013).

8. Kviatkovsky, I., Chrzanowski, H. M., Avery, E. G., Bartolomaeus, H. & Ramelow, S. Microscopy with undetected photons in the mid-infrared. *Science Advances.* https://www.science.org/doi/abs/10.1126/sciadv.abd0264 (2020).

9. Padgett, M. J. & Boyd, R. W. An introduction to ghost imaging: quantum and classical. *Philosophical Transactions of the Royal Society A: Mathematical, Physical and Engineering Sciences* **375,** 20160233. https://royalsocietypublishing.org/doi/10.1098/rsta.2016.0233 (2017).

10. Abouraddy, A. F., Stone, P. R., Sergienko, A. V., Saleh, B. E. A. & Teich, M. C. Entangled-Photon Imaging of a Pure Phase Object. *Physical Review Letters* **93,** 213903. https://link.aps.org/doi/10.1103/PhysRevLett.93.213903 (2004).

11. Pittman, T. B., Shih, Y. H., Strekalov, D. V. & Sergienko, A. V. Optical imaging by means of two-photon quantum entanglement. *Physical Review A* **52,** R3429–R3432. https://link.aps.org/doi/10.1103/PhysRevA.52.R3429 (1995).

12. Strekalov, D. V., Sergienko, A. V., Klyshko, D. N. & Shih, Y. H. Observation of Two-Photon "Ghost" Interference and Diffraction. *Physical Review Letters* **74,** 3600–3603. https://link.aps.org/doi/10.1103/PhysRevLett.74.3600 (1995).

13. Li, B. & Hofmann, H. F. Energy-time entanglement and intermediate-state dynamics in two-photon absorption. *Physical Review A* **104,** 022434. https://link.aps.org/doi/10.1103/PhysRevA.104.022434 (2021).

14. Carnio, E., Buchleitner, A. & Schlawin, F. How to optimize the absorption of two entangled photons. *SciPost Physics Core* **4,** 028. https://scipost.org/10.21468/SciPostPhysCore.4.4.028 (2021).

15. Lerch, S. & Stefanov, A. Experimental requirements for entangled two-photon spectroscopy. *The Journal of Chemical Physics* **155,** 064201. https://aip.scitation.org/doi/10.1063/5.0050657 (2021).

16. Svidzinsky, A. *et al.* Enhancing stimulated Raman excitation and two-photon absorption using entangled states of light. *Physical Review Research* **3,** 043029. https://link.aps.org/doi/10.1103/PhysRevResearch.3.043029 (2021).

17. Lee, D.-I. & Goodson, T. Entangled Photon Absorption in an Organic Porphyrin Dendrimer. *The Journal of Physical Chemistry B* **110,** 25582–25585. https://pubs.acs.org/doi/10.1021/jp066767g (2006).

18. Dorfman, K. E., Schlawin, F. & Mukamel, S. Nonlinear optical signals and spectroscopy with quantum light. *Reviews of Modern Physics* **88,** 045008. https://link.aps.org/doi/10.1103/RevModPhys.88.045008 (2016).

19. Varnavski, O. & Goodson, T. Two-Photon Fluorescence Microscopy at Extremely Low Excitation Intensity: The Power of Quantum Correlations. *Journal of the American Chemical Society* **142** (2020).

20. Ma, J. *et al.* Nonlinear Lithium Niobate Metasurfaces for Second Harmonic Generation. *Laser & Photonics Reviews* **15,** 2000521. https://onlinelibrary.wiley.com/doi/10.1002/lpor.202000521 (2021).

21. Kim, J.-H., Aghaeimeibodi, S., Carolan, J., Englund, D. & Waks, E. Hybrid integration methods for on-chip quantum photonics. *Optica* **7,** 291. https://www.osapublishing.org/abstract.cfm?URI=optica-7-4-291 (2020).

22. Javid, U. A. *et al.* Ultrabroadband Entangled Photons on a Nanophotonic Chip. *Physical Review Letters* **127,** 183601. https://link.aps.org/doi/10.1103/PhysRevLett.127.183601 (2021).

23. Javanainen, J. & Gould, P. L. Linear intensity dependence of a two-photon transition rate. *Physical Review A* **41,** 5088–5091. https://link.aps.org/doi/10.1103/PhysRevA.41.5088 (1990).

24. Dayan, B. Theory of two-photon interactions with broadband down-converted light and entangled photons. *Physical Review A* **76,** 043813. https://link.aps.org/doi/10.1103/PhysRevA.76.043813 (2007).

25. Georgiades, N. P., Polzik, E. S., Edamatsu, K., Kimble, H. J. & Parkins, A. S. Nonclassical Excitation for Atoms in a Squeezed Vacuum. *Physical Review Letters* **75,** 3426–3429. https://link.aps.org/doi/10.1103/PhysRevLett.75.3426 (1995).

26. Harpham, M. R., Suzer, O., Ma, C.-Q., Bauerle, P. & Goodson, T. Thiophene Dendrimers as Entangled Photon Sensor Materials. *Journal of the American Chemical Society* **131,** 973–979. https://doi.org/10.1021/ja803268s (2009).

27. Guzman, A. R., Harpham, M. R., Suzer, O., Haley, M. M. & Goodson, T. G. Spatial Control of Entangled Two-Photon Absorption with Organic Chromophores. *Journal of the American Chemical Society* **132,** 7840–7841. https://doi.org/10.1021/ja1016816 (2010).

28. Upton, L. *et al.* Optically Excited Entangled States in Organic Molecules Illuminate the Dark. *The Journal of Physical Chemistry Letters* **4,** 2046–2052. https://doi.org/10.1021/jz400851d (2013).

29. Villabona-Monsalve, J. P., Calderón-Losada, O., Nuñez Portela, M. & Valencia, A. Entangled Two Photon Absorption Cross Section on the 808 nm Region for the Common Dyes Zinc Tetraphenylporphyrin and Rhodamine B. *The Journal of Physical Chemistry A* **121,** 7869–7875. https://doi.org/10.1021/acs.jpca.7b06450 (2017).

30. Villabona-Monsalve, J. P., Varnavski, O., Palfey, B. A. & Goodson, T. I. Two-Photon Excitation of Flavins and Flavoproteins with Classical and Quantum Light. *Journal of the American Chemical Society* **140,** 14562–14566. https://doi.org/10.1021/jacs.8b08515 (2018).

31. Eshun, A., Cai, Z., Awies, M., Yu, L. & T. Goodson, I. I. I. Investigations of Thienoacene Molecules for Classical and Entangled Two-Photon Absorption. *The Journal of Physical Chemistry A* (2018).

32. Villabona-Monsalve, J. P., Burdick, R. K. & Goodson, T. I. Measurements of Entangled Two-Photon Absorption in Organic Molecules with CW-Pumped Type-I Spontaneous Parametric Down-Conversion. *The Journal of Physical Chemistry C* **124,** 24526–24532. https://doi.org/10.1021/acs.jpcc.0c08678 (2020).

33. Tabakaev, D. *et al.* Energy-time-entangled two-photon molecular absorption. *Physical Review A* **103,** 033701. https://link.aps.org/doi/10.1103/PhysRevA.103.033701 (2021).

34. Parzuchowski, K. M. *et al.* Setting Bounds on Entangled Two-Photon Absorption Cross Sections in Common Fluorophores. *Physical Review Applied* **15,** 044012. https://link.aps.org/doi/10.1103/PhysRevApplied.15.044012 (2021).

35. Landes, T. *et al. Experimental Bounds on Entangled Two Photon Absorption in Rhodamine 6G* in *Conference on Lasers and Electro-Optics (2021), paper FM3N.3* (2021), FM3N.3. https://opg.optica.org/abstract.cfm?uri=CLEO_QELS-2021-FM3N.3.

36. Landes, T. *et al.* Quantifying the enhancement of two-photon absorption due to spectral-temporal entanglement. *Optics Express* **29,** 20022–20033. https://opg.optica.org/oe/abstract.cfm?uri=oe-29-13-20022 (2021).

37. Burdick, R. K., Schatz, G. C. & Goodson, T. I. Enhancing Entangled Two-Photon Absorption for Picosecond Quantum Spectroscopy. *Journal of the American Chemical Society* **143,** 16930–16934. https://doi.org/10.1021/jacs.1c09728 (2021).

38. Corona-Aquino, S. *et al.* Experimental study on the effects of photon-pair temporal correlations in entangled two-photon absorption. *arXiv:2101.10987 [physics, physics:quant-ph].* http://arxiv.org/abs/2101.10987 (2021).

39. Shim, S., Stuart, C. M. & Mathies, R. A. Resonance Raman Cross-Sections and Vibronic Analysis of Rhodamine 6G from Broadband Stimulated Raman Spectroscopy. *ChemPhysChem* **9,** 697–699. https://onlinelibrary.wiley.com/doi/abs/10.1002/cphc.200700856 (2008).

40. Makarov, N. S., Drobizhev, M. & Rebane, A. Two-photon absorption standards in the 550–1600 nm excitation wavelength range. *Optics Express* **16,** 4029–4047. https://www.osapublishing.org/oe/abstract.cfm?uri=oe-16-6-4029 (2008).

41. Albota, M. A., Xu, C. & Webb, W. W. Two-photon fluorescence excitation cross sections of biomolecular probes from 690 to 960 nm. *Applied Optics* **37,** 7352–7356. https://www-osapublishing-org.caltech.idm.oclc.org/ao/abstract.cfm?uri=ao-37-31-7352 (1998).

42. Szoke, S., He, M., Hickam, B. P. & Cushing, S. K. Designing High-Power, oOctave Spanning Entangled Photon Sources for Quantum Spectroscopy. *The Journal of Chemical Physics* **154,** 244201. https://aip.scitation.org/doi/10.1063/5.0053688 (2021).

43. Burdick, R. K. *et al.* Predicting and Controlling Entangled Two-Photon Absorption in Diatomic Molecules. *The Journal of Physical Chemistry A* **122,** 8198–8212. https://doi.org/10.1021/acs.jpca.8b07466 (2018).

44. Kang, G. *et al.* Efficient Modeling of Organic Chromophores for Entangled Two-Photon Absorption. *Journal of the American Chemical Society* **142,** 10446–10458. https://doi.org/10.1021/jacs.0c02808 (2020).

45. Fischer, M. & Georges, J. Fluorescence quantum yield of rhodamine 6G in ethanol as a function of concentration using thermal lens spectrometry. *Chemical Physics Letters* **260,** 115–118. https://www.sciencedirect.com/science/article/pii/000926149600838X (1996).

46. Zehentbauer, F. M. *et al.* Fluorescence spectroscopy of Rhodamine 6G: Concentration and solvent effects. *Spectrochimica Acta Part A: Molecular and Biomolecular Spectroscopy* **121,** 147–151. https://www.sciencedirect.com/science/article/pii/S1386142513012195 (2014).

47. Lavoie, J. *et al.* Phase-Modulated Interferometry, Spectroscopy, and Refractometry using Entangled Photon Pairs. *Advanced Quantum Technologies* **3,** 1900114. http://onlinelibrary.wiley.com/doi/abs/10.1002/qute.201900114 (2020).

48. Lopez-Mago, D. & Novotny, L. Coherence measurements with the two-photon Michelson interferometer. *Physical Review A* **86,** 023820. https://link.aps.org/doi/10.1103/PhysRevA.86.023820 (2012).

49. Shoji, I., Kondo, T., Kitamoto, A., Shirane, M. & Ito, R. Absolute scale of second-order nonlinear-optical coefficients. *J. Opt. Soc. Am. B* **14,** 2268. https://opg.optica.org/abstract.cfm?URI=josab-14-9-2268 (1997).

50. Varnavski, O., Pinsky, B. & Goodson, T. Entangled Photon Excited Fluorescence in Organic Materials: An Ultrafast Coincidence Detector. *The Journal of Physical Chemistry Letters* **8,** 388–393. https://doi.org/10.1021/acs.jpclett.6b02378 (2017).

51. Gu, B., Keefer, D. & Mukamel, S. Wave Packet Control and Simulation Protocol for Entangled Two-Photon Absorption of Molecules. *Journal of Chemical Theory and Computation* **18,** 406–414. https://doi.org/10.1021/acs.jctc.1c00949 (2022).

52. Mikhaylov, A. *et al.* Hot-Band Absorption Can Mimic Entangled Two-Photon Absorption. *The Journal of Physical Chemistry Letters* **13,** 1489–1493. https://doi.org/10.1021/acs.jpclett.1c03751 (2022).

Chapter 5

EXPERIMENTAL UPPER BOUNDS FOR RESONANCE-ENHANCED ENTANGLED TWO-PHOTON ABSORPTION CROSS SECTION OF INDOCYANINE GREEN

ABSTRACT

Resonant intermediate states have been proposed to increase the efficiency of entangled two-photon absorption (ETPA). Although resonance-enhanced ETPA (r-ETPA) has been demonstrated in atomic systems using bright squeezed vacuum, it has not been studied in organic molecules. We investigate for the first time r-ETPA in an organic molecular dye, indocyanine green (ICG), when excited by broadband entangled photons in near-IR. Similar to many reported virtual state mediated ETPA (v-ETPA) measurements, no r-ETPA signals are measured, with an experimental upper bound for the cross section placed at $6(\pm 2) \times 10^{-23}$ cm^2. In addition, the classical resonance-enhanced two-photon absorption (r-TPA) cross section of ICG at 800 nm is measured for the first time to be $20(\pm 13)$ GM, where 1 GM equals 10^{-50} cm^4 s, suggesting that having a resonant intermediate state does not significantly enhance two-photon processes in ICG. The spectrotemporally resolved emission signatures of ICG excited by entangled photons are also presented to support this conclusion.

Most of this chapter has been reproduced with permission from:

He, M. *et al.* Experimental Upper Bounds for Resonance-Enhanced Entangled Two-Photon Absorption Cross Section of Indocyanine Green. *The Journal of Chemical Physics,* Accepted (2024).

5.1 Introduction

Research on molecular entangled two-photon absorption (ETPA) has gained momentum over the past decade due to its potential application in nonlinear spectroscopy and bioimaging. While multiple theoretical predictions on ETPA cross sections have been made [1–7], the predicted values vary by orders of magnitude, and the formulations emphasize different parameters of the excitation process. Although reported ETPA cross sections [8–10] could be as high as 1×10^{-17} cm^2, recent measurements of ETPA cross sections reported values lower than 1×10^{-21} cm^2 for organic molecules with virtual intermediate states, even in dyes with near-unity quantum yields which facilitate fluorescence detection such as rhodamine 6G (R6G) [11–15], and quantum dot systems with large classical two-photon absorption (TPA) cross sections [16]. The measured fluorescence signals from ETPA are usually in the tens per second to tens per hour count rate range, which hinders many potential applications in imaging and sensing.

For classical TPA, it is known that a real intermediate state increases the cross section by 1-2 orders of magnitude depending on the frequency and bandwidth of the excitation laser [17–21]. Resonance-enhanced ETPA (r-ETPA) is predicted to be enhanced by similar orders of magnitude in atoms [5, 22–24] and molecules [1]. While r-ETPA in atomic cesium [25] and atomic rubidium [26] have been observed when excited by bright squeezed vacuum, the quantum enhancement on the resonance-enhanced TPA (r-TPA) cross sections was not quantified. Moreover, atoms generally have classical TPA cross sections in the range of 10^{-40} – 10^{-35} cm^4 s, which are 7-15 orders of magnitude larger than those of organic molecules (10^{-50} – 10^{-47} cm^4 s) [17, 27–31]. Atoms also have longer-lived excited state coherences than molecules, evidenced by the homogeneous linewidths of atoms, [32–37] which could facilitate coherent biphoton processes. To date, experimental studies in organic molecules have only focused on virtual state-mediated ETPA (v-ETPA) instead of r-ETPA processes [2, 8–12, 14, 38–50].

The experimental challenge in measuring molecular r-ETPA is that signals from the first singlet excited state (S1) can mask signals from the subsequent, weaker excitation to the second singlet excited state (S2). Traditional TPA measurement approaches such as transmission measurements, pump versus pairs power attenuation test [11, 14, 51], and z-scans [52–54] therefore become more difficult. Indocyanine green (ICG), however, is a unique case for r-ETPA because it has both an S1-S0 emission at ~850 nm and an S2-S0 emission at ~550 nm [55–57], as shown in

Fig. 5.1. The S2:S1 fluorescence ratio allows quantitative comparison between the r-ETPA cross section and the classical one-photon absorption cross section. ICG is also important in medical imaging as the first FDA-approved near-IR contrast agent [58]. Although traditionally used as a one-photon dye, ICG will have further medical applications in deep tissue imaging if it exhibits significantly enhanced r-ETPA.

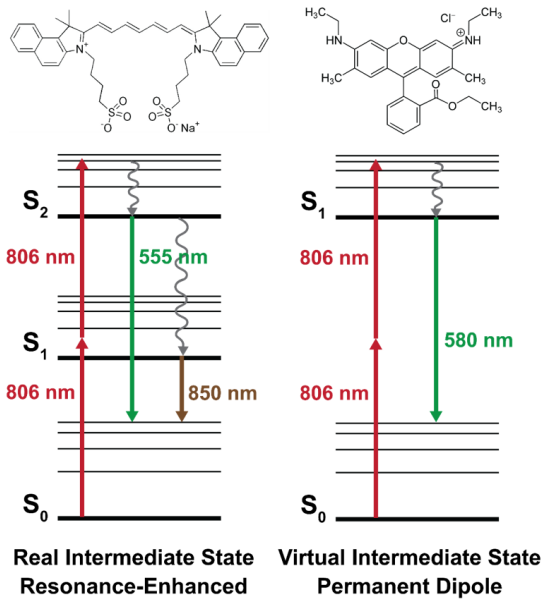

Figure 5.1: Jablonski diagram comparison between r-ETPA in ICG (left) and v-ETPA in R6G (right). Emission wavelengths are measured from 1 mM solutions in dimethyl sulfoxide (DMSO).

In this work, spectrotemporally resolved emission signatures of ICG are measured when photoexcited by broadband entangled photons in the near-IR region. No r-ETPA signals are measured within the detection limits of the measurements, allowing us to place an experimental upper bound on the r-ETPA cross section per molecule of ICG at $6(\pm 2) \times 10^{-23}$ cm^2. For comparison, the classical r-TPA cross section at 800 nm is also measured for the first time to be $20(\pm 13)$ GM where 1 GM equals 10^{-50} cm^4 s. The results suggest that having a resonant intermediate state does not significantly enhance the ETPA cross section of ICG in this case. The findings indicate that current measurement schemes with non-diffraction-limited focusing conditions, $< 1\%$ fluorescence collection efficiencies, and < 10 photons/s dark counts are not sufficiently sensitive for detecting r-ETPA signals in organic

molecules with < 20 GM classical TPA cross sections. The measured classical r-TPA cross section may still be useful for future imaging and sensing applications.

5.2 Methods

Measuring r-ETPA cross sections

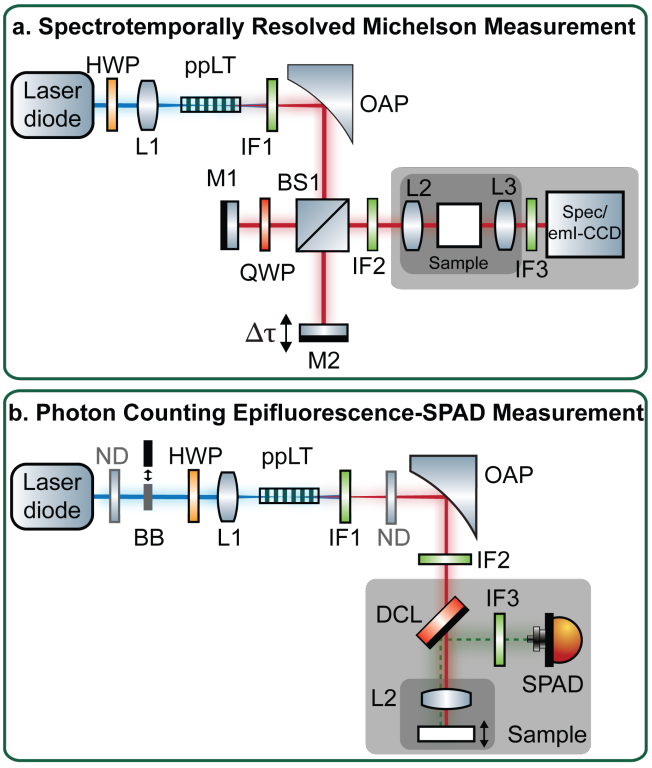

Figure 5.2: Experimental setups used in this work. a) A spectrotemporally resolved Michelson interference scheme with a grating spectrometer and emICCD. Fluorescence is collected along the direction of excitation beam propagation. b) A single-photon counting, epifluorescence scheme with a fiber-coupled SPAD as the detector. The gray shaded areas in both diagrams indicate physically sealed barriers that minimize scatter and ambient noise. HWP: half-wave plate, L: lens, ppLT: periodically-poled lithium tantalate, IF: interference filter set, OAP: off-axis parabolic mirror, BS: thin plate beamsplitter, QWP: quarter-wave plate, M: mirror, BD: beam dump, ND: neutral density filter wheel, BB: motorized beam block, DCL: dichroic longpass filter.

A previously described continuous-wave (CW) laser-pumped, broadband entangled photon source is used in the experiments [15, 59]. Briefly, as shown in Fig. 5.2, a 400-mW CW laser diode (Coherent) with a center wavelength of 403 nm is focused by a 400 mm plano-convex lens through a temperature-controlled Type 0 periodically

poled lithium tantalate (ppLT) crystal. This produces collinear entangled photons centered around 806 nm with a bandwidth of ~200 nm via spontaneous parametric down-conversion (SPDC). To minimize hot-band absorption [14] and one-photon scatter [15], edgepass filters are used to limit the bandwidth of the entangled photon excitation to 750-850 nm. Coincidence counting within the linear response range of the single photon avalanche diodes (SPAD, Laser Components) is used to verify that SPDC pairs rate scales linearly with pump power and to derive the maximum pairs rate [60]. The maximum SPDC pairs rate used here is 1.9×10^{10} pairs/s, corresponding to 9.2 nW of SPDC power and a down-conversion efficiency of 2.3×10^{-10}. Given the bandwidth and pairs rate, the maximum number of photons per frequency mode [51], n, is 4×10^{-4} (supplementary information C.1). Therefore, the measurements performed in this work are well within the regime of isolated pairs.

Two different detection schemes are used to measure fluorescence from r-ETPA in ICG. Each scheme has its advantages and drawbacks. The first detection scheme, as shown in Fig. 5.2a, uses a Michelson interferometer to introduce time delays ($\Delta\tau$) between the signal and idler photons in the entangled excitation beam. A grating spectrometer and an electron-multiplying intensified charge-coupled device (emICCD, Princeton Instruments) measure any fluorescence signal. An achromatic lens with a 100 mm focal length focuses excitation beam down to < 200 μm beam waist into a 10-mm thick cuvette. The cuvette holds an aqueous solution of 1 mM ICG. The second detection scheme (Fig. 5.2b) is an epifluorescence scheme with a SPAD. Compared with literature [11], a motorized beam block is also added to the pump path that blocks and unblocks the pump laser every 1 min to allow subtraction of dark counts and eliminate drift over long integration times. Also, instead of using different optical components to vary the pump and pairs rate, there are two locations along the beam path where a continuously variable metallic neutral density (ND) filter wheel is placed. The 2-mm thick ND wheel minimally affects the direction of beam propagation and introduces negligible dispersion. An aspheric lens with a 4.51 mm focal length and 0.55 numerical aperture (NA) focuses the excitation beam down to < 35 μm beam waist into a sample cuvette, measured by a laser beam profiler (Femto Easy). The cuvette is 1 mm thick to reduce fluorescence reabsorption, and the solvent is changed to DMSO for improved quantum yield [61] while the dye concentration remains 1 mM.

The Michelson scheme eliminates false signals caused by uncorrelated photon pairs and one-photon events by analyzing the interference pattern in the spectrotemporally

recorded signal [15]. The disadvantage of the scheme is its loss and complexity. The nondeterministic splitting of the entangled pairs by the Michelson interferometer incurs a 75% loss of visibility, and the spectrometer slit and grating induces another 50% loss. The emICCD's high dark counts (1 − 1000/s/pixel) add an extra source of noise and are not ideal for detecting single photons. Overall, the interferometer's long-term instability prevents acquisition times longer than a few minutes per data point. The main advantage of the epifluorescence and SPAD measurement is that it improves fluorescence collection efficiency by at least an order of magnitude to 1.5% compared with the Michelson setup. Hours-long integration times per data point are also possible with the SPAD. The disadvantage is that the SPAD is a bucket detector and cannot discern false signals from one-photon scatter or residual pump leakage. Heavy optical filtering must instead be relied on. A total of 20 OD of optical filtering from stacked longpass filters is used to remove the 403 nm CW pump beam after SPDC. A total of 8 OD of shortpass filters are placed in front of the SPAD to minimize one-photon SPDC scatter into the detector.

Measuring classical r-TPA cross sections

To benchmark the quantum enhancement of r-ETPA, the classical r-TPA cross section of ICG at 800 nm is first measured as it is not widely reported in the literature. Two-photon fluorescence from ICG is compared with that from a reference sample of R6G with known TPA cross sections [62]. Both ICG and R6G are dissolved in DMSO and have the same concentration of 2.5 μM. The r-TPA cross section of ICG can be derived from the following formula [63]:

$$\eta_{ICG} \cdot \delta(800\text{ nm})_{ICG} = \eta_{R6G} \cdot \delta(800\text{ nm})_{R6G} \cdot \frac{F(800\text{ nm})_{ICG}}{F(800\text{ nm})_{R6G}} \cdot \left(\frac{P(800\text{ nm})_{R6G}}{P(800\text{ nm})_{ICG}}\right)^2 \quad (5.1)$$

where η is the two-photon fluorescence quantum yield of ICG or R6G, $\delta(800\text{ nm})$ is the TPA cross section of ICG or R6G at 800 nm excitation, $F(800\text{ nm})$ is the measured two-photon fluorescence intensity from ICG or R6G excited by an 800 nm laser, and $P(800\text{ nm})$ is the excitation power used on ICG or R6G.

Classical two-photon fluorescence is measured by a calibrated, commercial Zeiss LSM 880 confocal laser scanning microscope with a 140-fs pulse width multiphoton tunable laser (Coherent). The sample solution is mounted into an imaging well formed by a 1-mm thick silicone spacer (CultureWell) securely placed on a glass slide and covered by a #1.5 coverslip. The sample is then placed on the translation

stage of the microscope, where a 40x C-apochromat water immersion objective (1.2 NA) is used to excite the sample and collect fluorescence. The microscope is equipped with appropriate emission filters, a series of diffraction gratings, and 32 photomultiplier tubes for TPA fluorescence detection. The built-in photon counting mode of the microscope is used to measure the fluorescence count rate, and the measurement is averaged over 50 repetitions of 1 s integration time. The fluorescence intensity $F(800\text{ nm})$ values in Eqn. 5.1 for ICG and R6G are obtained by subtracting the background count rate of pure DMSO from the sample count rates. The excitation power $P(800\text{ nm})$ ratio between R6G and ICG is calculated from the pulsed laser output powers, assuming linear losses of the laser power through the optical path before the sample plane. Specifically, to ensure the measured classical TPA fluorescence count rates are within the photomultiplier tubes' dynamic range, a $\frac{P(800\text{ nm})_{R6G}}{P(800\text{ nm})_{ICG}}$ ratio of 0.5 is used since ICG fluorescence quantum yield is lower than that of R6G. The built-in spectral detection mode of the microscope (9 nm resolution) is also used to qualitatively measure the r-TPA fluorescence spectrum of ICG, with an optical filter cutoff at 647 nm.

5.3 Results and Discussion

Fig. 5.3 compares the emission spectrum of ICG excited by the SPDC pairs (red) with ICG's classical S2-S0 fluorescence spectrum (light blue) resulting from r-TPA and classical S1-S0 fluorescence spectrum (purple). The classical S1-S0 trace is obtained by exciting the sample with an 808 nm CW diode laser; an OD 4 longpass filter with a 812 nm cutoff is used to filter out the residual excitation beam. The cuvette scatter of SPDC (orange) is well separated from the S1-S0 fluorescence. A 403 nm CW laser is also used to excite the ICG. resultant S2-S0 and S1-S0 emission peaks (deep blue) are spectrally separated so their peak intensity ratio is used to estimate the S2-S0 fluorescence quantum yield of ICG for later calculation of the classical r-TPA cross section. Specifically, the intensity values at 555 nm (S2-S0 fluorescence peak) and 850 nm (S1-S0 fluorescence peak) are scaled by the quantum efficiencies (QEs) of the spectrometer grating [64] and CCD camera [65]. The ratio of the QE-corrected intensities is then multiplied by ICG S1-S0 fluorescence quantum yield of 0.12 in DMSO [61], resulting in an estimated ICG S2-S0 fluorescence quantum yield of 0.02. The S1-S0 peak in the dual emission spectrum (deep blue) is red shifted from the S1-S0 single emission peak (purple), potentially due to the 403 nm laser accessing different vibronic levels than 808 nm excitation. The emission spectrum from SPDC excitation (red) at 20 s

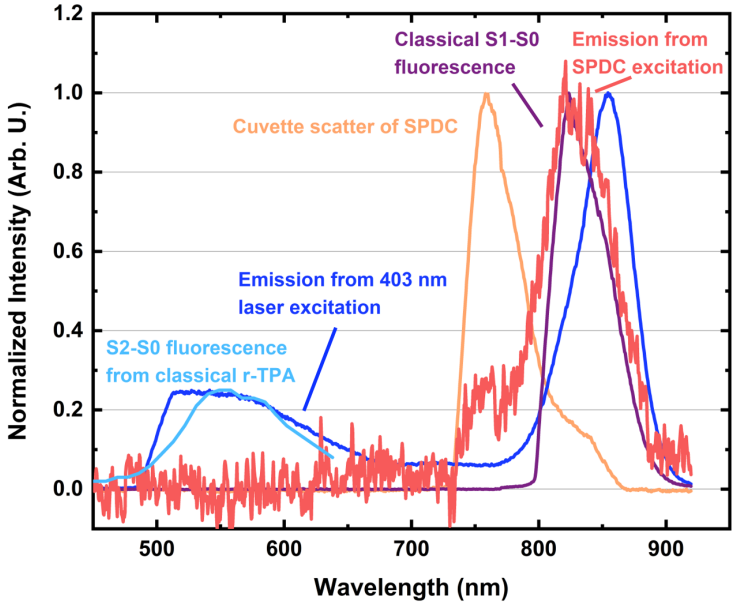

Figure 5.3: ICG fluorescence spectra when excited by an 800 nm pulsed two-photon laser (light blue), an 808 nm CW laser (purple), and the SPDC pairs (red); also showing dual fluorescence from 403 nm CW laser excitation (deep blue), as well as cuvette front scatter of SPDC (orange). All spectra except the classical TPA fluorescence are taken using the epifluorescence measurement scheme (Fig. 5.2b), with the fiber output sent to the spectrometer and emICCD. The classical TPA fluorescence spectrum is taken by the commercial two-photon absorption microscope and is cut off at 647 nm by an optical filter. These spectra are arbitrarily scaled and are not corrected for detector QEs.

integration time has an emission peak that matches the classical S1-S0 fluorescence, indicating one-photon absorption, but does not have an apparent S2-S0 emission peak, indicating the lack of TPA. Therefore, the more spectrally sensitive Michelson interference scheme (Fig. 5.2a) is employed to examine if one- versus two-photon signals can be separated.

Fig. 5.4a compares the CCD interferograms of the ICG S1-S0 (purple) and S2-S0 (red) emission regions as a function of time delay. Coincidence rates from the SPDC pairs, measured by two SPADs and a timing circuit, are also shown in orange. Each data point at a certain time delay $\Delta\tau$ in the S1-S0 emission region (820-920 nm) represents a summed signal count accumulated over 10 s, and each data point in the S2-S0 emission region (450-650 nm) represents a summed signal count accumulated over 100 s. In the two-photon coincidence interferogram, for an entangled state, the peak amplitudes are larger than the valley amplitudes near time zero, which results

from the Hong-Ou-Mandel effect [59, 66], as shown in Fig. 5.4a orange. The width of the main peak is determined by the SPDC bandwidth. As the bandwidth of the entangled photons is changed, either by varying phase matching conditions or spectral filtering, the width of the main peak, proportional to the entanglement correlation time [66], changes accordingly. In this case the correlation time is $\sim$ 50 fs. In a TPA event, the interferogram of the fluorescence will follow that of the SPDC coincidences. For a one-photon absorption event, the interferogram's peak and valley components have equal amplitudes, which is the case for the ICG S1-S0 emission pattern (Fig. 5.4a purple). On the other hand, the interferogram for the S2-S0 emission region is at or near noise level, indicating that no one- or two-photon signals exist within the spectral region despite this approach's higher signal-to-noise ratio compared with the spectral measurement of Fig. 5.3. The conclusions are further reinforced by the Fourier transforms of the interferograms in Fig. 5.4b where only the SPDC coincidences have a strong 2f peak at ~403 nm, and no peaks are measured in the S2-S0 emission region. Because the frequencies of entangled pairs add up to the pump frequency, Fourier transform of their Michelson interference will have a 2f peak at the pump frequency indicating frequency anti-correlation [66], in addition to a 1f peak at the SPDC degenerate frequency, as is shown in the SPDC coincidence Fourier transform (Fig. 5.4b orange). The Fourier transform of a fluorescence interferogram should carry the same 2f feature if ETPA events are present. As expected, the Fourier transform of the S1-S0 emission region has a single 1f peak centered at SPDC degeneracy (806 nm), corresponding to fluorescence from one-photon absorption. On the other hand, the Fourier transform of the S2-S0 emission region lacks both 2f and 1f peak, ruling out the presence of ETPA or other one-photon effects.

Finally, an epifluorescence and SPAD measurement scheme (Fig. 5.2b) is used to confirm the lack of a two-photon induced signal at even longer integration times than possible with the Michelson scheme. The approach was previously used to successfully measure v-ETPA signals of R6G with 5+ hours of integration time [11]. Error analysis is first performed using 1 mM R6G to determine the optimal integration time that stabilizes the standard deviation of the SPAD measurements. Three hundred sets of repeated measurements are used. Within each set, SPAD counts are measured for 1 minute in the laser-off configuration, followed by 1 minute of measurement in the laser-on configuration. A mean counts/s value is then calculated from each 1-min bin. The 150 repeated laser-off and 150 laser-on measurements are then analyzed separately to confirm that each accumulated standard deviation

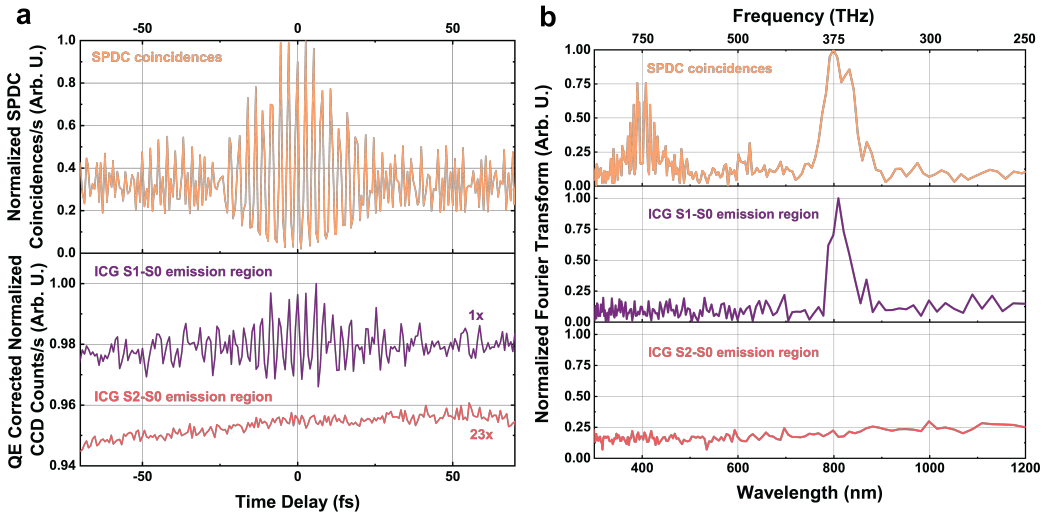

Figure 5.4: Spectrotemporally resolved, quantum efficiency corrected Michelson interferograms (a) and their Fourier transforms (b) of SPDC coincidences transmitted through a cuvette of water (orange), ICG's S1-S0 fluorescence region (purple), and ICG's S2-S0 fluorescence region (red). The Michelson interference of the SPDC pairs shows a main peak 50 fs wide, which corresponds to the entanglement correlation time [59, 66]. The interferogram also shows a side peak at negative time delays. This is due to the slight misalignment of the interferometer, as well as the asymmetric and non-Gaussian shape of the SPDC spectrum[15, 59]. The Fourier transforms show both frequency and equivalent wavelength units for ease of understanding. The Fourier transform of the interferometer pair rate exhibits a 2f peak at 403 nm, indicating frequency anti-correlation of the entangled photon state[66]. In contrast, the Fourier transforms for ICG emissions do not have 2f peaks. No two-photon events are registered by the interferograms or the Fourier transforms, ruling out the presence of r-ETPA fluorescence from ICG.

of the mean is proportional to $1/\sqrt{N}$ where N is the number of repeated 1-min measurements [67]. The data indicates that 50 min of integration time stabilizes time-dependent fluctuations and is still practical for performing multiple ETPA measurements.

Fig. 5.5a shows a comparison between the SPAD counts from 1 mM R6G, 1 mM ICG, and solvent DMSO when excited by entangled photons. A wavelength range of 500-650 nm is selected by 8 OD of interference filters at the SPAD entrance, which encompasses both ICG's S2-S0 r-TPA emission region and R6G's S1-S0 v-TPA emission region.Although each signal in Fig. 5.5a is already dark-count-subtracted, the solvent DMSO still shows positive counts, possibly indicating molecular Rayleigh scattering [68] of residual CW pump or SPDC. The ICG signal

is statistically indistinguishable from the DMSO signal, confirming that r-ETPA is undetectable with an upper bound of $6(\pm 2) \times 10^{-23}$ cm^2 for the cross section as later discussed. The R6G signal has a statistically significant signal above the solvent scatter. A pump versus pairs attenuation power study [11, 14, 51] using an ND filter wheel is performed to determine whether the signal is from one- or two-photon events. The measurement approach verifies ETPA when the fluorescence signal scales linearly with varying pump power but quadratically with pairs attenuation because the loss of one photon within an entangled pair destroys the entanglement. However, Fig. 5.5b shows that the R6G signal counts scale linearly with both pump attenuation and pairs attenuation, indicating the presence of one-photon processes such as hot-band absorption [14] instead of ETPA. While the pairs attenuation curve is shifted up with respect to the pump attenuation curve, we attribute this discrepancy as an artifact from the placement of the ND filter wheel in the beam path between pump and pair measurements. When moved, the ND wheel can alter background scatter at few photons per second levels. The results are, therefore, too close to the instrument noise floor to draw statistically sound conclusions about ETPA fluorescence in either ICG or R6G.

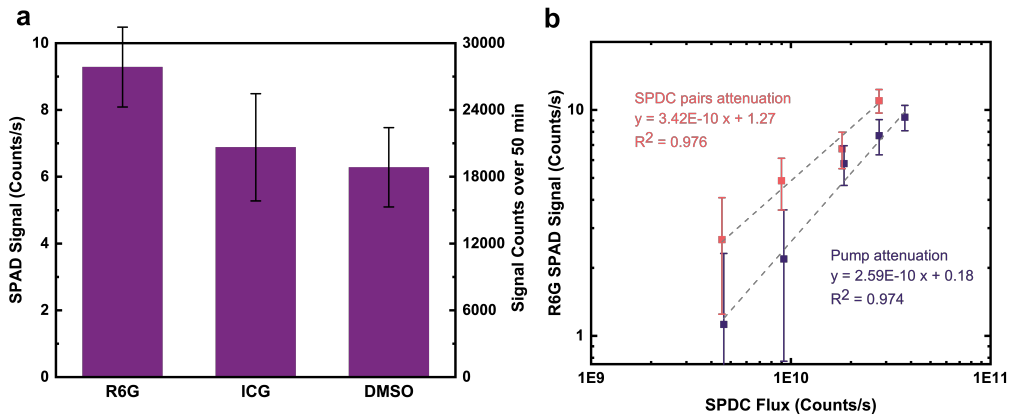

Figure 5.5: (a) SPAD signals of 1 mM R6G, 1 mM ICG, and DMSO, acquired over 50 min, in 50 repeated measurements of 1 min integration. Signal counts are calculated as laser-on counts minus laser-off counts (the total run time of each sample is, therefore, 100 min). The SPAD generates a readout every 100 ms. Each error bar is the standard deviation of the 50 measurements. ICG shows a background-level signal similar to that of DMSO, while R6G shows a statistically significant positive signal. (b) A pump versus pairs attenuation power study on R6G is conducted with the same integration times. Linear dependence on both pump and SPDC powers indicates one-photon processes such as hot-band absorption. The goodness of the linear fit is indicated by R^2 values.

Table 5.1: Summary of classical TPA cross sections and detection limits for ETPA cross sections.

Molecule	$\delta_{classical}$[a] (GM)	Michelson scheme detection limits σ_{ETPA} (cm^2)	Michelson scheme detection limits Equivalent δ_{TPA}[b] (GM)	SPAD scheme detection limits σ_{ETPA} (cm^2)	SPAD scheme detection limits Equivalent δ_{TPA}[b] (GM)
ICG	20(±13)[c]	$9(\pm2)\times10^{-23}$	$2(\pm2)\times10^{13}$	$6(\pm2)\times10^{-23}$	$3(\pm2)\times10^{12}$
R6G	20(±10)[d]	$4(\pm2)\times10^{-24}$	$8(\pm2)\times10^{11}$	$8(\pm2)\times10^{-24}$	$4(\pm2)\times10^{11}$

[a] Classical TPA cross sections.
[b] See calculation in supplementary information C.2.
[c] Measured relative to R6G $\delta_{classical}$ with 800 nm excitation.
[d] Based on literature [62, 69].

Experimental upper bounds can be placed on the r-ETPA cross section (σ_{ETPA}) of ICG based on the two measurement schemes, as summarized in Table 5.1. Each scheme's excitation flux, focusing conditions, collection efficiency, and the optical properties of ICG are used in the calculation [15] (more details see supplementary information C.2). Additionally, the classical r-TPA cross section of ICG ($\delta_{classical}$) is calculated to be 20(±13) GM according to Eqn. 5.1, and is included in the table for comparison. The measured $F(800\,\text{nm})_{ICG}$ value is 1899(±836) Hz, and the $F(800\,\text{nm})_{R6G}$ value is 22365(±429) Hz. To arrive at the $\delta(800\,\text{nm})_{ICG}$ value, the following approximations are made: 1) because reported TPA cross sections of R6G vary by up to 1 order of magnitude, regardless of solvent and excitation conditions [62, 69], 20(±10) GM is used as an estimate for $\delta(800\,\text{nm})_{R6G}$; 2) η_{ICG} is estimated as 0.02 as explained earlier; 3) η_{R6G} is approximated to be 0.95 [70, 71]. Because of the approximations, the calculated r-TPA cross section of ICG is emphasized as an order-of-magnitude estimation.

Using the excitation fluxes of the two measurement schemes, the r-ETPA cross section detection limits can be converted (supplementary information C.2) to equivalent δ_{TPA} values of $2(\pm2)\times10^{13}$ GM and $3(\pm2)\times10^{12}$ GM, as shown in Table 5.1. Comparing these values with ICG's classical r-TPA cross section of 20(±13) GM, we conclude that having a resonant intermediate state must enhance ICG's ETPA cross section by less than 11 orders of magnitude. The conclusion is supported by previous theory [1] suggesting that entanglement would only offer up to 7 orders of magnitude enhancement on the r-TPA cross section of molecules, and that r-ETPA may only be 3 orders of magnitude more enhanced than v-ETPA. The determined cross section upper limits for R6G are also listed in Table 5.1. These detection limits agree with theoretical predictions [2] and previous experiments [12, 15], suggesting that the measured upper bounds on ICG in this work are reasonable. The

Table 5.2: Theoretically predicted values for ICG σ_{ETPA}.

Reference	σ_{ETPA} (cm^2)[a]	ETPA model	Sources of broadening
Drago et al. [1]	1×10^{-28}	Molecular r-ETPA	Nonradiative decay and dephasing
Landes et al. [2]	1×10^{-30}	Molecular v-ETPA	Dephasing
Fei et al. [3]	1×10^{-31}	Atomic v-ETPA	None[b]

[a] Order of magnitude estimates, calculated based on experimental conditions used in this work (supplementary information C.3).
[b] In the “simple probabilistic model" (supplementary information C.3).

ICG detection limits differ from the R6G detection limits by ~1 order of magnitude mainly because ICG's absorption bands are broad and heavily overlap with emission bands, leading to a higher chance of fluorescence reabsorption. ICG also has a lower quantum yield than R6G. As discussed earlier, the correlation time of the entangled photons is < 50 fs, which is much shorter than the sub-ns lifetime of ICG [61]. Therefore, if present, ICG's S1-S2 transition is not significantly hindered by the decay of the intermediate state. For additional reference, predictions for the σ_{ETPA} value of ICG are also made based on three popular theoretical models for ETPA that focus on different characteristics and parameters of the ETPA process [1–3]. The results are listed in Table 5.2 and detailed calculations are available in supplementary information C.3. The theoretical models, regardless of whether real intermediate states are considered, agree that the ETPA cross section strongly depends on the frequency bandwidth of the exciting SPDC photons as well as the entanglement area. These theories also confirm that fluorescence from ICG should not be detectable with the experimental conditions used in this work.

The results are intended as upper bounds specific to the described experimental configurations, which have proven helpful in other studies of ETPA [12, 15]. Based on the theoretical predictions in Table 5.2, a 4-6 order of magnitude increase in the SPDC flux could result in a measurable r-ETPA signal, via increasing the pairs rate, increasing the bandwidth, or decreasing the focusing area. Within our bandwidth, the single-photon-per-mode limit could be maintained with an increase of 3 orders of magnitude in the SPDC power. Potential laser damage makes achieving this power difficult for the nonlinear grating used in this work. The high angular dispersion of the broadband SPDC beam makes achieving diffraction limited spot sizes also difficult [59], but this may be the most feasible route to increasing the magnitude of the excitation flux. Highly efficient periodically poled waveguides with up to 10^{-4} down-conversion efficiencies and few-μm mode field diameters [60] may be able to simultaneously achieve the broad bandwidth and spot size needed to boost signals

to experimental detection limits without exceeding laser damage thresholds in the future. If near UV to deep UV entangled photons can be created, molecules in this wavelength range can also be studied with moderately improved instrument detection limits due to higher S2-S0 fluorescence quantum yields, such as azulenes, aromatic acenes, polyenes, and metalloporphyrins [72]. Furthermore, maintaining the single-photon-per-mode limit may not even be critical for quantum-enhanced nonlinear light-matter interactions. Bright squeezed vacuum, a class of SPDC sources that saturate the single-photon-per-mode limit, are also proven to enhance two-photon absorption [25, 26], optical harmonics generation [73], and ultrafast spectroscopy [74]. Future experiments using bright squeezed vacuum sources generated in a single, waveguided spatial mode could further improve the detection limits for quantum-enhanced multiphoton processes.

5.4 Conclusion

We investigated the validity of r-ETPA in ICG and placed upper bounds on the possible enhancement. We measured the spectrotemporally resolved emission signatures of ICG excited by broadband entangled photons in near-IR. Similar to many reported v-ETPA measurements, no r-ETPA signals are measured, with an upper bound for the cross section placed at $6(\pm 2) \times 10^{-23}$ cm^2. In addition, the classical r-TPA cross section of ICG at 800 nm is measured to be 20($\pm$13) GM. The same measurements are performed on R6G for bench-marking. The results suggest that having a resonant intermediate state does not significantly enhance the ETPA cross section of ICG beyond the detection limits of this study. The findings indicate that current measurement schemes with non-diffraction-limited focusing conditions, $< 1\%$ fluorescence collection efficiencies, and < 10 photons/s dark counts are not sufficiently sensitive for detecting r-ETPA signals in organic molecules with small classical TPA cross sections. Further improvements to increase the SPDC flux and lower the instrument detection limits will be key to the successful detection of r-ETPA as well as v-ETPA signatures.

References

1. Drago, C. & Sipe, J. E. Aspects of two-photon absorption of squeezed light: The continuous-wave limit. *Physical Review A* **106,** 023115. `https://link.aps.org/doi/10.1103/PhysRevA.106.023115` (2022).

2. Landes, T. *et al.* Quantifying the enhancement of two-photon absorption due to spectral-temporal entanglement. *Optics Express* **29,** 20022–20033.

https://opg.optica.org/oe/abstract.cfm?uri=oe-29-13-20022 (2021).

3. Fei, H.-B., Jost, B. M., Popescu, S., Saleh, B. E. A. & Teich, M. C. Entanglement-Induced Two-Photon Transparency. *Physical Review Letters* **78,** 1679–1682. https://link.aps.org/doi/10.1103/PhysRevLett.78.1679 (1997).

4. Schlawin, F. Polarization-Entangled Two-Photon Absorption in Inhomogeneously Broadened Ensembles. *Frontiers in Physics* **10.** https://www.frontiersin.org/articles/10.3389/fphy.2022.848624 (2022).

5. Kang, G. *et al.* Efficient Modeling of Organic Chromophores for Entangled Two-Photon Absorption. *Journal of the American Chemical Society* **142,** 10446–10458. https://doi.org/10.1021/jacs.0c02808 (2020).

6. Burdick, R. K. *et al.* Predicting and Controlling Entangled Two-Photon Absorption in Diatomic Molecules. *The Journal of Physical Chemistry A* **122,** 8198–8212. https://doi.org/10.1021/acs.jpca.8b07466 (2018).

7. Wittkop, M., Marmolejo-Tejada, J. M. & Mosquera, M. A. Multichromatic quantum superpositions in entangled two-photon absorption spectroscopy. *Organic Electronics* **120,** 106858. https://www.sciencedirect.com/science/article/pii/S1566119923001143 (2023).

8. Harpham, M. R., Suzer, O., Ma, C.-Q., Bauerle, P. & Goodson, T. Thiophene Dendrimers as Entangled Photon Sensor Materials. *Journal of the American Chemical Society* **131,** 973–979. https://doi.org/10.1021/ja803268s (2009).

9. Guzman, A. R., Harpham, M. R., Suzer, O., Haley, M. M. & Goodson, T. G. Spatial Control of Entangled Two-Photon Absorption with Organic Chromophores. *Journal of the American Chemical Society* **132,** 7840–7841. https://doi.org/10.1021/ja1016816 (2010).

10. Upton, L. *et al.* Optically Excited Entangled States in Organic Molecules Illuminate the Dark. *The Journal of Physical Chemistry Letters* **4,** 2046–2052. https://doi.org/10.1021/jz400851d (2013).

11. Tabakaev, D. *et al.* Spatial Properties of Entangled Two-Photon Absorption. *Physical Review Letters* **129,** 183601. https://link.aps.org/doi/10.1103/PhysRevLett.129.183601 (2022).

12. Parzuchowski, K. M. *et al.* Setting Bounds on Entangled Two-Photon Absorption Cross Sections in Common Fluorophores. *Physical Review Applied* **15,** 044012. https://link.aps.org/doi/10.1103/PhysRevApplied.15.044012 (2021).

13. Landes, T. *et al.* Experimental feasibility of molecular two-photon absorption with isolated time-frequency-entangled photon pairs. *Physical Review Research* **3,** 033154. https://link.aps.org/doi/10.1103/PhysRevResearch.3.033154 (2021).

14. Mikhaylov, A. *et al.* Hot-Band Absorption Can Mimic Entangled Two-Photon Absorption. *The Journal of Physical Chemistry Letters* **13,** 1489–1493. https://doi.org/10.1021/acs.jpclett.1c03751 (2022).

15. Hickam, B. P., He, M., Harper, N., Szoke, S. & Cushing, S. K. Single-Photon Scattering Can Account for the Discrepancies among Entangled Two-Photon Measurement Techniques. *The Journal of Physical Chemistry Letters,* 4934–4940. https://pubs.acs.org/doi/10.1021/acs.jpclett.2c00865 (2022).

16. Gäbler, T. B., Hendra, P., Jain, N. & Gräfe, M. Photon Pair Source based on PPLN-Waveguides for Entangled Two-Photon Absorption. *Advanced Physics Research,* 2300037. https://onlinelibrary.wiley.com/doi/abs/10.1002/apxr.202300037 (2023).

17. Terenziani, F., Katan, C., Badaeva, E., Tretiak, S. & Blanchard-Desce, M. Enhanced Two-Photon Absorption of Organic Chromophores: Theoretical and Experimental Assessments. *Advanced Materials* **20,** 4641–4678 (2008).

18. Kobayashi, Y., Mutoh, K. & Abe, J. Stepwise two-photon absorption processes utilizing photochromic reactions. *Journal of Photochemistry and Photobiology C: Photochemistry Reviews* **34,** 2–28. https://www.sciencedirect.com/science/article/pii/S1389556717300722 (2018).

19. Drobizhev, M., Karotki, A., Kruk, M. & Rebane, A. Resonance enhancement of two-photon absorption in porphyrins. *Chemical Physics Letters* **355,** 175–182. https://www.sciencedirect.com/science/article/pii/S0009261402002063 (2002).

20. Makarov, N. *et al. Resonance enhancement of two-photon absorption of phthalocyanines for 3D optical storage in the presence of hot-band absorption* in *Organic Photonic Materials and Devices IX* **6470** (2007), 147–158. https://www.spiedigitallibrary.org/conference-proceedings-of-spie/6470/64700R/Resonance-enhancement-of-two-photon-absorption-of-phthalocyanines-for-3D/10.1117/12.696970.full.

21. Hahn, V. *et al.* Two-step absorption instead of two-photon absorption in 3D nanoprinting. *Nature Photonics* **15,** 932–938. https://www.nature.com/articles/s41566-021-00906-8 (2021).

22. Oka, H. Two-photon absorption by spectrally shaped entangled photons. *Physical Review A* **97,** 033814. https://link.aps.org/doi/10.1103/PhysRevA.97.033814 (2018).

23. Schlawin, F. & Buchleitner, A. Theory of coherent control with quantum light. *New Journal of Physics* **19,** 013009. https://dx.doi.org/10.1088/1367-2630/aa55ec (2017).

24. Li, B. & Hofmann, H. F. Enhancement of broadband entangled two-photon absorption by resonant spectral phase flips. *Physical Review A* **108,** 013706. https://link.aps.org/doi/10.1103/PhysRevA.108.013706 (2023).

25. Georgiades, N. P., Polzik, E. S., Edamatsu, K., Kimble, H. J. & Parkins, A. S. Nonclassical Excitation for Atoms in a Squeezed Vacuum. *Physical Review Letters* **75,** 3426–3429. https://link.aps.org/doi/10.1103/PhysRevLett.75.3426 (1995).

26. Dayan, B., Pe'er, A., Friesem, A. A. & Silberberg, Y. Two Photon Absorption and Coherent Control with Broadband Down-Converted Light. *Physical Review Letters* **93,** 023005. https://link.aps.org/doi/10.1103/PhysRevLett.93.023005 (2004).

27. Sulham, C. V., Pitz, G. A. & Perram, G. P. Blue and infrared stimulated emission from alkali vapors pumped through two-photon absorption. *Applied Physics B* **101,** 57–63. https://doi.org/10.1007/s00340-010-4015-9 (2010).

28. Davila, R. C. *Two-Photon Excitation of Cesium Alkali Metal Vapor 72D, 82D Kinetics and Spectroscopy* PhD thesis (Air Force Institute of Technology, 2018).

29. Bjorkholm, J. E. & Liao, P. F. Resonant Enhancement of Two-Photon Absorption in Sodium Vapor. *Physical Review Letters* **33,** 128–131. https://link.aps.org/doi/10.1103/PhysRevLett.33.128 (1974).

30. Xu, L. *et al.* Recent progress in efficient organic two-photon dyes for fluorescence imaging and photodynamic therapy. *Journal of Materials Chemistry C* **8,** 6342–6349. https://pubs.rsc.org/en/content/articlelanding/2020/tc/d0tc00563k (2020).

31. Nociarová, J. *et al.* Direct Iodination of Electron-Deficient Benzothiazoles: Rapid Access to Two-Photon Absorbing Fluorophores with Quadrupolar D-π-A-π-D Architecture and Tunable Heteroaromatic Core. *Organic Letters* **23,** 3460–3465. https://doi.org/10.1021/acs.orglett.1c00893 (2021).

32. Deutsch, C. *et al.* Spin Self-Rephasing and Very Long Coherence Times in a Trapped Atomic Ensemble. *Physical Review Letters* **105,** 020401. https://link.aps.org/doi/10.1103/PhysRevLett.105.020401 (2010).

33. Boyd, M. M. *et al.* Optical Atomic Coherence at the 1-Second Time Scale. *Science* **314,** 1430–1433. https://www.science.org/doi/full/10.1126/science.1133732 (2006).

34. Young, A. W. *et al.* Half-minute-scale atomic coherence and high relative stability in a tweezer clock. *Nature* **588,** 408–413. https://www.nature.com/articles/s41586-020-3009-y (2020).

35. Gustin, I., Kim, C. W., McCamant, D. W. & Franco, I. Mapping electronic decoherence pathways in molecules. *Proceedings of the National Academy of Sciences* **120,** e2309987120. https://www.pnas.org/doi/10.1073/pnas.2309987120 (2023).

36. Hildner, R., Brinks, D. & van Hulst, N. F. Femtosecond coherence and quantum control of single molecules at room temperature. *Nature Physics* **7,** 172–177. https://www.nature.com/articles/nphys1858 (2011).

37. Paulus, B. C., Adelman, S. L., Jamula, L. L. & McCusker, J. K. Leveraging excited-state coherence for synthetic control of ultrafast dynamics. *Nature* **582,** 214–218. https://www.nature.com/articles/s41586-020-2353-2 (2020).

38. Lee, D.-I. & Goodson, T. Entangled Photon Absorption in an Organic Porphyrin Dendrimer. *The Journal of Physical Chemistry B* **110,** 25582–25585. https://pubs.acs.org/doi/10.1021/jp066767g (2006).

39. Villabona-Monsalve, J. P., Calderón-Losada, O., Nuñez Portela, M. & Valencia, A. Entangled Two Photon Absorption Cross Section on the 808 nm Region for the Common Dyes Zinc Tetraphenylporphyrin and Rhodamine B. *The Journal of Physical Chemistry A* **121,** 7869–7875. https://doi.org/10.1021/acs.jpca.7b06450 (2017).

40. Villabona-Monsalve, J. P., Varnavski, O., Palfey, B. A. & Goodson, T. I. Two-Photon Excitation of Flavins and Flavoproteins with Classical and Quantum Light. *Journal of the American Chemical Society* **140,** 14562–14566. https://doi.org/10.1021/jacs.8b08515 (2018).

41. Eshun, A., Cai, Z., Awies, M., Yu, L. & T. Goodson, I. I. I. Investigations of Thienoacene Molecules for Classical and Entangled Two-Photon Absorption. *The Journal of Physical Chemistry A* (2018).

42. Villabona-Monsalve, J. P., Burdick, R. K. & Goodson, T. I. Measurements of Entangled Two-Photon Absorption in Organic Molecules with CW-Pumped Type-I Spontaneous Parametric Down-Conversion. *The Journal of Physical Chemistry C* **124,** 24526–24532. https://doi.org/10.1021/acs.jpcc.0c08678 (2020).

43. Tabakaev, D. *et al.* Energy-time-entangled two-photon molecular absorption. *Physical Review A* **103,** 033701. https://link.aps.org/doi/10.1103/PhysRevA.103.033701 (2021).

44. Varnavski, O. & Goodson, T. Two-Photon Fluorescence Microscopy at Extremely Low Excitation Intensity: The Power of Quantum Correlations. *Journal of the American Chemical Society* **142** (2020).

45. Landes, T. *et al. Experimental Bounds on Entangled Two Photon Absorption in Rhodamine 6G* in *Conference on Lasers and Electro-Optics (2021), paper FM3N.3* (2021), FM3N.3. https://opg.optica.org/abstract.cfm?uri=CLEO_QELS-2021-FM3N.3.

46. Burdick, R. K., Schatz, G. C. & Goodson, T. I. Enhancing Entangled Two-Photon Absorption for Picosecond Quantum Spectroscopy. *Journal of the American Chemical Society* **143,** 16930–16934. https://doi.org/10.1021/jacs.1c09728 (2021).

47. Corona-Aquino, S. *et al.* Experimental Study of the Validity of Entangled Two-Photon Absorption Measurements in Organic Compounds. *The Journal of Physical Chemistry A* **126,** 2185–2195. https://doi.org/10.1021/acs.jpca.2c00720 (2022).

48. Villabona-Monsalve, J. P. *et al.* Two-Photon Absorption in Electron Donor–Acceptor Dyads and Triads Using Classical and Entangled Photons: Potential Systems for Photon-to-Spin Quantum Transduction. *The Journal of Physical Chemistry C* **126,** 6334–6343. https://doi.org/10.1021/acs.jpcc.2c00830 (2022).

49. Triana-Arango, F., Ramos-Ortiz, G. & Ramírez-Alarcón, R. Spectral Considerations of Entangled Two-Photon Absorption Effects in Hong–Ou–Mandel Interference Experiments. *The Journal of Physical Chemistry A* **127,** 2608–2617. https://doi.org/10.1021/acs.jpca.2c07356 (2023).

50. Varnavski, O. *et al.* Colors of entangled two-photon absorption. *Proceedings of the National Academy of Sciences* **120,** e2307719120. https://www.pnas.org/doi/full/10.1073/pnas.2307719120 (2023).

51. Dayan, B., Pe'er, A., Friesem, A. A. & Silberberg, Y. Nonlinear Interactions with an Ultrahigh Flux of Broadband Entangled Photons. *Physical Review Letters* **94,** 043602. https://link.aps.org/doi/10.1103/PhysRevLett.94.043602 (2005).

52. Sengupta, P. *et al.* Sensitive measurement of absolute two-photon absorption cross sections. *The Journal of Chemical Physics* **112,** 9201–9205. https://doi.org/10.1063/1.481540 (2000).

53. Ajami, A., Husinsky, W., Liska, R. & Pucher, N. Two-photon absorption cross section measurements of various two-photon initiators for ultrashort laser radiation applying the Z-scan technique. *JOSA B* **27,** 2290–2297. https://opg.optica.org/josab/abstract.cfm?uri=josab-27-11-2290 (2010).

54. Nag, A., De, A. K. & Goswami, D. Two-photon cross-section measurements using an optical chopper: z-scan and two-photon fluorescence schemes. *Journal of Physics B: Atomic, Molecular and Optical Physics* **42,** 065103. https://dx.doi.org/10.1088/0953-4075/42/6/065103 (2009).

55. Kumari, A. & Gupta, S. Two-photon excitation and direct emission from S2 state of U.S. Food and Drug Administration approved near-infrared dye: Application of anti-Kasha's rule for two-photon fluorescence imaging. *Journal of Biophotonics* **12,** e201800086. http://onlinelibrary.wiley.com/doi/abs/10.1002/jbio.201800086 (2019).

56. Das, D. K., Makhal, K., Singhal, S. & Goswami, D. Polarization induced control of multiple fluorescence from a molecule. *Chemical Physics Letters* **579,** 45–50. https://www.sciencedirect.com/science/article/pii/S0009261413008026 (2013).

57. Pu, Y., Shi, L., Pratavieira, S. & Alfano, R. R. *Enhancing the depth of tissue microscope imaging using two-photon excitation of the second singlet state of fluorescent agents* in *Optical Biopsy XII* **8940** (2014), 176–182. https://www.spiedigitallibrary.org/conference-proceedings-of-spie/8940/894017/Enhancing-the-depth-of-tissue-microscope-imaging-using-two-photon/10.1117/12.2035334.full.

58. *Is indocyanine green (ICG) FDA approved?* Accessed 25 August 2023. https://www.aatbio.com/resources/faq-frequently-asked-questions/Is-indocyanine-green-ICG-FDA-approved.

59. Szoke, S., He, M., Hickam, B. P. & Cushing, S. K. Designing High-Power, oOctave Spanning Entangled Photon Sources for Quantum Spectroscopy. *The Journal of Chemical Physics* **154,** 244201. https://aip.scitation.org/doi/10.1063/5.0053688 (2021).

60. Harper, N. A. *et al.* Highly efficient visible and near-IR photon pair generation with thin-film lithium niobate. *arXiv:2310.07046.* http://arxiv.org/abs/2310.07046 (2023).

61. Berezin, M. Y., Lee, H., Akers, W. & Achilefu, S. Near Infrared Dyes as Lifetime Solvatochromic Probes for Micropolarity Measurements of Biological Systems. *Biophysical Journal* **93,** 2892–2899. https://www.cell.com/biophysj/abstract/S0006-3495(07)71542-4 (2007).

62. Makarov, N. S., Drobizhev, M. & Rebane, A. Two-photon absorption standards in the 550–1600 nm excitation wavelength range. *Optics Express* **16,** 4029–4047. https://www.osapublishing.org/oe/abstract.cfm?uri=oe-16-6-4029 (2008).

63. Deng, X. *et al.* Measurement of two-photon properties of indocyanine green in water and human plasma excited at the 1700-nm window. *Journal of Biophotonics* **13,** e202000299. https://onlinelibrary.wiley.com/doi/abs/10.1002/jbio.202000299 (2020).

64. *IsoPlane* Accessed 20 December 2023. https://www.princetoninstruments.com/products/isoplane-family/isoplane.

65. *PI MAX 4* Accessed 20 December 2023.

66. Lavoie, J. *et al.* Phase-Modulated Interferometry, Spectroscopy, and Refractometry using Entangled Photon Pairs. *Advanced Quantum Technologies* **3,** 1900114. http://onlinelibrary.wiley.com/doi/abs/10.1002/qute.201900114 (2020).

67. Skoog, D. A., Holler, F. J. & Crouch, S. R. *Principles of Instrumental Analysis* 7th ed. ISBN: 978-1-305-57721-3. https://www.cengage.com/c/principles-of-instrumental-analysis-7e-skoog-holler-crouch/9781305577213/ ().

68. Miles, R. B., Lempert, W. R. & Forkey, J. N. Laser Rayleigh scattering. *Measurement Science and Technology* **12,** R33. https://dx.doi.org/10.1088/0957-0233/12/5/201 (2001).

69. Oulianov, D. A., Tomov, I. V., Dvornikov, A. S. & Rentzepis, P. M. Observations on the measurement of two-photon absorption cross-section. *Optics Communications* **191,** 235–243. https://www.sciencedirect.com/science/article/pii/S003040180101121X (2001).

70. Kubin, R. F. & Fletcher, A. N. Fluorescence quantum yields of some rhodamine dyes. *Journal of Luminescence* **27,** 455–462. https://www.sciencedirect.com/science/article/pii/002223138290045X (1982).

71. Magde, D., Wong, R. & Seybold, P. G. Fluorescence Quantum Yields and Their Relation to Lifetimes of Rhodamine 6G and Fluorescein in Nine Solvents: Improved Absolute Standards for Quantum Yields. *Photochemistry and Photobiology* **75,** 327–334. https://onlinelibrary.wiley.com/doi/abs/10.1562/0031-8655%282002%290750327FQYATR2.0.CO2 (2002).

72. Itoh, T. Fluorescence and Phosphorescence from Higher Excited States of Organic Molecules. *Chemical Reviews* **112,** 4541–4568. https://doi.org/10.1021/cr200166m (2012).

73. Spasibko, K. Y. *et al.* Multiphoton Effects Enhanced due to Ultrafast Photon-Number Fluctuations. *Physical Review Letters* **119,** 223603. https://link.aps.org/doi/10.1103/PhysRevLett.119.223603 (2017).

74. Cutipa, P., Cutipa, P., Chekhova, M. V. & Chekhova, M. V. Bright squeezed vacuum for two-photon spectroscopy: simultaneously high resolution in time and frequency, space and wavevector. *Optics Letters* **47,** 465–468. https://opg.optica.org/ol/abstract.cfm?uri=ol-47-3-465 (2022).

Chapter 6

ENTANGLED PHOTON CORRELATIONS ALLOW A CONTINUOUS-WAVE LASER DIODE TO MEASURE SINGLE PHOTON, TIME-RESOLVED FLUORESCENCE

ABSTRACT

Fluorescence lifetime experiments are a standard approach for measuring excited state dynamics and local environment effects. Here, we show that entangled photon pairs produced from a continuous-wave (CW) laser diode can replicate pulsed laser experiments without phase modulation. As a proof of principle, picosecond fluorescence lifetimes of indocyanine green are measured in multiple environments. The use of entangled photons has three unique advantages. First, low power CW laser diodes and entangled photon source design lead to straightforward on-chip integration for a direct path to distributable fluorescence lifetime measurements. Second, the entangled pair wavelength is easily tuned by adjusting the temperature or electric field, allowing a single source to cover octave bandwidths. Third, femtosecond temporal resolutions can be reached without requiring major advances in source technology or external phase modulation. Entangled photons could therefore provide increased accessibility to time-resolved fluorescence while also opening new scientific avenues in photosensitive and inherently quantum systems.

Most of this chapter has been reproduced with permission from:

Harper, N. *et al.* Entangled Photon Correlations Allow a Continuous-Wave Laser Diode to Measure Single-Photon, Time-Resolved Fluorescence. *The Journal of Physical Chemistry Letters,* 5805–5811. https://doi.org/10.1021/acs.jpclett.3c01266 (2023).

6.1 Introduction

Time-resolved fluorescence spectroscopy is routinely used in laboratory and clinical settings to measure excited state dynamics and, just as importantly, how changes to the lifetime provide information about the local environment surrounding the fluorophore [1, 2]. The advent of inexpensive pulsed laser diodes has led to a proliferation of time-domain fluorescence lifetime techniques in biosensing and microscopy beyond initial physical chemistry applications. Measured lifetimes are intrinsically fluorophore-specific and depend on variations in the surrounding chemical environment, such as temperature [3], pH [4], neighboring fluorophores [5], and the quantum state [6–9]. This specificity, alongside developments in highly fluorescent tagging proteins and molecular markers, has also enabled fluorescence lifetime imaging microscopy (FLIM) to become a ubiquitous technique to visualize and understand complex biological samples[10, 11]. Autofluorescence endogenous to cellular environments has permitted label-free FLIM medical imaging applications, including clinical cancer diagnosis[12–14].

The next logical frontier for time-resolved fluorescence is highly distributable, wearable devices [15, 16]. At these spatial scales and cost targets, the same pulsed lasers that enabled proliferation of laboratory measurements become a barrier. While on-chip pulsed lasers are being developed, most still require an external power source for the diode or pulse generation [17]. Further, the short on-chip cavity lengths lead to GHz repetition rates that do not give sufficient time for fluorophores to fully relax between pulses [18]. To date, on-chip pulses are mostly in the picosecond range, although recent publications have shown pulses as short as 350 fs [19]. These integrated pulsed lasers typically have a narrow wavelength tuning range, which can make measurements of multiple fluorescent probes or dynamics from multiple local environments difficult [20].

An intriguing alternative to pulsed lasers is to leverage the inherent quantum correlations between entangled photons in a pair. When one high-energy pump photon splits into a pair of two lower-energy entangled photons through spontaneous parametric down-conversion (SPDC), the two single photons are deterministically correlated in time [21]. Thus, if one photon is used to excite a fluorophore, coincidence detection of the resulting fluorescence with the other entangled photon provides a measurement of the time-resolved fluorescence [22]. The uncertainty in the temporal width of the photon pair wave packet can range from tens [23–25] to hundreds [21] of femtoseconds, enabling time-resolved measurements comparable

to those made with tabletop classical pulsed lasers. It is also key to note that, unlike continuous-wave (CW) phase modulation spectroscopy [26], a high frequency modulator is not needed for this technique due to its utilization of the inherent correlations between two entangled photons.

Given that classical time-resolved fluorescence instruments are also limited by detector bandwidths and timing circuits, CW entangled photon sources provide comparable experiments but with a few interesting technological advantages. First, it is straightforward to fabricate on-chip entangled photon sources that require only microwatts of power from a CW laser diode [27, 28]. Second, the wavelengths of the SPDC photons can be tuned across the transparency range of the down-conversion crystal, usually from UV to near-IR, by varying the phase matching conditions, either by heating the crystal or by tuning the pump wavelength, enabling a range of biosensing and physical chemistry experiments [29]. Finally, femtosecond temporal resolutions can be reached without requiring major advances in external phase modulation or detection technology. Scientifically, given that the entangled photon measurements are natively performed in a single-photon-per-measurement regime, the technique is also interesting for measuring photosensitive samples [30], studying quantum systems [31], or exploring scaling behaviors of various properties against incidence flux [32, 33].

Despite early theoretical interest in utilizing entangled pairs to perform lifetime measurements [22, 34, 35], an experimental demonstration using a CW laser has not yet been published[1]. We therefore provide a proof-of-principle experiment by measuring the fluorescence lifetime of indocyanine green (ICG). The correlation time of the entangled photon source is < 30 fs [25], but the detector used limits temporal resolution to 50 ps and minimum measurable lifetime to 365 ps [36]. The excited-state lifetimes of ICG in three solvents are measured to check the accuracy of the technique against previously published work [37]. Through a statistical analysis we show that, even though limited by the MHz detector maximum count rates and bandwidth, integration times in the minutes range provide sufficient signal for accurate lifetime determination using this configuration. Our results demonstrate that measuring time-resolved fluorescence from entangled photons is possible with properties approaching pulsed lasers, providing the proof of principle for new modalities of compact time-resolved fluorescence spectroscopy and experiments in a single-photon excitation and single-photon detection limit. Periodically poled

[1] At the time of this publication, we became aware of Ted Laurence's unpublished work using a similar method for microscopy.

entangled photon sources routinely approach THz pair generation rates, so commercially available picosecond detectors with GHz count rates can improve these measurements to femtosecond temporal resolution and seconds integration time. Future developments could also perform highly multiplexed measurements using the additional correlated properties of SPDC such as the momentum or angular degree of freedom, as proposed in Ref. [22].

6.2 Experimental overview

The experimental configuration for performing fluorescence lifetime measurements with entangled photon pairs is shown in Fig. 6.1, and a detailed description of all components is provided in the Experimental Details section. Briefly, 2 mW of power from a 402.5 nm CW laser diode pumps a periodically poled, Type-0 SPDC crystal to generate entangled photon pairs spanning 720 nm to 913 nm. Here, the pump laser power is significantly reduced using neutral density filters to avoid saturating the single photon counting detectors. The periodically poled bulk source used here produces free-space pairs, adding down-stream losses due to collimation and fiber coupling. A waveguided equivalent would enable the same studies to be performed on-chip and with μW pump powers.

The energies of the photons in the entangled pair sum to that of the pump laser. For the entangled photon source used, one photon has a wavelength between 720 – 805 nm with a simultaneously produced conjugate photon between 805 – 913 nm. The resulting correlation time from this bandwidth is $\sim$ 30 fs, comparable to the pulse width of state-of-the-art mode locked lasers [38]. The detectors used in this experiment have a larger timing jitter (3.65 ns) than the temporal characteristics of the source and ultimately determine the experimental temporal resolution, as explained later in more detail.

The entangled photon pairs are then deterministically split using a short-pass dichroic filter tuned to 805 nm. The reflected lower energy photon heralds the measurement when it is detected by a single photon counting avalanche detector (SPAD), starting the timer for a time-correlated single photon counting (TCSPC) circuit. The higher energy photon is sent to the sample, where it excites a single molecule that then emits a single fluorescence photon with some delay. The fluorescence photon is collected in an epifluorescence scheme and then detected by another SPAD, which stops the timer on the TCSPC board. The time delay between the heralding and fluorescence photon detections is recorded over multiple measure-

ments to create a histogram of such time differences, from which the fluorescence lifetime can be extracted.

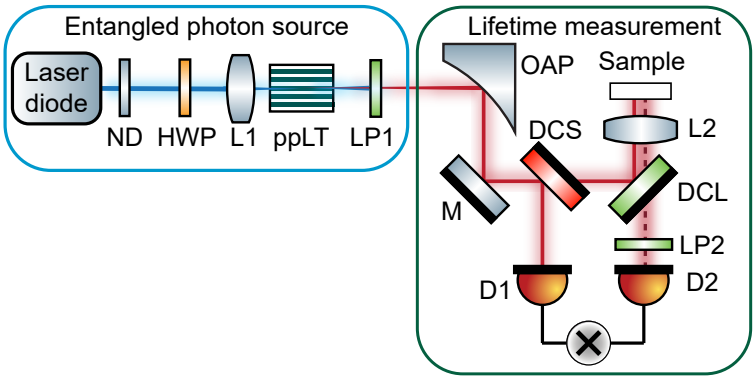

Figure 6.1: Experimental configuration for measuring fluorescence lifetimes with energy-time entangled photon pairs. The broadband entangled photon source consists of a 402.5 nm laser diode that is focused into a periodically poled lithium tantalate crystal. The resulting entangled photons (solid red lines) are collimated with an off-axis parabolic mirror and then separated by wavelength with a dichroic mirror. One photon from the entangled pair is directed to a detector to herald the measurement while the other is focused onto a molecular sample with a high numerical aperture (NA) aspheric lens. The lens collects the backwards emission from the sample's fluorescence (dashed red line) which is then directed through a series of long-pass filters onto a second detector. A coincidence circuit generates histograms of the arrival times between the reference and fluorescence photons. Abbreviations: ND: neutral density filters, HWP: half-wave plate, L1: UVFS focusing lens, ppLT: periodically poled lithium tantalate grating, LP1: 500 nm long-pass filter, OAP: off-axis parabolic mirror, M: mirror, DCS: dichroic short-pass mirror with cut-on wavelength 805 nm, DCL: dichroic short-pass mirror with cut-on wavelength 810 nm, L2: high-NA aspheric lens, LP2: 808 nm long-pass filter, D1 and D2: multimode fiber coupled single photon avalanche photodiodes connected to a coincidence circuit.

The molecular dye indocyanine green (ICG) is used as a proof of principle since it is commonly utilized to perform fluorescence imaging in biological and clinical settings [39, 40]. ICG also has appropriate spectral properties relative to the entangled photon source and a well-characterized lifetime dependence on the solvent environment [37]. Methanol, ethanol, and dimethylsulfoxide (DMSO) were selected as solvents due to their variation of the ICG lifetime by hundreds of picoseconds. The absorption wavelength, emission wavelength, and quantum yield change only slightly across the three solvents (Table D.1). The spectrum of the SPDC was tuned through the phase matching temperature to maximize spectral overlap with

the sample (Fig. 6.2a). The resulting ICG fluorescence (Fig. 6.2b) is separated from the excitation beam with a long-pass dichroic mirror and further filtered with an OD6 long-pass interference filter. The instrument response function (IRF, Fig. 6.2b), which characterizes the response that would be measured by a sample with an infinitely short lifetime, was obtained by replacing the sample with a mirror and removing the final long-pass OD6 filter to allow part of the excitation flux to reach the second detector. The IRF spectrum is altered from the excitation spectrum because it has been filtered by the dichroic mirror, but this alteration has minimal impact on the time-domain response due to the minimal wavelength sensitivity of the SPADs used here.

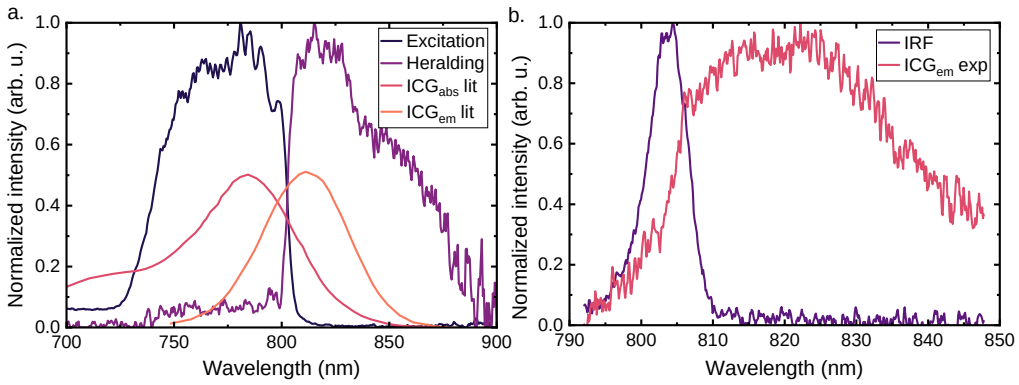

Figure 6.2: Spectral properties of the entangled photons and indocyanine green. (a) Normalized spectra of the entangled photons used for the heralding and excitation photons compared to the normalized absorption/emission spectra for ICG in methanol from Ref. [37]. The ICG spectra have been further scaled by 50% to distinguish them from the entangled photon spectra. (b) Normalized fluorescence signal from 100μM ICG in methanol following entangled photon excitation compared to the portion of entangled photon flux that is used to characterize the instrument response function.

The timing uncertainty broadens the detection of the fluorescence photons by the total IRF. The current temporal resolution of the experiment is limited by the timing uncertainty of the detection electronics, just as with most pulsed laser experiments. The measured histograms $R(t)$ are described by a convolution of the sample's temporal response $S(t)$ with the IRF:

$$R(t) = IRF(t) * S(t) = \int_{-\infty}^{t} IRF(t-t')S(t')dt'. \tag{6.1}$$

After a measurement, the fluorophore lifetime is fit by the sample response function that will give the best match to the measured experimental data. Here, that is a single exponential, but a more complex function could be used if a mixture of lifetimes is present and sufficiently fast detectors are used. Therefore, conceptually, the data produced is analogous to TCSPC with a pulsed laser.

From previous theoretical analysis, the minimum fluorescence lifetime that can be measured before deviation in the fit lifetime occurs is approximately 10% of the IRF width [36]. The IRF width in this experiment is approximately 3.65 ns, limiting our instrument to lifetime measurements greater than 365 ps. The counting circuit used here has a minimum time bin width of 4 ps with a 12 ps electrical time resolution; thus the primary factor in the 3.65 ns IRF width is the SPAD timing jitter. It should be noted that detectors with picosecond timing jitter and GHz count rates are commercially available but were not available to our lab at the time of this experiment. The central moment of the IRF drifts over time, in this case with a 50 ps standard deviation over 20 minutes; therefore, all lifetimes measured using this approach are reported with this level of uncertainty. The relevant characteristic timescales for this experiment are summarized in Table 6.1.

Experiment timescale	SPAD dead time	IRF width[2]	Minimum measurable lifetime[3]	IRF drift (20 minute interval)[4]	Standard error of lifetime fit
Time (ns)	43	3.65	0.365	0.050	0.003

Table 6.1: Summary of relevant experimental timescales from instrument parameters.

6.3 Results: TCSPC histograms and lifetimes

The TCSPC histograms for ICG in three solvents, the IRFs, and the fits of the fluorescence lifetime are shown in Fig. 6.3abc. The measured TCSPC histograms for ICG in different solvents are shifted and broadened due to the nonzero lifetime. This broadening is more pronounced in DMSO compared to methanol and ethanol because of the longer ICG lifetime in this solvent. The ICG excited state lifetimes

[2]This IRF width is mainly due to SPAD jitter.

[3]Based on calculations from Ref. [36] that the minimum measurable lifetime is $\sim$ 10% of the IRF width.

[4]Detector drift results in a small variation of the IRF center value that ultimately limits the temporal resolution of the measurements. The reported fluorescence lifetimes are reported with this value as the standard deviation.

from fitting are presented in Table 6.2 and the exponential decays corresponding to these lifetimes are shown in Fig. 6.3d. The measured lifetimes agree with previously reported values [37] within error. The near-unity χ^2 values and uncorrelated weighted residuals Fig. D.4) indicate a satisfactory fit. The standard deviation of the measurements for all experiments are reported as 50 ps due to detector drift, which is larger than the 3 ps standard errors from the fit. The curves in Fig. 6.3abc are normalized and background subtracted for clarity. The raw experimental data plotted on a logarithmic scale are also available in Fig. D.3. An experiment where the sample is replaced by a blank cuvette of methanol does not yield a measurable coincidence peak Fig. D.1.

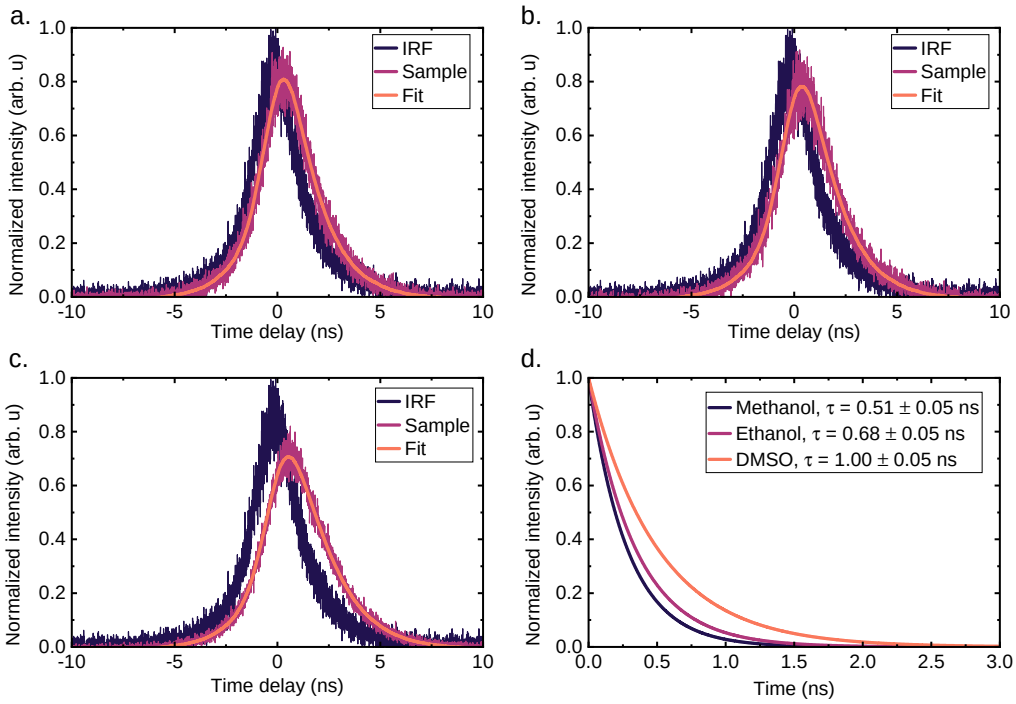

Figure 6.3: Normalized instrument response, TCSPC histogram, and fit of the histogram for ICG in methanol (a), ethanol (b), and DMSO (c). (d) Normalized fluorescence lifetime decays of ICG in each solvent reconstructed from the TCSPC fit lifetime and a single-exponential model.

6.4 Results: Measurement statistics

The practicality of entangled photons for fluorescence lifetime measurements should also be quantified. Due to the Poissonian statistics of photon counting, the signal-

Solvent	Reported lifetime (ns)	Measured lifetime(ns)	χ^2 statistic
Methanol	0.51	0.56 ± 0.05	1.003
Ethanol	0.62	0.68 ± 0.05	0.975
DMSO	0.97	1.00 ± 0.05	1.019

Table 6.2: Fluorescence lifetimes for ICG in solutions of methanol, ethanol, and DMSO previously characterized in Ref. [37], as well as the lifetimes measured in this work and the fitting statistic.

to-noise ratio is expected to scale according to $\sqrt{N}$, where N is the number of true coincident photon events recorded. The number of coincidences can be increased either by increasing the SPDC flux or by increasing the integration time of each histogram. To verify the noise statistics, the fit procedure was repeated on one-minute subsets of a 14 hour DMSO dataset (Fig. 6.4). As expected, the uncertainty in the fitted lifetime in DMSO scales proportionally to $N^{-0.53\pm0.01}$, close to the expected $N^{-1/2}$ (Fig. 6.4). For each sampling interval, the dataset was binned and a fit was performed on each of the resulting histograms. The resulting standard deviation of the inferred lifetimes was recorded. The increasing uncertainty in the standard deviation at long integration times originates from the smaller sample sizes.

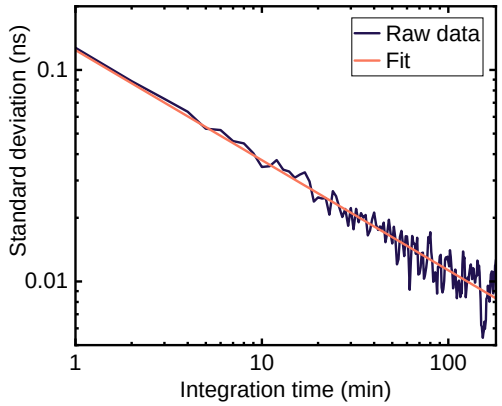

Figure 6.4: Standard deviation of the fit lifetime with respect to integration time for ICG in DMSO.

Fig. 6.4 suggest that integration times on the order of several minutes would be sufficient for lifetime determination with a 10% uncertainty, based on the detectors used here that saturate at 10^6 photons/s fluxes. The integration time could be reduced to $<$ 1 minute by using higher count rate detectors, such as those that can reach 10^9 photon/s, given that the pair rate of the experimental entangled source could

have been increased by over two orders of magnitude. Theoretically, only ~ 200 coincidences are necessary for single exponential decay lifetimes to be determined with 10% uncertainty when the IRF is shorter than the molecular lifetime [41], potentially further lowering the experimental integration time to below 1 second, closer to current microscopic techniques. Using coincidence counting also leads to rejection of background, classical photons on the order of $1,000 : 1$, making the scheme feasible even in sun-lit and room-lit conditions [42].

The proposed technique is therefore aptly timed with the rapidly evolving world of photon counting detector technology [43–45], especially given that THz flux entangled photon sources are already feasible. Fig. 6.4 provides evidence that the use of GHz bandwidth detectors coupled with high efficiency (10^{-6}) entangled photon sources would allow for reasonable integration times even with $\sim \mu$W power CW laser diodes. Thus, the technique presented here has multiple interesting outlooks compared to conventional pulsed laser TCSPC or CW-modulated fluorescence lifetime measurements, whether it is used for on-chip technology advances, investigation of dynamics in the single-photon excitation limit, or exploration of the ability of quantum systems and molecules to preserve incident quantum states of light.

It is important to note, however, that this method is fundamentally limited by the need to time every heralding photon, regardless of whether a fluorescence photon is detected. Practically, this means that the maximum SPDC rate is limited to the inverse of the detector dead time or molecular lifetime, whichever is larger, and the flux that contributes to the measurement will be reduced by the detector inefficiency. As a result, the count rate of fluorescence events will be restricted by the maximum SPDC flux and the probability of converting excitation photons to fluorescence detection events, which is a function of both molecular and instrumental parameters. Currently, entangled photon pair rates in the THz range can be produced, whereas state of the art photon counting detectors and molecular lifetimes imply sub-GHz pair rates are necessary. Regardless of technology advancements, this upper limit could be surpassed by multiplexing on an EMICCD or SPAD array as proposed in Ref. [22], which would allow the full potential of THz-rate entangled sources to be used.

6.5 Conclusion

In conclusion, we have demonstrated that molecular excited state lifetimes can be measured using the temporal correlations of entangled photons produced from a

CW laser. The solvent-dependent lifetime of indocyanine green was measured in methanol, ethanol, and DMSO in agreement with previous reports using pulsed lasers. The low pump flux needed for SPDC provides a direct route to time-resolved fluorescence measurements using on-chip, CMOS compatible photonics. Multiple waveguides and temperature tuning of phase matching can be used in the future to quickly measure a wide range of fluorophores from a single SPDC source and a photonic circuit. Overall, using a CW laser diode as a pump source opens new horizons for performing complex spectroscopic and microscopic studies with quantum light sources.

6.6 Experimental details

Broadband entangled pairs are generated in a periodically poled crystal whose design and characterization, as well as its use in studying entangled light-matter interactions, has been reported previously [25, 46]. In short, photon pairs are generated by Type-0 spontaneous parametric down-conversion in a third-order periodically poled 8% MgO-doped congruent lithium tantalate (CLT) bulk crystal (HC Photonics). The crystal is pumped with a continuous wave diode laser with a maximum power of 400 mW at 402.5 nm and FWHM linewidth of 1 nm (Coherent OBIS). The pump polarization is conditioned with a polarizing beamsplitter (Thorlabs PBSW-405) and half-wave plate (Thorlabs WPH10M-405) before being focused through the SPDC crystal with a 40 cm focal length UV-fused silica lens (Eksma Optics). The temperature of the crystal and subsequent entangled photon bandwidth and spectrum is set and maintained using a chip heater and PID loop with an accuracy of 10mK (Covesion). For measurements of indocyanine green (ICG, Sigma Aldrich) the crystal was heated to 75.0℃ to tune the SPDC to a nondegenerate spectrum where the low-wavelength photons overlap with the ICG absorption curve. A series of 500nm OD 4 long-pass (Edmund Optics #84-706) and spatial filters (irises) remove any remaining pump photons and select the entangled photon pairs that are collinear with the pump beam.

Following the filters, the entangled photons are collimated with an off-axis parabolic mirror (Thorlabs) and directed to a short-pass dichroic mirror with a nominal cut-on wavelength of 800 nm (Edmund Optics #69-196). The incidence angle of the dichroic mirror is fine-tuned with a rotation mount (Thorlabs RP005) to increase the cut-on wavelength to 805 nm, the degenerate wavelength of the pairs, as measured with a grating spectrometer (Princeton Instruments IsoPlane SCT-320, 150 gr/mm grating with 800 nm blaze) and electron multiplying intensified charge-coupled

device (EMICCD, Princeton Instruments PIMAX4). The reflected flux (805 nm – 913 nm) is fiber-coupled into a multimode fiber (105μm core, 0.22 NA, M43L01) using two mirrors and a 4.51 mm focal length aspheric lens (Thorlabs C230TMD-B) and serves as the herald for the experiment. The transmitted flux is directed to a long-pass dichroic mirror with a nominal cut-on wavelength of 800 nm (Edmund Optics #69-883) and serves as the excitation for the sample. The angle of this dichroic mirror is also fine-tuned with a rotation mount (Thorlabs RP005) such that the transmission is $>$ 810 nm so that the passband does not overlap with that of the first dichroic mirror. A high-NA 4.51 mm focal length aspheric lens (Thorlabs C230TMD-B) focuses the excitation photons into a 1 mm path length quartz cuvette (Helma/Millipore Sigma) containing $\sim$ 300μL of 100μM ICG in solution. The cuvette is mounted onto a micrometer-driven linear stage to precisely control the position of the sample relative to the focus of the excitation beam. The resulting fluorescence is collected through the long-pass dichroic and coupled into a second SPAD using with two mirrors, a 9.2 mm diameter, 4.51 mm focal length aspheric lens (Thorlabs C230TMD-B), and a multimode fiber (105μm core, 0.22 NA, M43L01). An OD6 808 nm long-pass filter (Semrock LP02-808RE-25) following the dichroic mirror filters any remaining SPDC photons and/or scatter from the fluorescence signal. For the IRF measurements, the sample cuvette was replaced with a mirror, which was positioned so the excitation beam was focused at the surface of the mirror. Differences in pathlength due to the missing glass of the cuvette are estimated to introduce a 5 ps error, which is below the resolution of this experiment. Black cardboard boxes are positioned to block the sample from any pump scatter and minimize background.

Spectral measurements of the heralding and fluorescence photons were performed by collimating the output of the fibers and directing the image onto the spectrometer/EMICCD. The spectrum of the excitation photons was measured similarly by replacing the sample with a multimode fiber with a micrometer-driven x/y translation mount. This same scheme was used with coincidence counting to estimate the number of heralded excitation photons arriving at the sample.

Lifetime measurements were performed by connecting the multimode fibers to SPADs (Laser Components Count) and a coincidence counting circuit (PicoQuant PicoHarp 300). For these experiments, the SPDC between 805 and 912 nm served as the heralding trigger, and the SPAD output was connected to the sync channel of the counting circuit in a forward start-stop mode. The detection events of the

fluorescence SPAD served as the stop signal for the experiment, and the SPAD output was connected to the CH1 input of the counting circuit. An electronic delay of 30 ns between the arms was implemented through the counting circuit. This offset is subtracted from the time axis of Fig. 6.3(abc) for clarity but is not removed from the raw data in the supplementary information. Neutral density filters were used to decrease pump power and resulting SPDC flux to minimize lost heralding events due to the dead-time of the detectors (43 ns). For lifetime measurements, the number of singles in the heralding arm was approximately $1 * 10^5$ counts/s, and the number of singles in the fluorescence arm was approximately 600 counts/s. Data collection consists of repeatedly collecting histograms for 60 seconds, with a series of 10 measurements of the singles rates in each channel measured between each histogram to monitor drift in the alignment. For the methanol, ethanol, and DMSO scans, 840, 840, and 960 histograms were collected, resulting in a total experiment time of 14, 14, and 16 hours, respectively. The instrument response function was measured over 240 coincidence histograms for a total of 6 hours. A custom MATLAB fitting routine is used to determine the characteristic excited state lifetime using the iterative reconvolution approach [47]. In this technique, the single-exponential sample response function is varied so that its convolution with the IRF best matches the measured histograms by minimizing the sum of squared errors.

References

1. Cundall, R. *Time-Resolved Fluorescence Spectroscopy in Biochemistry and Biology* ISBN: 978-1-4757-1634-4 (Springer Science & Business Media, 2013).

2. Bright, F. V. & Munson, C. A. Time-resolved fluorescence spectroscopy for illuminating complex systems. *Analytica Chimica Acta. ANALYTICAL HORIZONS - An International Symposium celebrating the publication of Volume 500 of Analytica Chimica Acta* **500,** 71–104. https://www.sciencedirect.com/science/article/pii/S0003267003007232 (2003).

3. Sumitani, M., Nakashima, N., Yoshihara, K. & Nagakura, S. Temperature dependence of fluorescence lifetimes of trans-stilbene. *Chemical Physics Letters* **51,** 183–185. https://www.sciencedirect.com/science/article/pii/0009261477853815 (1977).

4. Islam, M. S., Honma, M., Nakabayashi, T., Kinjo, M. & Ohta, N. pH Dependence of the Fluorescence Lifetime of FAD in Solution and in Cells. *International Journal of Molecular Sciences* **14,** 1952–1963. https://www.mdpi.com/1422-0067/14/1/1952 (2013).

5. Sekar, R. B. & Periasamy, A. Fluorescence resonance energy transfer (FRET) microscopy imaging of live cell protein localizations. *The Journal of Cell Biology* **160,** 629–633. https://www.ncbi.nlm.nih.gov/pmc/articles/PMC2173363/ (2003).

6. Frimmer, M., Chen, Y. & Koenderink, A. F. Scanning Emitter Lifetime Imaging Microscopy for Spontaneous Emission Control. *Physical Review Letters* **107,** 123602. https://link.aps.org/doi/10.1103/PhysRevLett.107.123602 (2011).

7. Schell, A. W. *et al.* Scanning Single Quantum Emitter Fluorescence Lifetime Imaging: Quantitative Analysis of the Local Density of Photonic States. *Nano Letters* **14,** 2623–2627. https://doi.org/10.1021/nl500460c (2014).

8. Inam, F. A. *et al.* Emission and Nonradiative Decay of Nanodiamond NV Centers in a Low Refractive Index Environment. *ACS Nano* **7,** 3833–3843. https://doi.org/10.1021/nn304202g (2013).

9. Dunn, T. J., Walmsley, I. A. & Mukamel, S. Experimental Determination of the Quantum-Mechanical State of a Molecular Vibrational Mode Using Fluorescence Tomography. *Physical Review Letters* **74,** 884–887. https://link.aps.org/doi/10.1103/PhysRevLett.74.884 (1995).

10. Datta, R., Heaster, T. M., Sharick, J. T., Gillette, A. A. & Skala, M. C. Fluorescence lifetime imaging microscopy: fundamentals and advances in instrumentation, analysis, and applications. *Journal of Biomedical Optics* **25,** 071203. https://www.spiedigitallibrary.org/journals/journal-of-biomedical-optics/volume-25/issue-7/071203/Fluorescence-lifetime-imaging-microscopy--fundamentals-and-advances-in-instrumentation/10.1117/1.JBO.25.7.071203.full (2020).

11. Becker, W. Fluorescence lifetime imaging – techniques and applications. *Journal of Microscopy* **247,** 119–136. https://onlinelibrary.wiley.com/doi/abs/10.1111/j.1365-2818.2012.03618.x (2012).

12. Wang, Z. *et al.* Applications of fluorescence lifetime imaging in clinical medicine. *Journal of Innovative Optical Health Sciences* **11,** 1830001. https://www.worldscientific.com/doi/10.1142/S179354581830001X (2018).

13. Blondel, W. *et al.* Spatially-Resolved Multiply-Excited Autofluorescence and Diffuse Reflectance Spectroscopy: SpectroLive Medical Device for Skin In Vivo Optical Biopsy. *Electronics* **10,** 243. https://www.mdpi.com/2079-9292/10/3/243 (2021).

14. Ouyang, Y., Liu, Y., Wang, Z. M., Liu, Z. & Wu, M. FLIM as a Promising Tool for Cancer Diagnosis and Treatment Monitoring. *Nano-Micro Letters* **13,** 133. https://doi.org/10.1007/s40820-021-00653-z (2021).

15. Elson, D. S., Jo, J. A. & Marcu, L. Miniaturized side-viewing imaging probe for fluorescence lifetime imaging (FLIM): validation with fluorescence dyes, tissue structural proteins and tissue specimens. *New journal of physics* **9,** 127. https://www.ncbi.nlm.nih.gov/pmc/articles/PMC2691608/ (2007).

16. Paterson, A. S. *et al.* A low-cost smartphone-based platform for highly sensitive point-of-care testing with persistent luminescent phosphors. *Lab on a Chip* **17,** 1051–1059. https://pubs.rsc.org/en/content/articlelanding/2017/lc/c6lc01167e (2017).

17. Davenport, M. L., Liu, S. & Bowers, J. E. Integrated heterogeneous silicon/III–V mode-locked lasers. *Photonics Research* **6,** 468–478. https://opg.optica.org/prj/abstract.cfm?uri=prj-6-5-468 (2018).

18. Turgeman, L. & Fixler, D. Photon Efficiency Optimization in Time-Correlated Single Photon Counting Technique for Fluorescence Lifetime Imaging Systems. *IEEE Transactions on Biomedical Engineering* **60,** 1571–1579 (2013).

19. Lu, Z. G. *et al.* 312-fs pulse generation from a passive C-band InAs/InP quantum dot mode-locked laser. *Optics Express* **16,** 10835–10840. https://opg.optica.org/oe/abstract.cfm?uri=oe-16-14-10835 (2008).

20. Valeur, B. & Berberan-Santos, M. B. in *Molecular Fluorescence* 285–325 (John Wiley & Sons, 2012). ISBN: 978-3-527-65000-2. https://onlinelibrary.wiley.com/doi/abs/10.1002/9783527650002.ch10.

21. MacLean, J.-P. W., Donohue, J. M. & Resch, K. J. Direct Characterization of Ultrafast Energy-Time Entangled Photon Pairs. *Physical Review Letters* **120,** 053601. https://link.aps.org/doi/10.1103/PhysRevLett.120.053601 (2018).

22. Scarcelli, G. & Yun, S. H. Entangled-photon coincidence fluorescence imaging. *Optics Express* **16,** 16189–16194. https://opg.optica.org/oe/abstract.cfm?uri=oe-16-20-16189 (2008).

23. Nasr, M. B. *et al.* Ultrabroadband Biphotons Generated via Chirped Quasi-Phase-Matched Optical Parametric Down-Conversion. *Physical Review Letters* **100,** 183601. https://link.aps.org/doi/10.1103/PhysRevLett.100.183601 (2008).

24. Hendrych, M., Shi, X., Valencia, A. & Torres, J. P. Broadening the bandwidth of entangled photons: A step towards the generation of extremely short biphotons. *Physical Review A* **79,** 023817. https://link.aps.org/doi/10.1103/PhysRevA.79.023817 (2009).

25. Szoke, S., He, M., Hickam, B. P. & Cushing, S. K. Designing High-Power, oOctave Spanning Entangled Photon Sources for Quantum Spectroscopy. *The Journal of Chemical Physics* **154,** 244201. https://aip.scitation.org/doi/10.1063/5.0053688 (2021).

26. Menzel, E. R. & Popovic, Z. D. Picosecond-resolution fluorescence lifetime measuring system with a cw laser and a radio. *Review of Scientific Instruments* **49,** 39–44. https://doi.org/10.1063/1.1135248 (2008).

27. Zhao, J., Ma, C., Rüsing, M. & Mookherjea, S. High Quality Entangled Photon Pair Generation in Periodically Poled Thin-Film Lithium Niobate Waveguides. *Phys. Rev. Lett.* **124,** 163603. https://link.aps.org/doi/10.1103/PhysRevLett.124.163603 (2020).

28. Javid, U. A. *et al.* Ultrabroadband Entangled Photons on a Nanophotonic Chip. *Physical Review Letters* **127,** 183601. https://link.aps.org/doi/10.1103/PhysRevLett.127.183601 (2021).

29. Kumar, R., Ong, J. R., Savanier, M. & Mookherjea, S. Controlling the spectrum of photons generated on a silicon nanophotonic chip. *Nature Communications* **5,** 5489. https://www.nature.com/articles/ncomms6489 (2014).

30. Brumer, P. & Shapiro, M. Molecular response in one-photon absorption via natural thermal light vs. pulsed laser excitation. *Proceedings of the National Academy of Sciences* **109,** 19575–19578. https://www.pnas.org/doi/10.1073/pnas.1211209109 (2012).

31. Zavatta, A., Viciani, S. & Bellini, M. Single-photon excitation of a coherent state: Catching the elementary step of stimulated light emission. *Physical Review A* **72,** 023820. https://link.aps.org/doi/10.1103/PhysRevA.72.023820 (2005).

32. Freitag, M. *et al.* Dye-sensitized solar cells for efficient power generation under ambient lighting. *Nature Photonics* **11,** 372–378. https://www.nature.com/articles/nphoton.2017.60 (2017).

33. Reich, N. H., van Sark, W. G. J. H. M. & Turkenburg, W. C. Charge yield potential of indoor-operated solar cells incorporated into Product Integrated Photovoltaic (PIPV). *Renewable Energy* **36,** 642–647. https://www.sciencedirect.com/science/article/pii/S0960148110003423 (2011).

34. Asban, S., Dorfman, K. E. & Mukamel, S. Interferometric spectroscopy with quantum light: Revealing out-of-time-ordering correlators. *The Journal of Chemical Physics* **154,** 210901. https://doi.org/10.1063/5.0047776 (2021).

35. Oka, H. Real-time analysis of two-photon excitation by correlated photons: Pulse-width dependence of excitation efficiency. *Physical Review A* **81,** 053837. https://link.aps.org/doi/10.1103/PhysRevA.81.053837 (2010).

36. Becker, W. *Advanced Time-Correlated Single Photon Counting Techniques* (eds Castleman, A. W., Toennies, J. & Zinth, W.) ISBN: 978-3-540-26047-9 978-3-540-28882-4. http://link.springer.com/10.1007/3-540-28882-1 (Springer, Berlin, Heidelberg, 2005).

37. Berezin, M. Y., Lee, H., Akers, W. & Achilefu, S. Near Infrared Dyes as Lifetime Solvatochromic Probes for Micropolarity Measurements of Biological Systems. *Biophysical Journal* **93,** 2892–2899. https://www.cell.com/biophysj/abstract/S0006-3495(07)71542-4 (2007).

38. Dorfman, K. E., Schlawin, F. & Mukamel, S. Nonlinear optical signals and spectroscopy with quantum light. *Reviews of Modern Physics* **88,** 045008. https://link.aps.org/doi/10.1103/RevModPhys.88.045008 (2016).

39. Alander, J. T. *et al.* A review of indocyanine green fluorescent imaging in surgery. *Journal of Biomedical Imaging* **2012,** 7:7. https://dl.acm.org/doi/10.1155/2012/940585 (2012).

40. Reinhart, M. B., Huntington, C. R., Blair, L. J., Heniford, B. T. & Augenstein, V. A. Indocyanine Green: Historical Context, Current Applications, and Future Considerations. *Surgical Innovation* **23,** 166–175. https://doi.org/10.1177/1553350615604053 (2016).

41. Köllner, M. & Wolfrum, J. How many photons are necessary for fluorescence-lifetime measurements? *Chemical Physics Letters* **200,** 199–204. https://www.sciencedirect.com/science/article/pii/000926149287068Z (1992).

42. Beer, M., Haase, J. F., Ruskowski, J. & Kokozinski, R. Background Light Rejection in SPAD-Based LiDAR Sensors by Adaptive Photon Coincidence Detection. *Sensors* **18,** 4338. https://www.mdpi.com/1424-8220/18/12/4338 (2018).

43. Shen, B., Bose, S. & Johnston, M. L. On-chip high-voltage SPAD bias generation using a dual-mode, closed-loop charge pump. *2017 IEEE International Symposium on Circuits and Systems (ISCAS),* 1–4 (2017).

44. Tisa, S., Zappa, F. & Labanca, I. On-chip detection and counting of single-photons. *IEEE InternationalElectron Devices Meeting, 2005. IEDM Technical Digest.,* 815–818 (2005).

45. Maruyama, Y. & Charbon, E. An all-digital, time-gated 128X128 spad array for on-chip, filter-less fluorescence detection. *2011 16th International Solid-State Sensors, Actuators and Microsystems Conference,* 1180–1183 (2011).

46. Hickam, B. P., He, M., Harper, N., Szoke, S. & Cushing, S. K. Single-Photon Scattering Can Account for the Discrepancies among Entangled Two-Photon Measurement Techniques. *The Journal of Physical Chemistry Letters,* 4934–4940. https://pubs.acs.org/doi/10.1021/acs.jpclett.2c00865 (2022).

47. Grinvald, A. & Steinberg, I. Z. On the analysis of fluorescence decay kinetics by the method of least-squares. *Analytical Biochemistry* **59,** 583–598 (1974).

Chapter 7

CONCLUSION AND OUTLOOK

Studies of entangled light-matter interactions have been gaining momentum because of their potential applications in bioimaging and sensing. Entangled photons are predicted to linearize nonlinear optical processes and offer orders of magnitude of enhancement to the interaction cross sections. To investigate the validity of entanglement-enhanced bioimaging techniques, I have designed and characterized the performance of an on-chip broadband entangled light source based on periodically poled lithium tantalate (ppLT). This light source achieved ultrafast entangled correlation times with an unprecedented power of ~ 100 nW in near-infrared (NIR), which is a crucial first step toward fully integrated, thin-film lithium niobate (TFLN)-based, visible to NIR entangled photon sources [1, 2]. I have used this light source to carry out subsequent spectroscopy/microscopy experiments to systematically investigate the feasibility of entanglement-enabled microscopy techniques such as entangled two-photon absorption (ETPA) microscopy and entangled fluorescence lifetime measurements. I developed and characterized a novel method to measure fluorescence from ETPA using a spectrotemporally resolved Michelson interferometer which is good at eliminating false signals due to one-photon absorption and scattering. By attempting to detect virtual-state mediated ETPA from rhodamine 6G (R6G) and resonance-enhanced ETPA from indocyanine green (ICG), I concluded that the ETPA signals were below the detection limits of the instruments and often masked by one-photon effects such as scattering and linear absorption, and that resonance enhancement provided experimentally negligible improvement on the ETPA cross section. Instead, experimental upper bounds were placed on the ETPA cross sections of the studied molecules, and continued improvement of the light source and instrument detection limits was emphasized. Although ETPA may not be a viable process for harnessing quantum enhancements, other nonlinear processes such as second-harmonic generation (SHG) imaging [3, 4] and stimulated Raman scattering (SRS) microscopy may still benefit significantly from entanglement enhancement. SHG experiences higher quantum enhancement than two-photon absorption (TPA) as it relies on polarizability instead of an excited state. Although quantum-enhanced SHG has already been demonstrated with squeezed light [5, 6], future studies focusing on lower-flux, entangled SHG and its application in microscopy are still needed.

Similarly, stimulated Raman processes have inherently higher "effective" cross sections than TPA, on the order of 10^{-32} to 10^{-22} cm^2 for single chemical bonds (i.e., C-H, C=O, etc.)[7]. SRS has been predicted to be susceptible to quantum enhancement from frequency-correlated entangled photons [8], which cannot be produced by narrow-linewidth continuous wave (CW) lasers, but can be produced via dispersion engineering and special phase-matching conditions using pulsed lasers [9–12].

I have also identified on-chip entangled fluorescence lifetime imaging microscopy (entangled-FLIM) as a major future development focus that will enable scalable, on-chip, nonlinear bioimaging and sensing applications. I demonstrated its feasibility via a proof-of-principle experiment which measured the fluorescence lifetime of ICG in various solvents. Using entangled photons produced from a CW laser, the lifetime measurement scheme achieved a temporal resolution of 50 ps and a minimum measurable lifetime of 365 ps, which can be used to distinguish most biologically relevant fluorophores in the wavelength range of the light source [13]. This experiment is a critical first step toward scalable, high-throughput, wavelength-multiplexed, and on-chip FLIM or lifetime measurements which could be used in label-free health monitoring technologies. Future development of this technique should focus on three parallel directions: 1) Creating fully integrated photonics platforms that include an integrated pump light source, entanglement generation, spectrotemporal control of the entangled state, and sample interaction windows. The material should ideally be CMOS-compatible, which requires extensive materials research and development beyond TFLN. 2) Lowering the entangled photon wavelengths to the ultraviolet (UV) to visible range in which most autofluorescent biomolecules are excitable [14]. This will allow for label-free lifetime measurements that can identify the species and map out the excited state dynamics of endogenous biomarkers in disease screening. 3) Increasing detector throughput by developing single-photon detectors with GHz to THz count rates in the UV-visible range [15–17] and by adopting multiplexed coincidence counting methods using emICCDs or SPAD arrays [18–20]. Ultimately, CMOS-based single photon counters [21–23] should be used to allow full integration of the entangled-FLIM technique.

References

1. Harper, N. A. *et al.* Highly efficient visible and near-IR photon pair generation with thin-film lithium niobate. *arXiv:2310.07046.* `http://arxiv.org/abs/2310.07046` (2023).

2. Hwang, E. *et al.* Tunable and efficient ultraviolet generation with periodically poled lithium niobate. *Optics Letters* **48,** 3917–3920. https://opg.optica.org/ol/abstract.cfm?uri=ol-48-15-3917 (2023).

3. Wang, J. *et al.* Direct Comparison of Second Harmonic Generation and Two-Photon Photoluminescence from Single Connected Gold Nanodimers. *The Journal of Physical Chemistry C* **120,** 17699–17710. https://doi.org/10.1021/acs.jpcc.6b04850 (2016).

4. Helmchen, F. & Denk, W. Deep tissue two-photon microscopy. *Nature Methods* **2,** 932–940. http://www.nature.com/articles/nmeth818 (2005).

5. Spasibko, K. Y. *et al.* Multiphoton Effects Enhanced due to Ultrafast Photon-Number Fluctuations. *Physical Review Letters* **119,** 223603. https://link.aps.org/doi/10.1103/PhysRevLett.119.223603 (2017).

6. Kopylov, D. A. *et al. Multiphoton effects with bright squeezed vacuum* in *Conference on Lasers and Electro-Optics (2020), paper JTh3N.1* (2020), JTh3N.1. https://opg.optica.org/abstract.cfm?uri=CLEO_SI-2020-JTh3N.1.

7. Gao, X., Li, X. & Min, W. Absolute Stimulated Raman Cross Sections of Molecules. *The Journal of Physical Chemistry Letters* **14,** 5701–5708. https://doi.org/10.1021/acs.jpclett.3c01064 (2023).

8. Svidzinsky, A. *et al.* Enhancing stimulated Raman excitation and two-photon absorption using entangled states of light. *Physical Review Research* **3,** 043029. https://link.aps.org/doi/10.1103/PhysRevResearch.3.043029 (2021).

9. Erdmann, R., Branning, D., Grice, W. & Walmsley, I. A. Restoring dispersion cancellation for entangled photons produced by ultrashort pulses. *Physical Review A* **62,** 053810. https://link.aps.org/doi/10.1103/PhysRevA.62.053810 (2000).

10. Giovannetti, V., Maccone, L., Shapiro, J. H. & Wong, F. N. C. Generating Entangled Two-Photon States with Coincident Frequencies. *Physical Review Letters* **88,** 183602. https://link.aps.org/doi/10.1103/PhysRevLett.88.183602 (2002).

11. Torres, J. P., Macia, F., Carrasco, S. & Torner, L. Engineering the frequency correlations of entangled two-photon states by achromatic phase matching. *Optics Letters* **30,** 314–316. https://opg.optica.org/ol/abstract.cfm?uri=ol-30-3-314 (2005).

12. Hendrych, M., Micuda, M. & Torres, J. P. Tunable control of the frequency correlations of entangled photons. *Optics Letters* **32.** https://opg.optica.org/ol/abstract.cfm?uri=ol-32-16-2339 (2007).

13. Berezin, M. Y. & Achilefu, S. Fluorescence Lifetime Measurements and Biological Imaging. *Chemical Reviews* **110,** 2641–2684. https://doi.org/10.1021/cr900343z (2010).

14. Croce, A. C. & Bottiroli, G. Autofluorescence spectroscopy and imaging: a tool for biomedical research and diagnosis. *European Journal of Histochemistry* **58.** https://www.ejh.it/index.php/ejh/article/view/2461 (2014).

15. Severini, F. *et al.* SPAD Pixel With Sub-NS Dead-Time for High-Count Rate Applications. *IEEE Journal of Selected Topics in Quantum Electronics* **28,** 1–8. https://ieeexplore.ieee.org/document/9601277 (2022).

16. Jiang, W.-H. *et al.* 1.25 GHz sine wave gating InGaAs/InP single-photon detector with a monolithically integrated readout circuit. *Optics Letters* **42,** 5090–5093. https://opg.optica.org/ol/abstract.cfm?uri=ol-42-24-5090 (2017).

17. Scarcella, C., Boso, G., Ruggeri, A. & Tosi, A. InGaAs/InP Single-Photon Detector Gated at 1.3 GHz With 1.5% Afterpulsing. *IEEE Journal of Selected Topics in Quantum Electronics* **21,** 17–22. https://ieeexplore.ieee.org/abstract/document/6919246?casa_token=Vrga53To-BQAAAAA:RJm5NmQbNzvYedyXyBoaUDBR9qPopJTBMhwt8gf4Cwkzuuuo KCW4ebXxJ4Rv7QcgDQWEoxc (2015).

18. Defienne, H., Zhao, J., Charbon, E. & Faccio, D. Full-field quantum imaging with a single-photon avalanche diode camera. *Physical Review A* **103,** 042608. https://link.aps.org/doi/10.1103/PhysRevA.103.042608 (2021).

19. Reichert, M., Defienne, H. & Fleischer, J. W. Massively Parallel Coincidence Counting of High-Dimensional Entangled States. *Scientific Reports* **8,** 7925. http://www.nature.com/articles/s41598-018-26144-7 (2018).

20. Zhang, Y. *et al.* Multidimensional quantum-enhanced target detection via spectrotemporal-correlation measurements. *Physical Review A* **101,** 053808. https://link.aps.org/doi/10.1103/PhysRevA.101.053808 (2020).

21. Tisa, S., Tosi, A. & Zappa, F. Fully-integrated CMOS single photon counter. *Optics Express* **15,** 2873–2887. https://opg.optica.org/oe/abstract.cfm?uri=oe-15-6-2873 (2007).

22. Fossum, E. R., Ma, J., Masoodian, S., Anzagira, L. & Zizza, R. The Quanta Image Sensor: Every Photon Counts. *Sensors* **16,** 1260. https://www.mdpi.com/1424-8220/16/8/1260 (2016).

23. Field, R. M., Realov, S. & Shepard, K. L. A 100 fps, Time-Correlated Single-Photon-Counting-Based Fluorescence-Lifetime Imager in 130 nm CMOS. *IEEE Journal of Solid-State Circuits* **49,** 867–880. https://ieeexplore.ieee.org/abstract/document/6698400?casa_token=JbVwbPPBe

4EAAAAA:TgcGJZgo6-v5pSMPvvcqMtAuw_YP1XqROPOT2a47n8HAXunzpG9j9Rj4DLp-0fQZXfd-f1U (2014).

Appendix A

SUPPLEMENTARY INFORMATION FOR DESIGNING HIGH-POWER, OCTAVE SPANNING ENTANGLED PHOTON SOURCES FOR QUANTUM SPECTROSCOPY

A.1 CLT refractive indices

The Sellmeier equations [1] describing the frequency and temperature dependent refractive indices of the material are plotted in Fig. A.1.

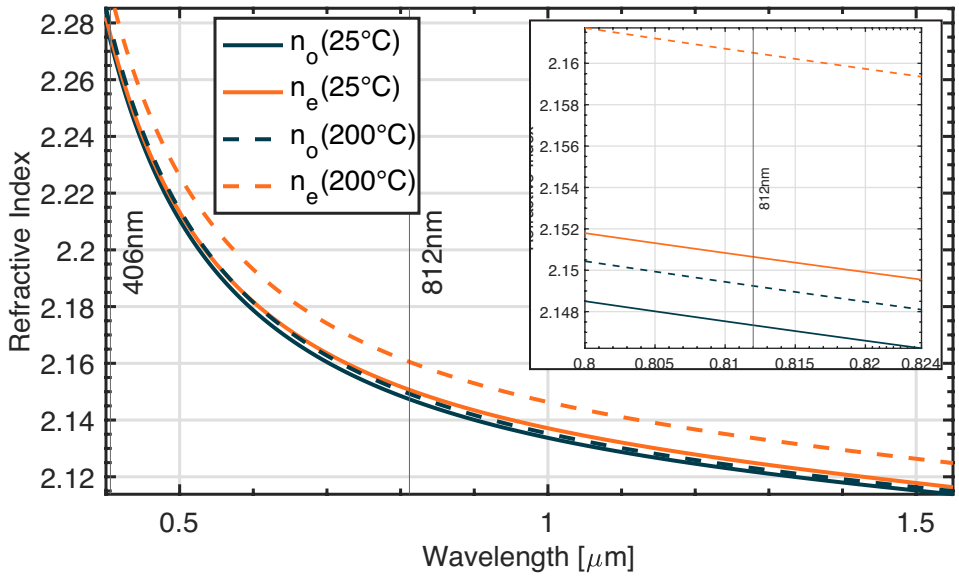

Figure A.1: Congruent lithium tantalate refractive indices for ordinary and extraordinary polarizations at two different temperatures.

A.2 Quasi-phase-matching

Based upon these values, the poling periodicity was calculated for a collinear 3^{rd}-order Type-0 QPM configuration with a degenerate wavelength of 812nm.

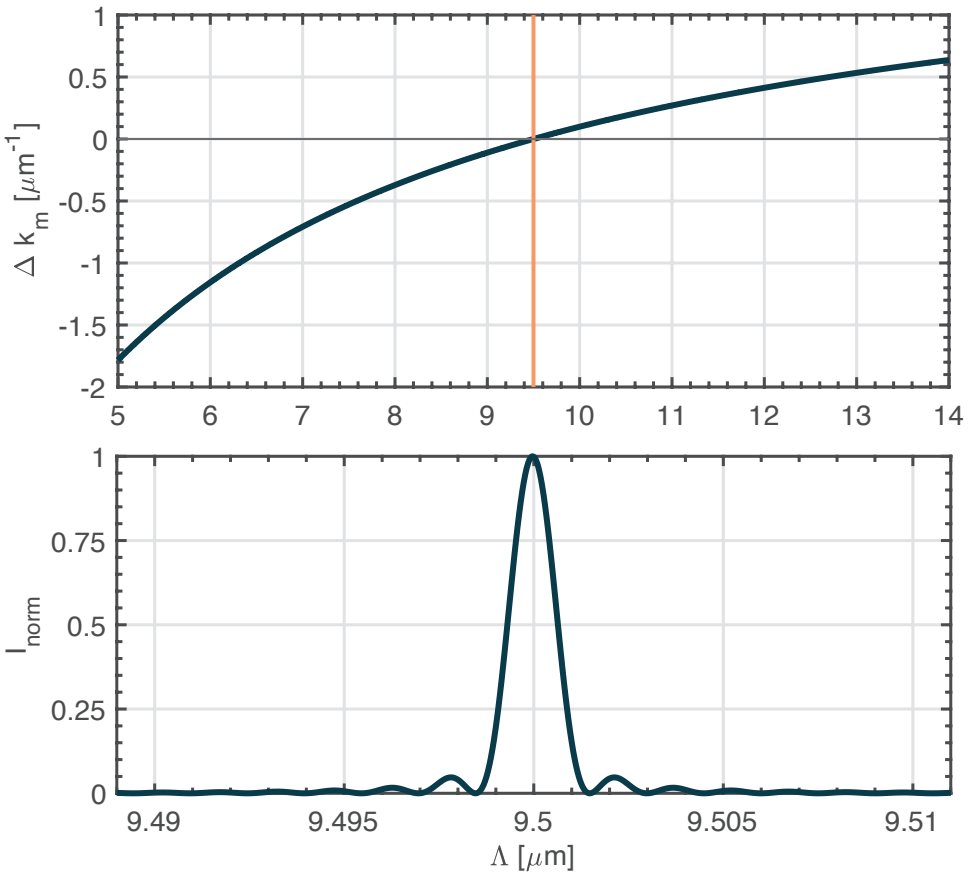

Figure A.2: Calculated poling period for 406nm-812nm at 133℃ — CLT.

A.3 Phase-matching amplitude

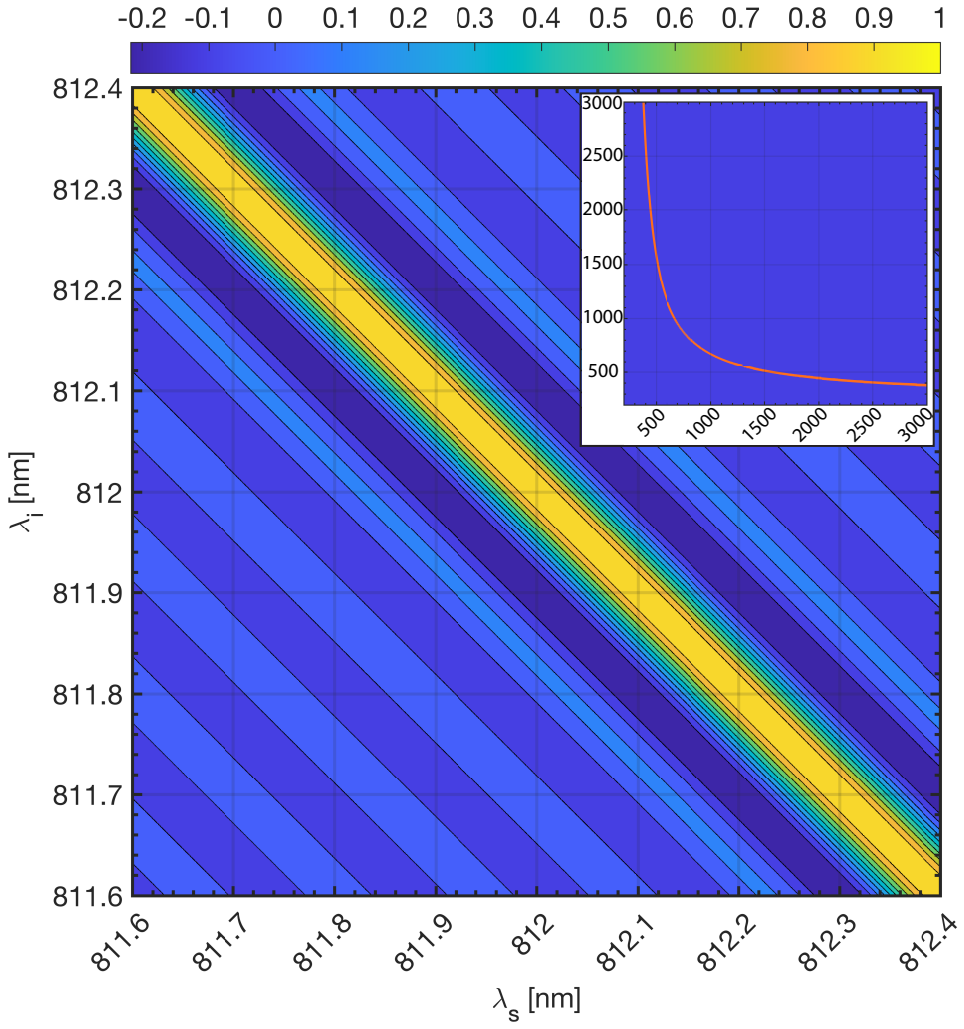

Figure A.3: Phase matching amplitude contour plot for a 20 mm long ppCLT grating with a 9.5 μm poling period at 133℃. The inset shows the wide range phase matching curve across a larger wavelength range for the Type-0 phase matching configuration.

Once the required poling period for our specific crystal and configuration has been determined, the two-dimensional phase-matching amplitude can be calculated by again evaluating Eq. 3.5 and Eq. 3.7 in the main text for a wide range of wavelength combinations. The result is the contour plot in Fig. A.3, which shows the downconversion intensity for photon pairs near the 812 nm degeneracy point. The inset of Fig. A.3 is a wide-range plot displaying the characteristic shape of the phase-matching curve for a Type-0 process. The contour provides some important

information regarding the resultant output of the SPDC process. Mathematically, the output state of the downconversion process can be described as:

$$|\Psi\rangle = \int\int \gamma\left(\omega_s, \omega_i\right) d\omega_s d\omega_i a_s^\dagger a_i^\dagger |0\rangle \tag{A.1}$$

whereby the joint spectral amplitude (JSA), $\gamma\left(\omega_s, \omega_i\right)$ is the product of two terms, the pump-envelope function $\mu\left(\omega_s, \omega_i\right)$ and the phase-matching amplitude $\phi\left(\omega_s, \omega_i\right)$ [2]. Here the phase-matching amplitude function is solely determined by the crystal and the desired downconversion configuration. The pump-envelope function on the other hand is dictated by, as the name implies, the spectral characteristic of the pump beam. Obviously due to conservation of energy, μ will be diagonal in its orientation if plotted as a function of the signal and idler wavelengths.

The strongly diagonal direction of ϕ is advantageous as its overlap with the pump-envelope along the diagonal allows for a wide range of anti-correlated signal and idler photon pairs to be phase-matched. This is of particular importance in experiments where this anti-correlation is necessary for achieving two-photon absorption processes which occur via an intermediate energy level transition [3]. This can be viewed in contrast to applications where highly spectrally pure photon states are desired, such as in single photon sources. Here, obtaining a lack of frequency correlations by designing an anti-diagonal direction of ϕ is of primary concern.

A.4 Entanglement and purity

Given the output state as defined in Eq. A.1, the joint spectral amplitude allows for the prediction of the SPDC spectrum obtained for a given configuration of μ and ϕ by carrying out an integral across all signal/idler wavelengths with respect to a corresponding idler/signal wavelength held constant. For our specific 20 mm long ppCLT grating with a 9.5 μm poling period, the pump bandwidth has a distinct effect on not only the resulting emission spectrum's bandwidth, but also more profoundly on the entanglement of the photonic state. This is characterized by the purity,

$$P = \frac{1}{K} \tag{A.2}$$

with

$$K = \frac{1}{\Sigma_i \lambda_i^2} \tag{A.3}$$

being the Schmidt number equal to the rank of the reduced single particle density matrix. This value can be interpreted as a weighted measure (weights being the eigenvalues λ_i) of the number of modes required to represent the mixed state, and

therefore how entangled it is [4]. The eigenvalues themselves are obtained via a singular value decomposition of the joint spectral amplitude matrix. As shown in Fig. A.4 (top), the SPDC spectrum trivially narrows as the pump bandwidth is decreased up to a limiting point. Below this value, the intersection of the pump envelope μ with the phase matching amplitude ϕ no longer causes a decrease in the spectral width which is being carved out by μ. Fig. A.4 (bottom) shows the calculated FWHM of the SPDC spectrum as a function of the pump bandwidth, as well as the corresponding purity of the output state. As is evident, the purity of the state decreases with increasing pump bandwidths, and therefore conversely the entanglement of the overall state increases. While this is advantageous from the perspective of producing a state which displays more/stronger anti-correlations between photon pairs, the significant drawback is that the spectral resolution with which optical atomic and molecular transitions are able to be addressed is directly determined by the bandwidth of the pump laser driving the SPDC process. Thus, for highly spectrally resolved measurements, the figure of merit will be dictated by the pump laser.

A.5 Broadband HOM interference

The temporal properties and the degree of entanglement of the SPDC flux can be assessed by measuring the fourth-order interference in a two-photon Michelson (or Mach-Zehnder) interferometer. In such an interferometer, six beamsplitter ports are involved. See diagram below (Fig. A.5).

The interferometer input wavefunction for entangled pairs entering BS1 via port a is

$$|\Psi\rangle \propto \iint d\omega_s d\omega_i \psi(\omega_s, \omega_i) \hat{a}_s^\dagger(\omega_s) \hat{a}_i^\dagger(\omega_i) \, |0,0\rangle \tag{A.4}$$

where $\psi(\omega_s, \omega_i)$ is the joint spectral amplitude of the entangled photons as defined in previous sections.

After the first pass through BS1,

$$\hat{a}_s^\dagger(\omega_s)\hat{a}_i^\dagger(\omega_i) \;=\; \frac{1}{2}[\hat{c}_s^\dagger(\omega_s)\hat{c}_i^\dagger(\omega_i) - \hat{d}_s^\dagger(\omega_s)\hat{d}_i^\dagger(\omega_i) + i\hat{c}_s^\dagger(\omega_s)\hat{d}_i^\dagger(\omega_i) + i\hat{d}_s^\dagger(\omega_s)\hat{c}_i^\dagger(\omega_i)]. \tag{A.5}$$

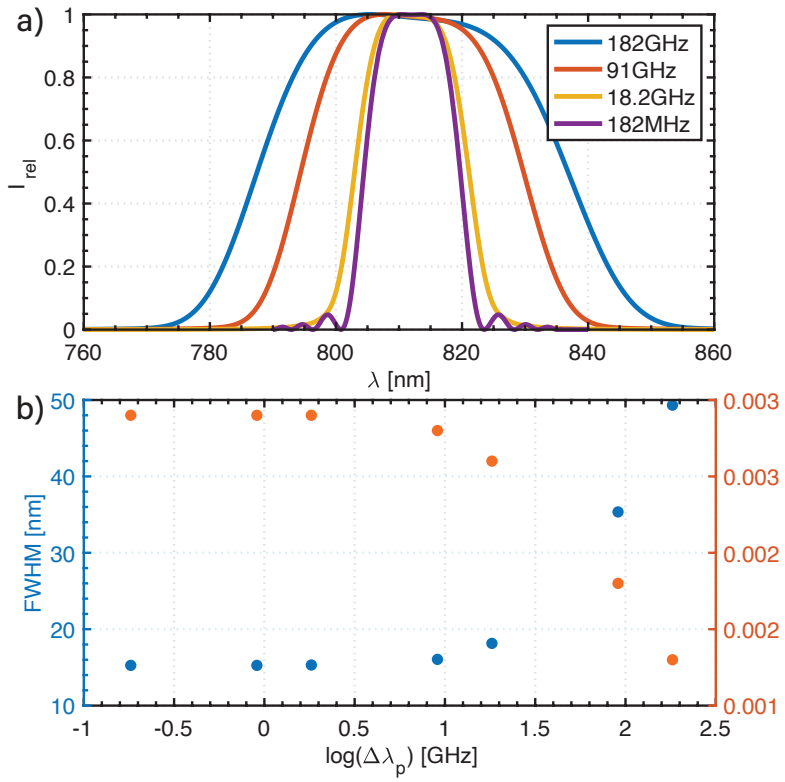

Figure A.4: SPDC emission spectrum as a function of the pump bandwidth. The corresponding broadening of the spectrum at larger bandwidths carries with it a degradation of the photon state purity which is of advantage where strong (anti-) correlation between photon pairs is desired.

After the second pass

$$\begin{aligned}\hat{a}_s^\dagger(\omega_s)\hat{a}_i^\dagger(\omega_i) \;=\; & \frac{1}{4}\left[1+e^{i\omega_p\tau}-e^{i\omega_i\tau}-e^{i\omega_s\tau}\right]\hat{e}_s^\dagger(\omega_s)\hat{e}_i^\dagger(\omega_i)\\ & +\frac{i}{4}\left[1-e^{i\omega_p\tau}+e^{i\omega_i\tau}-e^{i\omega_s\tau}\right]\hat{e}_s^\dagger(\omega_s)\hat{f}_i^\dagger(\omega_i)\\ & +\frac{i}{4}\left[1-e^{i\omega_p\tau}-e^{i\omega_i\tau}+e^{i\omega_s\tau}\right]\hat{f}_s^\dagger(\omega_s)\hat{e}_i^\dagger(\omega_i)\\ & -\frac{1}{4}\left[1+e^{i\omega_p\tau}+e^{i\omega_i\tau}+e^{i\omega_s\tau}\right]\hat{f}_s^\dagger(\omega_s)\hat{f}_i^\dagger(\omega_i).\end{aligned} \tag{A.6}$$

Since the coincidences are detected after port f, the last term of the above expression is relevant. Using the fact that $\omega_i = \omega_p - \omega_s$, the ff component of the entangled two photon wavefunction becomes

$$\begin{aligned}|\Psi\rangle_{ff} &\propto -\frac{1}{4}\iint d\omega_s d\omega_i \psi(\omega_s,\omega_i)\left[1+e^{i\omega_p\tau}(1+e^{-i\omega_s\tau})+e^{i\omega_s\tau}\right]\hat{f}_s^\dagger(\omega_s)\hat{f}_i^\dagger(\omega_i)\,|0,0\rangle\\ &= -\sqrt{2}\int d\omega_s \psi(\omega_s,\omega_p-\omega_s)\left[1+cos((\omega_p-\omega_s)\tau)\right]\left[1+cos(\omega_s\tau)\right]\;|0,2\rangle\,.\end{aligned} \tag{A.7}$$

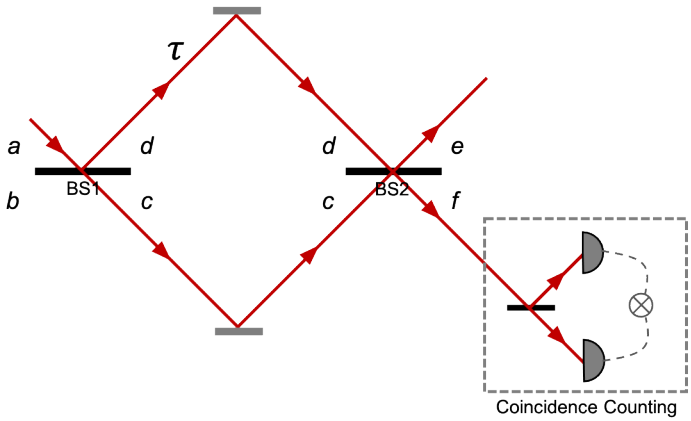

Figure A.5: Schematics of a two-photon Michelson or Mach-Zehnder interferometer.

Note that here it was assumed that ω_p is constant and the pump laser has an infinitely narrow line width. Therefore, the probability of detecting coincidences after port f is

$$P \propto 2 \int d\omega_s |\psi(\omega_s, \omega_p - \omega_s)|^2 [1 + cos((\omega_p - \omega_s)\tau)]^2 [1 + cos(\omega_s \tau)]^2 \quad \text{(A.8)}$$

where $|\psi(\omega_s, \omega_p - \omega_s)|^2$ is the joint spectral density of the entangled photons. Thus the interference pattern at port f can be plotted out (Fig. A.6 and A.7). The interference pattern is the result of contributions from both classical and quantum (HOM) interferences. The effect of HOM is manifested by the main peak at zero time delay. As the bandwidth of the entangled photons change, either by varying phase matching conditions or simply placing a bandpass filter before the photon counting detectors, the width of the interference peak, proportional to the coherence length of the flux, changes accordingly.

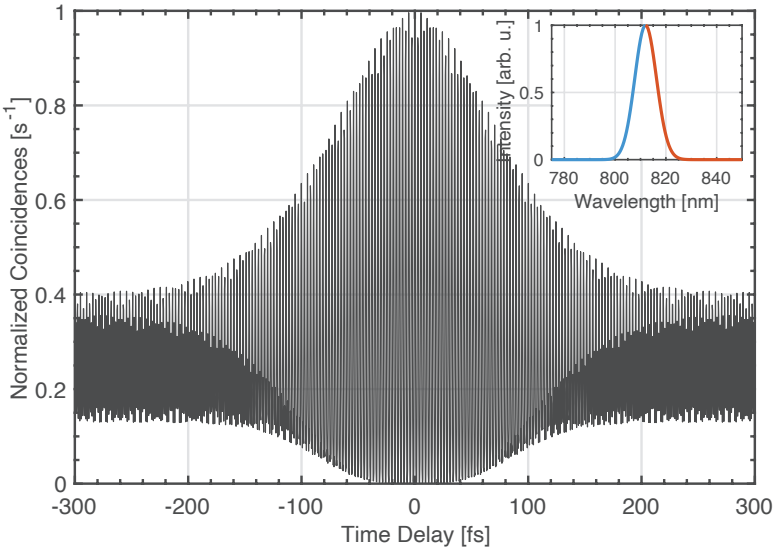

Figure A.6: Simulated normalized narrowband Michelson interference corresponding to the Gaussian SPDC spectrum filtered by 10 nm bandpass filter centered at 812 nm. Sampling step 0.32 fs.

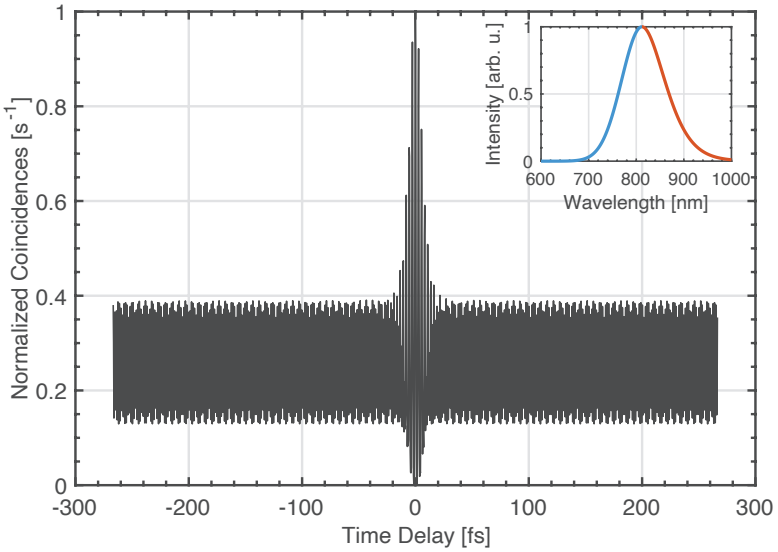

Figure A.7: Simulated normalized broadband Michelson interference corresponding to the Gaussian SPDC spectrum filtered by 125 nm bandpass filter centered at 812 nm. Sampling step 0.32 fs.

Additional experimental data

Figs. A.8, A.9, A.10, A.11 provide additional characterization on the relationship between interference measurements and the pump.

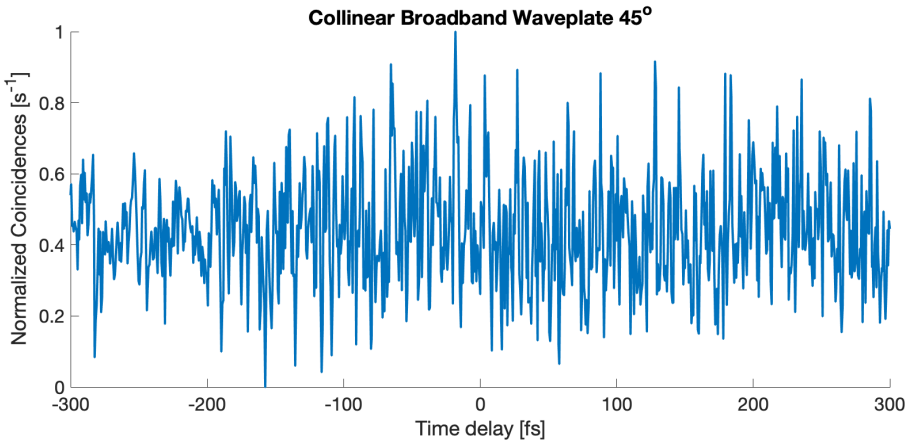

Figure A.8: Measured collinear broadband two-photon interference when the arms of the Michelson interferometer are perpendicularly polarized. No distinguishable interference pattern is observed, and the coincidences follow pump and noise fluctuations.

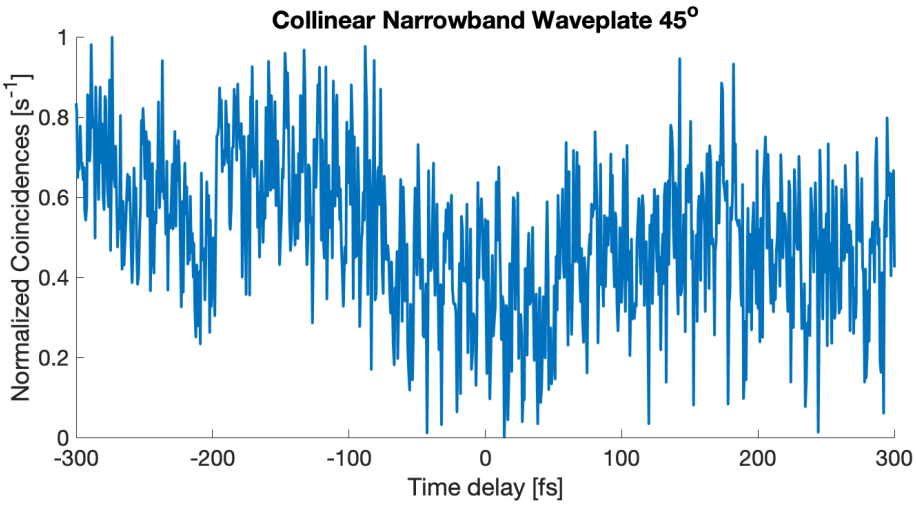

Figure A.9: Measured collinear narrowband two-photon interference when the arms of the Michelson interferometer are perpendicularly polarized. No distinguishable interference pattern is observed, and the coincidences follow pump and noise fluctuations.

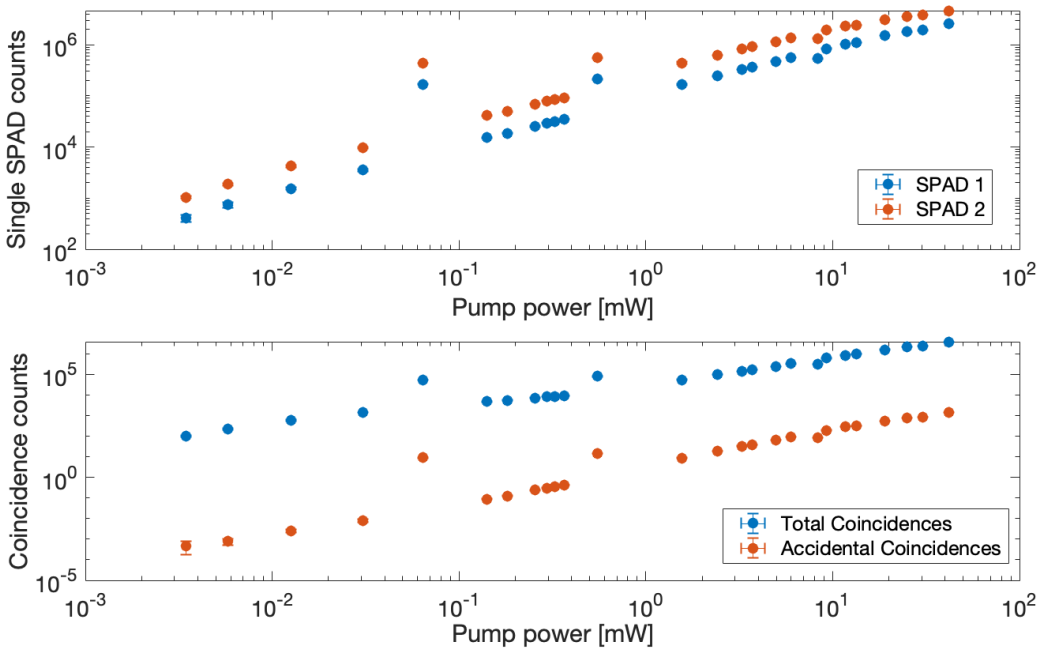

Figure A.10: Measured SPAD counts and coincidences vs. pump power in the collinear broadband case. Top: single SPAD channel counts in 15s. Bottom: total and accidental coincidences in 15s.

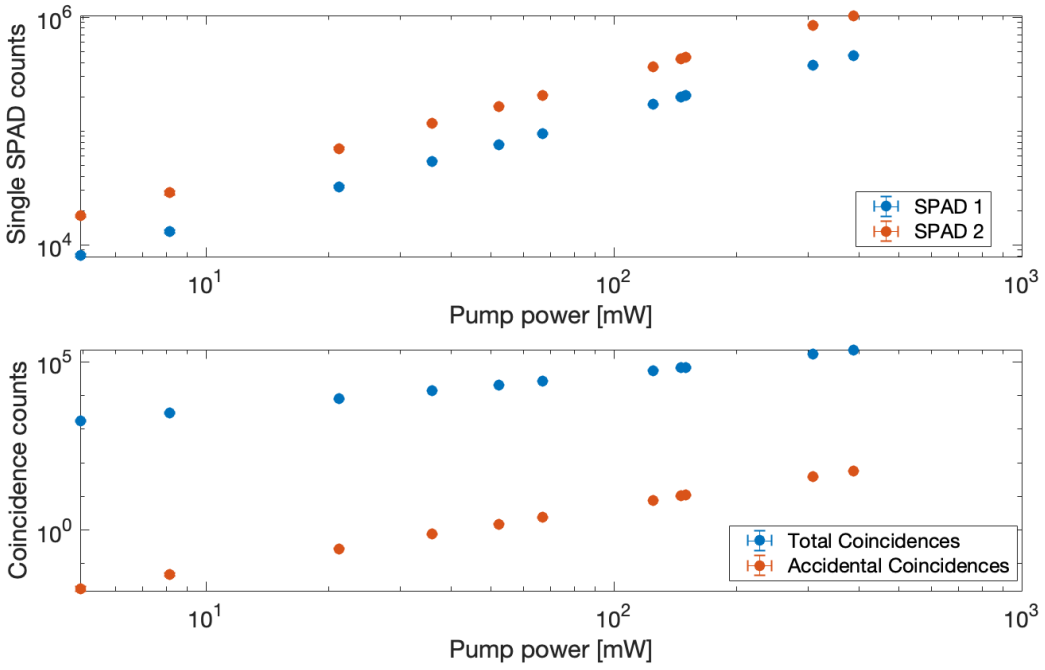

Figure A.11: Measured SPAD counts and coincidences vs. pump power in the collinear narrowband case. Top: single SPAD channel counts in 15s. Bottom: total and accidental coincidences in 15s.

References

1. Moutzouris, K., Hloupis, G., Stavrakas, I., Triantis, D. & Chou, M.-H. Temperature-dependent visible to near-infrared optical properties of 8 mol% Mg-doped lithium tantalate. *Optical Materials Express* **1,** 458–465. `https://www.osapublishing.org/ome/abstract.cfm?uri=ome-1-3-458` (2011).

2. Zielnicki, K. *et al.* Joint Spectral Characterization of Photon-Pair Sources. *Journal of Modern Optics* **65,** 1141–1160. `http://arxiv.org/abs/1801.01195` (2018).

3. Saleh, B. E. A., Jost, B. M., Fei, H.-B. & Teich, M. C. Entangled-Photon Virtual-State Spectroscopy. *Physical Review Letters* **80,** 3483–3486. `https://link.aps.org/doi/10.1103/PhysRevLett.80.3483` (1998).

4. Ekert, A. & Knight, P. L. Entangled quantum systems and the Schmidt decomposition. *American Journal of Physics* **63,** 415–423. `https://doi.org/10.1119/1.17904` (1995).

Appendix B

SUPPLEMENTARY INFORMATION FOR SINGLE PHOTON SCATTERING CAN ACCOUNT FOR THE DISCREPANCIES BETWEEN ENTANGLED TWO-PHOTON MEASUREMENT TECHNIQUES

B.1 Linear absorption measurement

In previous experimental protocols, the ETPA cross section was quantified by measuring the attenuation of entangled photon pairs transmitted through a molecular sample [1–7]. Here, we perform a similar study on a solution of 5 mM R6G in water by directly focusing the output of the ppLT chip into a sample cuvette and monitoring the transmitted photon counts with a spectrometer/EMICCD as the pump power is varied. The process is repeated for a blank water standard. The absorption cross section reported in Fig. 4.5 is calculated from a plot of the transmitted photon rate vs. the input photon rate using the following steps:

$$A = \varepsilon l c \tag{B.1}$$

$$\varepsilon = \frac{N_A}{\ln 10}\sigma \tag{B.2}$$

$$T = \frac{I_{sample}}{I_{solvent}} = 10^{-A} \tag{B.3}$$

$$\log_{10}\frac{I_{sample}}{I_{solvent}} = \log_{10} 10^{-A} = -A \tag{B.4}$$

$$\log_{10}\frac{I_{sample}}{I_{solvent}} = \varepsilon(1\text{cm})(5\text{mM}) \tag{B.5}$$

$$\log_{10}\frac{I_{sample}}{I_{solvent}} = \frac{6.02 * 10^{23}\frac{\text{molecule}}{\text{mole}}}{\ln 10} * \sigma * (1\text{cm}) * \left(\frac{0.005\text{mole}}{1000\text{cm}^3}\right) \tag{B.6}$$

$$\log_{10}\frac{I_{sample}}{I_{solvent}} = 2.8759 * 10^{19}\frac{\text{molecule}}{\text{cm}^2} * \sigma \tag{B.7}$$

$$\sigma = -\frac{1}{2.8759 * 10^{19}}\frac{\text{cm}^2}{\text{molecule}}\log_{10}\frac{I_{sample}}{I_{solvent}} \tag{B.8}$$

$$\sigma = -\frac{1}{2.8759 * 10^{19}}\frac{\text{cm}^2}{\text{molecule}}\log_{10}(0.9725) \tag{B.9}$$

$$\sigma = 4 * 10^{-21}\frac{\text{cm}^2}{\text{molecule}}. \tag{B.10}$$

In other experimental protocols, the sample with solvent counts are subtracted from the solvent counts to yield an absorbed photon rate, which is plotted against the input photon rate. The ETPA cross section is then calculated from the slope of the linear fit using the following equation:

$$\sigma_E = \frac{m}{lcN_A} \tag{B.11}$$

where σ_E is the ETPA cross section, m is the slope of the linear fit, l is the path length of the cuvette, c is the sample concentration, and N_A is Avogadro's number. A cross section of $8(\pm 1) * 10^{-21}$ cm^2/molecule was measured using this linear transmission method.

It is important to note that for an entangled photon pair, when performing coincidence counting, if one photon is lost then the entangled state is broken. In other words, the losses scale as the intensity squared because if one photon is lost neither of the two photons is measured by the coincidence detection. Squaring the measured scattering amplitude gives good agreement with the linear measurement, further confirming that for the measured virtual state molecules, any entangled enhancement is less than the scattering process. It should also be noted that a one photon scattering will lead to a linear slope just as the proposed linearization of the two-photon process.

B.2 Interferogram simulation

To simulate the interferograms shown in the right panel of Fig. B.2, the measured interferograms (left) are first Fourier transformed to reveal the different frequency components, shown below in Fig. B.1. The 1f peaks, which possess the same frequencies as the original interfering photons, are fitted with double or single Gaussian peaks (solid lines, Fig. B.1). For entangled two-photon Michelson cases (Fig. B.1a,b), the fitted peaks follow the distribution of entangled joint spectral amplitudes (JSA), and are then used as the input JSA for entangled fourth-order interference simulation (see section "Broadband fourth-order interference"). For example, for the single peaks, the JSA takes the form of

$$\phi(\lambda_s, \lambda_p) = \frac{1}{\sigma_{SPDC}\sqrt{2}} \exp\left\{ \frac{(\lambda_s - 2\lambda_p)^2}{2\sigma_{SPDC}^2} \right\} \tag{B.12}$$

where λ_s is the wavelength of the signal, λ_p is the center wavelength of the pump, $\sigma_{SPDC} = \frac{FWHM}{2\sqrt{2\ln 2}}$ where $FWHM$ is the full width half maximum of the fitted peaks.

For the case of single-photon Michelson (Fig. B.1c), the fitted peak is a single Gaussian representing single-photon scatter, which is then used as the input spec-

trum for classical single-photon Michelson simulation. The resultant simulated interferograms are shown in Fig. B.2 right panel.

Fourier transform of measured interferograms

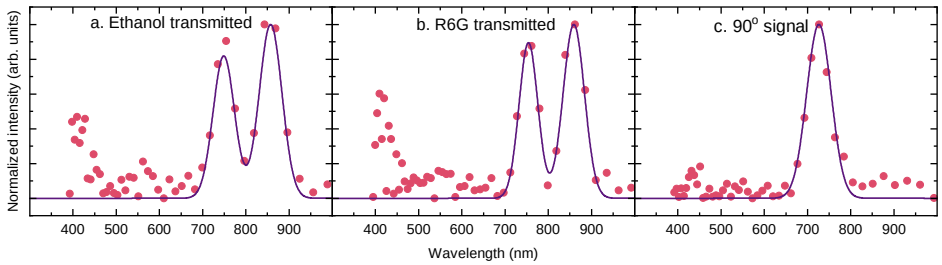

Figure B.1: Fourier transform of measured interferograms (pink scatter points) showing 1f and 2f components, which correspond to the interfering photon and the SPDC pump frequencies, respectively. Note that the 2f components in the left and middle panels are the result of interference between the pathways of unseparated entangled photon pairs, not single photons at the pump frequency. To obtain input spectra/JSA for interference simulation, the 1f components are fitted into Gaussian peaks (purple solid lines).

Comparison of experimental and simulated interferograms of transmitted coincidence

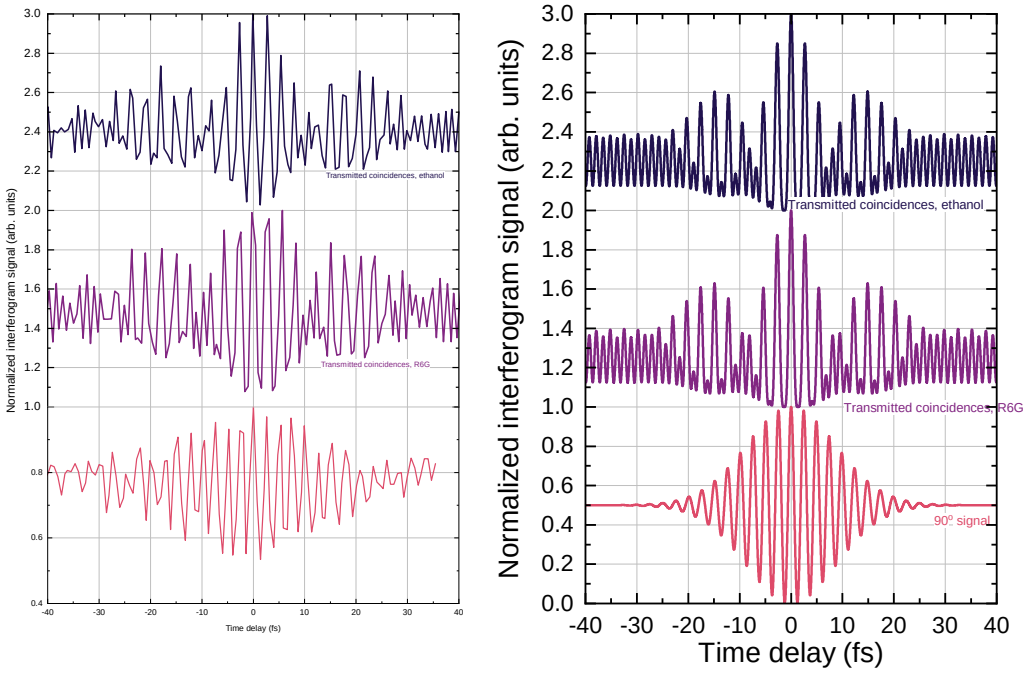

Figure B.2: Photon counts scaled to 1 vs time delay for non-degenerate bandwidth entangled photons traveling through a two-photon Michelson interferometer. Parameters from Gaussian fits of spectra obtained by Fourier-transforming the experimental interferograms (left) are used to simulate the two-photon Michelson interferograms (right). For more details on simulation method, see previous section "Interferogram simulation." No modulation of the quantum state is observed when ethanol is replaced with an R6G/ethanol solution and the resulting 90-degree signal follows a one photon process.

B.3 Broadband fourth-order interference

Characterization of the temporal properties and visibility of the entangled state measured through the fourth-order interference with a two-photon Michelson interferometer. This setup has been previously theoretically modeled and experimentally verified [8, 9]. The two-photon Michelson interferometer consists of six beamsplitter ports, as shown in Fig. B.3.

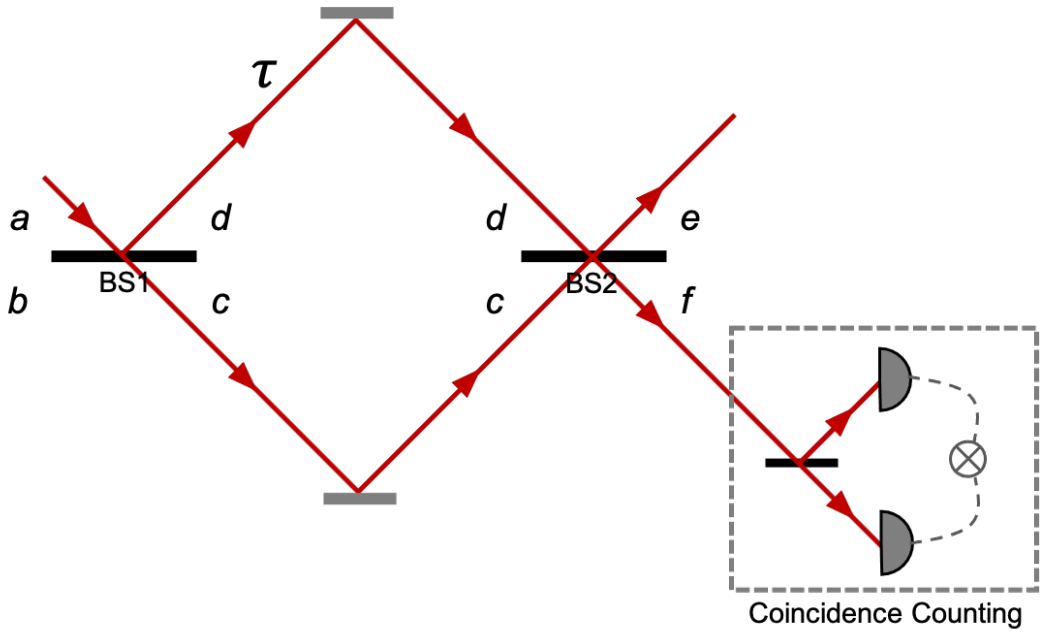

Figure B.3: Schematics of a two-photon Michelson or Mach-Zehnder interferometer.

The theoretical derivation of the interferogram we expect to observe is as follows:

Spontaneous parametric down conversion (SPDC) of a pump photon with frequency ω_p generates an entangled photon pair with signal and idler frequencies ω_s and ω_i, respectively, described by the wavefunction

$$|\Psi\rangle \propto \iint d\omega_s d\omega_i \phi(\omega_s, \omega_i) \hat{a}_s^\dagger(\omega_s) \hat{a}_i^\dagger(\omega_i) \, |0,0\rangle \tag{B.13}$$

where $\phi(\omega_s, \omega_i)$ is the joint spectral amplitude (JSA) of the entangled photons, and the vacuum component of $|\Psi\rangle$ is omitted. The JSA is normalized such that $\iint d\omega_s d\omega_i |\phi(\omega_s, \omega_i)|^2 = 1$, and is symmetrized such that $\phi(\omega_s, \omega_i) = \phi(\omega_i, \omega_s)$ because the signal and idler are indistinguishable in a type-0 SPDC source.

Upon first pass of BS1, the operators assume the form

$$\begin{aligned} &\hat{a}_s^\dagger(\omega_s) \hat{a}_i^\dagger(\omega_i) \xrightarrow{\hat{U}_{BS1}} \\ &\quad \frac{1}{2}[\hat{c}_s^\dagger(\omega_s) \hat{c}_i^\dagger(\omega_i) - \hat{d}_s^\dagger(\omega_s) \hat{d}_i^\dagger(\omega_i) + i\hat{c}_s^\dagger(\omega_s) \hat{d}_i^\dagger(\omega_i) + i\hat{d}_s^\dagger(\omega_s) \hat{c}_i^\dagger(\omega_i)] \end{aligned} \tag{B.14}$$

where it is assumed that the beam splitter has an equal transmittivity and reflectivity of 50% and no frequency dependence.

Following a time delay, τ, introduced in port d and a second pass through BS1, the operators transform as:

$$\begin{aligned}\hat{a}_s^\dagger(\omega_s)\hat{a}_i^\dagger(\omega_i) \rightarrow & \frac{1}{4}[1+e^{i\omega_p\tau}-e^{i\omega_i\tau}-e^{i\omega_s\tau}]\hat{e}_s^\dagger(\omega_s)\hat{e}_i^\dagger(\omega_i) \\ & +\frac{i}{4}[1-e^{i\omega_p\tau}+e^{i\omega_i\tau}-e^{i\omega_s\tau}]\hat{e}_s^\dagger(\omega_s)\hat{f}_i^\dagger(\omega_i) \\ & +\frac{i}{4}[1-e^{i\omega_p\tau}-e^{i\omega_i\tau}+e^{i\omega_s\tau}]\hat{f}_s^\dagger(\omega_s)\hat{e}_i^\dagger(\omega_i) \\ & -\frac{1}{4}[1+e^{i\omega_p\tau}+e^{i\omega_i\tau}+e^{i\omega_s\tau}]\hat{f}_s^\dagger(\omega_s)\hat{f}_i^\dagger(\omega_i).\end{aligned} \tag{B.15}$$

The rate of coincidence counts in port f, R_{ff} is obtained by is obtained by projecting the wavefunction onto the response of two single-photon detectors with the projector P_{ff}. We assume that the photodectors have a flat frequency response over the bandwidth of the SPDC, and that the integration time of the detectors is significantly longer than the coherence time of the pairs:

$$\begin{aligned}R_{ff} \propto \langle\Psi|P_{ff}|\Psi\rangle &\approx \iint d\omega_1 d\omega_2 \, \langle\Psi|\hat{f}^\dagger(\omega_1)\hat{f}^\dagger(\omega_2)|0\rangle \, \langle 0|\hat{f}^\dagger(\omega_1)\hat{f}^\dagger(\omega_2)|\Psi\rangle \\ &= \iint d\omega_1 d\omega_2 |\, \langle 0|\hat{f}(\omega_1)\hat{f}(\omega_2)|\Psi\rangle \,|^2.\end{aligned} \tag{B.16}$$

The effect of this projection operator is that only the component of $|\Psi\rangle$ with both photons in port f contributes to the observed coincidences. Inserting equations 2 and 4 yields a four-dimensional integral, which is then simplified using the identity $\langle 0|\hat{f}(\omega_a)\hat{f}(\omega_b)|\Psi\rangle = \delta(\omega_a - \omega_b)$ to a two-dimensional integral:

$$R_{ff} \propto \iint d\omega_s d\omega_i |1+e^{i(\omega_s+\omega_i)\tau}+e^{i\omega_s\tau}+e^{i\omega_i\tau}|^2|\phi(\omega_s,\omega_i)|^2. \tag{B.17}$$

To further simplify Eqn. B.17, we approximate the JSA from our source as follows. Due to energy conservation, $\phi(\omega_s, \omega_i)$ will be proportional to the amplitude of the pump beam at the sum of the pair frequency, $\alpha(\omega_s + \omega_i)$, and will also be proportional to the phase-matching amplitude of the crystal, $\Phi(\omega_s, \omega_i)$, which is symmetric about $\omega_s = \omega_i$:

$$\phi(\omega_s,\omega_i) \propto \alpha(\omega_s+\omega_i)\Phi(\omega_s,\omega_i). \tag{B.18}$$

Due to the narrow bandwidth of the pump laser, we approximate the pump amplitude function as a delta function at $\lambda = 406$ nm. The joint spectral intensity (the square of the JSA) becomes

$$|\phi(\omega_s, \omega_i)|^2 = \delta(\omega_p - \omega_s - \omega_i) S(\omega_s) \tag{B.19}$$

where $S(\omega_s)$ is the spectral density of the SPDC (the spectrum of the pairs as measured by a spectrometer) and is symmetric about $\omega_s = \omega_p/2$. Inserting Eqn. B.19 into Eqn. B.17 reduces the two-dimensional integral to a single-dimensional integral, which is then simplified further using standard trigonometric identities:

$$R_{ff} \propto \int d\omega_s |1 + e^{i(\omega_s+\omega_i)\tau} + e^{i\omega_s\tau} + e^{i(\omega_p-\omega_s)\tau}|^2 S(\omega_s) \tag{B.20}$$

$$\propto \int d\omega_s [1 + \cos\big((\omega_p - \omega_s)\tau\big)][1 + \cos(\omega_s\tau)] S(\omega_s). \tag{B.21}$$

The quality of the Michelson interferogram can be inferred from its visibility, calculated as

$$V = \frac{R_{maximum} - R_{minimum}}{R_{maximum} + R_{minimum}}. \tag{B.22}$$

B.4 Entangled photon spectra

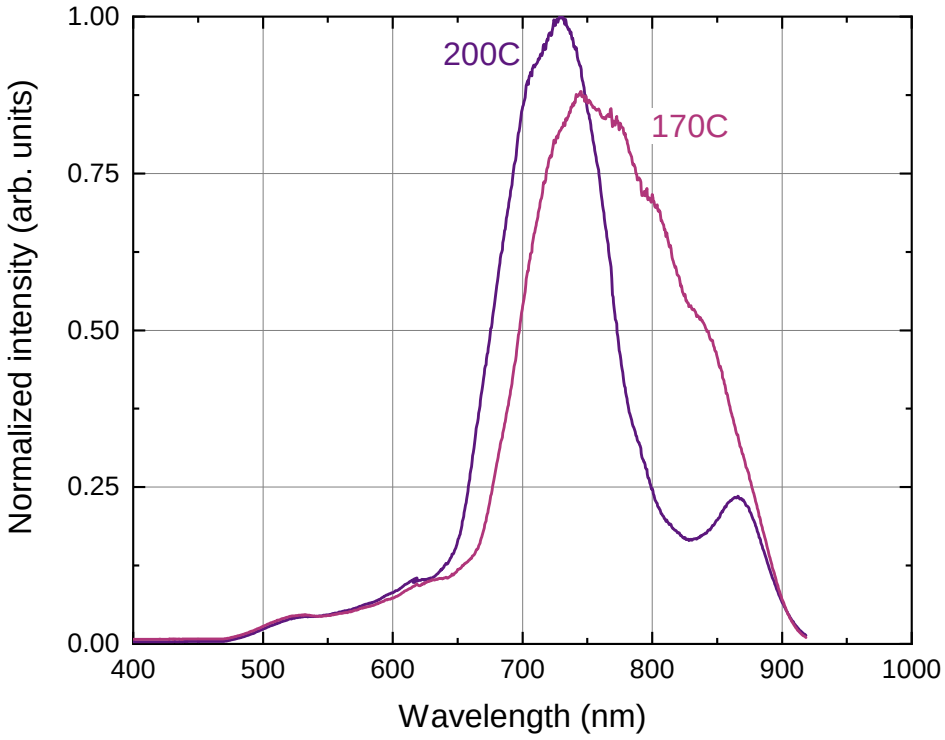

Figure B.4: Normalized spectra of the entangled photons for two ppLT crystal temperatures (changing the phase matching parameters). The 200℃ entangled photons (purple trace) are described as the nondegenerate spectrum while the 170℃ entangled photons (pink trace) are described as the degenerate spectrum. Note that the EMICCD has a quantum efficiency that tails to ~ 900 nm, giving the high wavelength cutoff slope seen for both spectra.

B.5 Absorption spectra of studied compounds

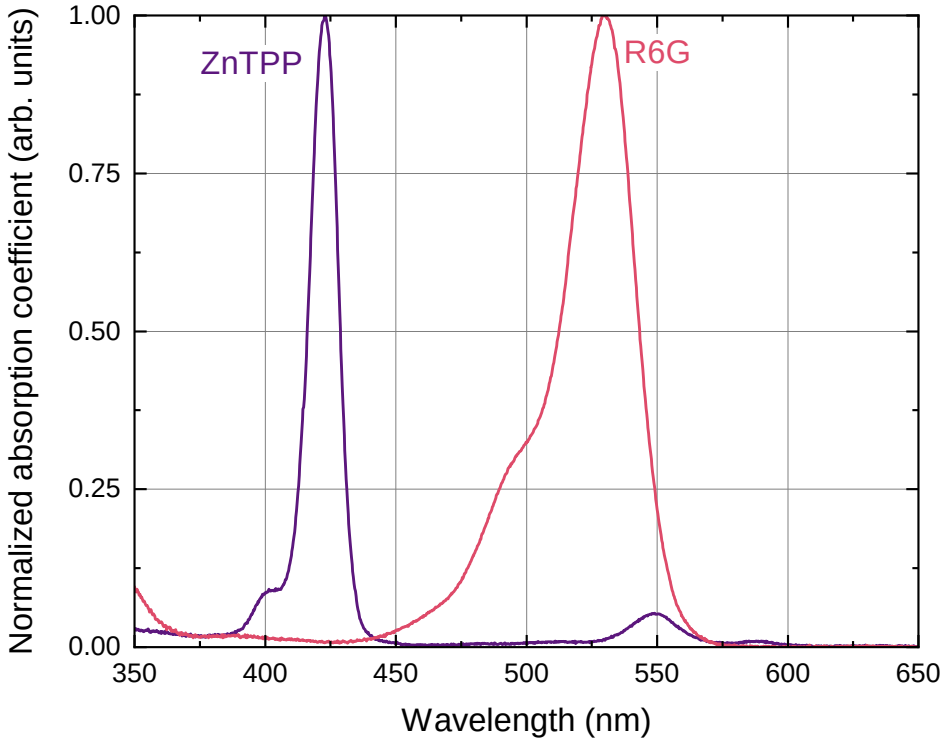

Figure B.5: Normalized absorption spectra of zinc tetraphenylporphyrin (ZnTPP, purple trace) and Rhodamine 6G (R6G, pink trace) [10].

B.6 Degenerate entangled photons

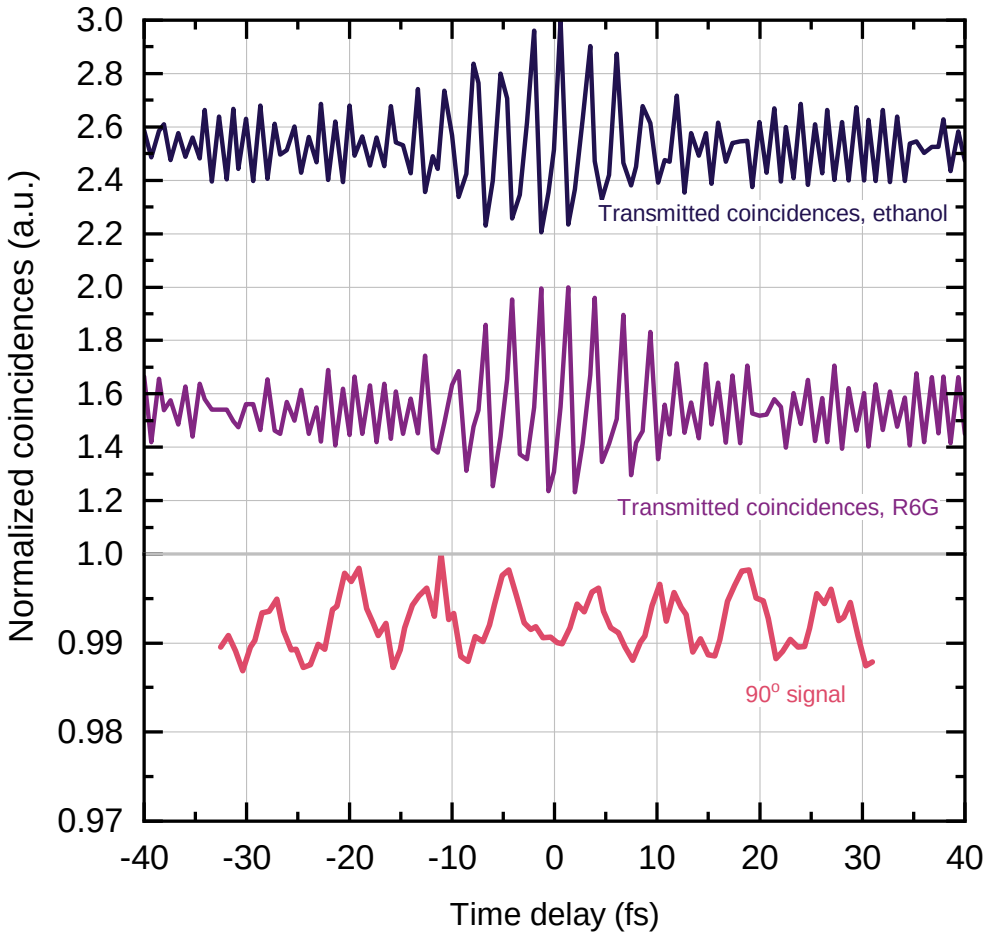

Figure B.6: Photon counts scaled to 1 vs time delay for degenerate bandwidth entangled photons traveling through a two-photon Michelson interferometer. The top trace is coincidence counts with solvent, the middle trace is transmitted coincidence counts with R6G, and the bottom trace is summed CCD counts of the 90-degree signal. Note that the scale of the y axis is shifted below values of 1 so that the bottom trace can be better visualized.

B.7 Zinc tetraphenylporphyrin

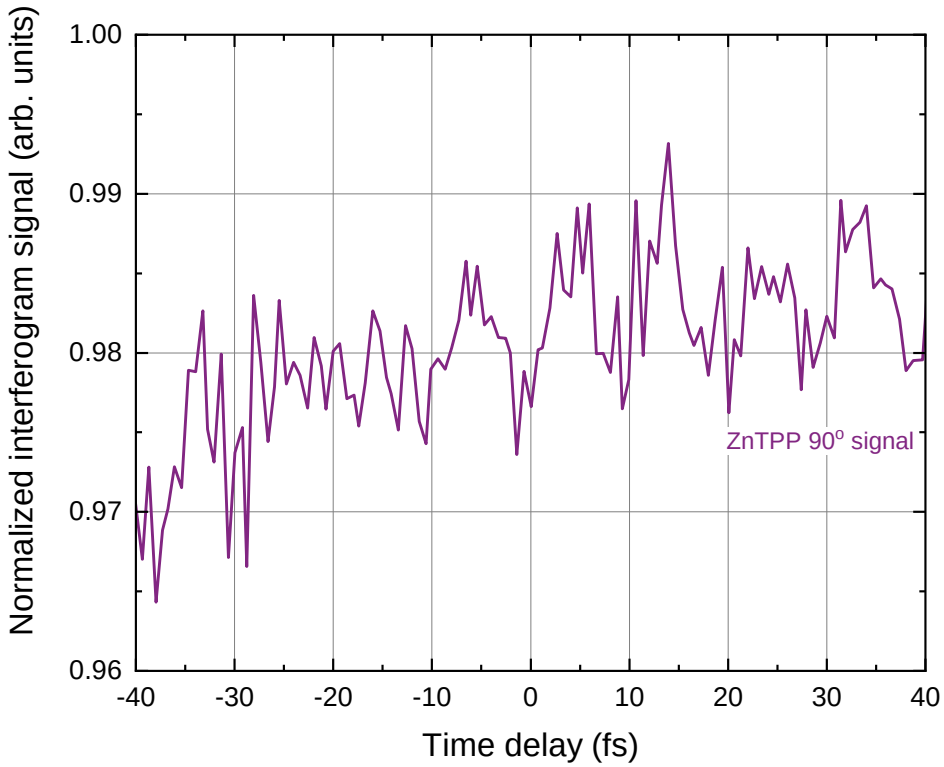

Figure B.7: Normalized 90-degree summed EMICCD counts versus time delay of broadband entangled photons focused into a solution of zinc tetraphenylporphyrin (ZnTPP). The signal here is purely a result of the noise of the EMICCD camera.

B.8 Destruction of entanglement with a quarter-wave plate

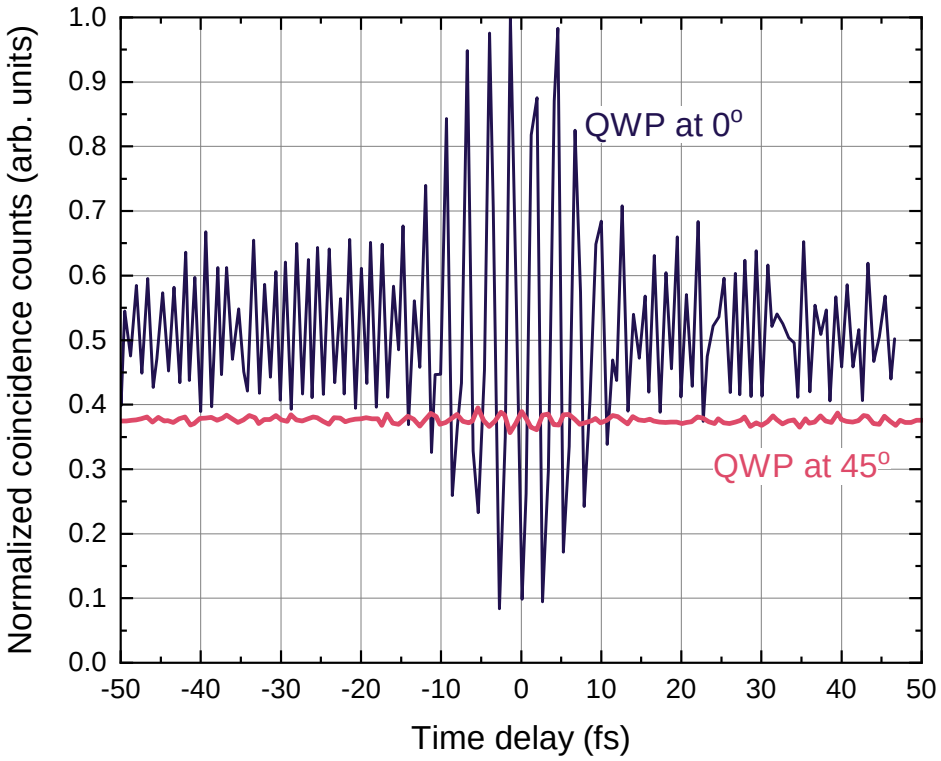

Figure B.8: Normalized coincidences when the quarter-wave plate (QWP) in one of the arms of the two-photon Michelson interferometer is adjusted from 0° (purple line) to 45° (pink line) to polarize the entangled photons 90° with respect to each other. The baseline of the resulting interferogram (pink line) has been corrected with a multiplication factor to account for the deviation from the ideal 50 : 50 beam splitter ratio as the polarization state is varied. This non-ideal ratio also contributes to the low visibility (< 0.04) oscillations around time zero.

B.9 Absorbed photon rate vs. input photon rate

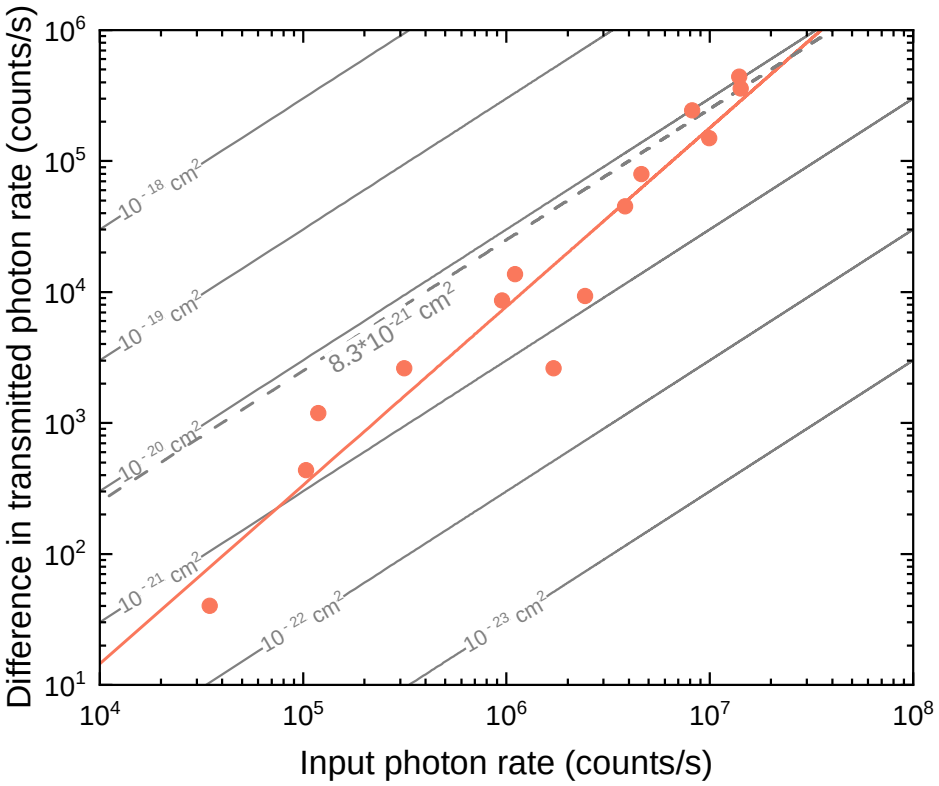

Figure B.9: Measured absorbed photon rate (orange data points, calculated from: $R_{solvent} - R_{sample}$, a popular method used literature) and fit (orange solid line) vs input photon rate for 5 mM Rhodamine 6G in water. The slope of the line of best fit for this data is 1.3. Using the method standard in literature, the ETPA cross section from the measured absorption rate would be $8(\pm 1) * 10^{-21}$ cm^2/molecule. In this manuscript, the linear relationship is determined to not be from ETPA, but rather from a single photon scattering process. Note that the error bars for each data point are on the order of the graph point size.

References

1. Lee, D.-I. & Goodson, T. Entangled Photon Absorption in an Organic Porphyrin Dendrimer. *The Journal of Physical Chemistry B* **110,** 25582–25585. `https://pubs.acs.org/doi/10.1021/jp066767g` (2006).

2. Harpham, M. R., Suzer, O., Ma, C.-Q., Bauerle, P. & Goodson, T. Thiophene Dendrimers as Entangled Photon Sensor Materials. *Journal of the American Chemical Society* **131,** 973–979. `https://doi.org/10.1021/ja803268s` (2009).

3. Guzman, A. R., Harpham, M. R., Suzer, O., Haley, M. M. & Goodson, T. G. Spatial Control of Entangled Two-Photon Absorption with Organic Chromophores. *Journal of the American Chemical Society* **132,** 7840–7841. https://doi.org/10.1021/ja1016816 (2010).

4. Upton, L. *et al.* Optically Excited Entangled States in Organic Molecules Illuminate the Dark. *The Journal of Physical Chemistry Letters* **4,** 2046–2052. https://doi.org/10.1021/jz400851d (2013).

5. Villabona-Monsalve, J. P., Calderón-Losada, O., Nuñez Portela, M. & Valencia, A. Entangled Two Photon Absorption Cross Section on the 808 nm Region for the Common Dyes Zinc Tetraphenylporphyrin and Rhodamine B. *The Journal of Physical Chemistry A* **121,** 7869–7875. https://doi.org/10.1021/acs.jpca.7b06450 (2017).

6. Villabona-Monsalve, J. P., Varnavski, O., Palfey, B. A. & Goodson, T. I. Two-Photon Excitation of Flavins and Flavoproteins with Classical and Quantum Light. *Journal of the American Chemical Society* **140,** 14562–14566. https://doi.org/10.1021/jacs.8b08515 (2018).

7. Villabona-Monsalve, J. P., Burdick, R. K. & Goodson, T. I. Measurements of Entangled Two-Photon Absorption in Organic Molecules with CW-Pumped Type-I Spontaneous Parametric Down-Conversion. *The Journal of Physical Chemistry C* **124,** 24526–24532. https://doi.org/10.1021/acs.jpcc.0c08678 (2020).

8. Lopez-Mago, D. & Novotny, L. Coherence measurements with the two-photon Michelson interferometer. *Physical Review A* **86,** 023820. https://link.aps.org/doi/10.1103/PhysRevA.86.023820 (2012).

9. Lavoie, J. *et al.* Phase-Modulated Interferometry, Spectroscopy, and Refractometry using Entangled Photon Pairs. *Advanced Quantum Technologies* **3,** 1900114. http://onlinelibrary.wiley.com/doi/abs/10.1002/qute.201900114 (2020).

10. Taniguchi, M. & Lindsey, J. S. Database of Absorption and Fluorescence Spectra of >300 Common Compounds for use in PhotochemCAD. *Photochemistry and Photobiology* **94,** 290–327. https://onlinelibrary.wiley.com/doi/abs/10.1111/php.12860 (2018).

Appendix C

SUPPLEMENTARY INFORMATION FOR EXPERIMENTAL UPPER BOUNDS FOR RESONANCE-ENHANCED ENTANGLED TWO-PHOTON ABSORPTION CROSS SECTION OF INDOCYANINE GREEN

C.1 Photon number per mode estimation

The number of photons per frequency mode, n, depends on the SPDC frequency bandwidth Δ_f and photon pairs rate r_{SPDC}. Specifically [1],

$$n = \frac{r_{SPDC}}{\Delta_f} \tag{C.1}$$

Given the SPDC pairs rate r_{pairs} of 1.9×10^{10} pairs/s and spectral bandwidth of 750-850 nm, n can be calculated as

$$n = \frac{2r_{pairs}}{\Delta_f} = \frac{2 \times 1.9 \times 10^{10} photons/s}{\frac{c}{750nm} - \frac{c}{850nm}} = 4 \times 10^{-4} \tag{C.2}$$

C.2 Derivation of ETPA cross section σ_{ETPA} and its equivalent TPA cross section δ_{TPA}

To derive the experimental upper bounds for σ_{ETPA} and its equivalent δ_{TPA} as shown in main text Table I for each measurement scheme, two values are required: the input photon count rate N_i which is the SPDC photon count rate measured after a cuvette of solvent, and the absorbed photon count rate N_{abs} which is the measured ETPA fluorescence photon rate divided by the quantum yield of the fluorophore. In this work, because no ETPA fluorescence is measured, the noise floor of the instrument divided by the fluorophore quantum yield is used for N_{abs}, and the resultant cross section values are meant as upper limits. Both count rates are corrected for detector quantum efficiencies at appropriate wavelengths and each experimental setup's collection efficiency as discussed in the main text.

The conventional ETPA absorption rate R is [2]

$$R = \sigma_{ETPA}\phi_i + \delta_{TPA}\phi_i^2 \tag{C.3}$$

where ϕ_i is the input photon flux, σ_{ETPA} is the ETPA cross section, and δ_{TPA} is the accidental TPA cross section.

Because our experiments operate at the highly isolated photon pairs regime, the second quadratic term of Eqn. C.3 is negligible compared with the first linear term [2, 3]. Calculating the σ_{ETPA} value is therefore straightforward using the natural logarithm of transmittance [4]:

$$\sigma_{ETPA} = -\frac{ln(1 - N_{abs}/N_i)}{N_A c l} \tag{C.4}$$

where N_A is the Avogadro constant, c is the concentration of the fluorophore, and l is the cuvette path length.

Now, if we assume instead that all the absorbed photons are due to accidental classical TPA, i.e. the second term of Eqn. C.3 dominates, then we may convert σ_{ETPA} to its equivalent δ_{TPA} value. The conversion relies on the photon flux ϕ, which is photon count per unit time per unit area [5, 6]:

$$\delta_{TPA} = \frac{\phi_{abs}}{\phi_i - \phi_{abs}} \cdot \frac{1}{N_A c l \phi_i} \tag{C.5}$$

where ϕ_i and ϕ_{abs} are the flux of input SPDC photons and the flux of absorbed photons, respectively. Thus $\phi_i = N_i/A$ and $\phi_{abs} = N_{abs}/A$, where A is the focusing area and is approximately the same for the input and absorbed photons. Further, given that $\phi_{abs} << \phi_i$, Eqn. C.5 can be simplified as

$$\delta_{TPA} \approx \frac{\phi_{abs}}{\phi_i} \cdot \frac{1}{N_A c l \phi_i} = \frac{N_{abs}}{N_i} \cdot \frac{1}{N_A c l \frac{N_i}{A}} = \frac{N_{abs}}{N_i^2} \cdot \frac{A}{N_A c l} = \frac{N_{abs}}{N_i^2} \cdot \frac{\pi r_0^2}{N_A c l} \tag{C.6}$$

where r_0 is the beam waist radius measured by a beam profiler as described in the Methods section of the main text.

C.3 Theoretical predictions for ICG σ_{ETPA}

Three theoretical models are used to predict the σ_{ETPA} value for ICG, as shown in main text Table II. Below we lay out the formulas and calculations for each model. For calculating cross sections, we use our experimental conditions when appropriate: 50 fs entanglement correlation time, 100 nm SPDC bandwidth centered at 806 nm, 35 μm focusing diameter, 20 GM measured classical TPA cross section ($\delta_{classical}$) for ICG.

Drago et al. [7]

The authors define the ETPA cross sections in relation to the squeezed TPA absorption rate R_{sq} as

$$R_{sq} = I_{sq}(I_{vac} + I_{sq})\sigma_{sq,I}^{2PA} + 2I_{sq}^2\sigma_{sq,II}^{2PA} \tag{C.7}$$

where I_{sq} is the squeezed (or entangled) light intensity. The parameter $I_{vac} = \frac{\hbar\omega_0}{AT_e}$ is the "vacuum intensity", where ω_0 is the center frequency of the SPDC spectrum, A is the focusing or entanglement area, and T_e is the entanglement coherence time. For our experimental conditions, I_{vac} is approximately 10^3 W/m^2. The $\sigma_{sq,I}^{2PA}$ and $\sigma_{sq,II}^{2PA}$ are two contributions of the squeezed TPA cross section and their values, which depend on the detuning of the SPDC center frequency from the ground to intermediate state transition frequency, are obtained via numerical analysis and expressed in GM. The conventional ETPA cross section (σ_{ETPA}) and classical TPA cross section ($\delta_{classical}$) can be used to express Eqn. C.7 as:

$$R_{sq} = I_{sq}\sigma_{ETPA} + I_{sq}^2 \cdot \delta_{classical} \tag{C.8}$$

Therefore,

$$\sigma_{ETPA} = (I_{vac} + I_{sq})\sigma_{sq,I}^{2PA} \tag{C.9}$$

and

$$\delta_{classical} = 2\sigma_{sq,II}^{2PA} << \sigma_{ETPA} \tag{C.10}$$

Because our experiments operate in the isolated pairs regime, and specifically our I_{sq} is on the order of 10 W/m^2, $I_{vac} >> I_{sq}$ and the second (quadratic) term of the absorption rate is negligible. Therefore Eqn. C.9 becomes

$$\sigma_{ETPA} \approx I_{vac}\sigma_{sq,I}^{2PA} = 10^3\text{W/m}^2 \cdot \sigma_{sq,I}^{2PA} \tag{C.11}$$

By plugging in the relevant cross section values presented by authors' numerical analysis, we find r-ETPA cross section for ICG to be in the range of 10^{-28} cm^2 to 10^{-26} cm^2, with the maximum achieved at detuning that equals exactly half of the

SPDC bandwidth. The v-ETPA cross section, obtained from the far-detuned limit where detuning is greater than 200 nm, is in the range of $< 10^{-29}$ cm^2. In our experiments, the SPDC excitation is on-resonance and has minimal detuning from the intermediate state, and therefore the predicted r-ETPA cross section for ICG will be closer to the lower end, on the order of 10^{-28} cm^2. This value is below our detection limit.

As described in Section C.2, the σ_{ETPA} value can be converted to an equivalent δ_{TPA} value which can then be used to compare with the molecule's classical TPA cross section. Specifically, the conversion relation in the isolated pairs regime is

$$R_{sq} \approx I_{sq}\sigma_{ETPA} = I_{sq}^2\delta_{TPA} \tag{C.12}$$

Therefore,

$$\delta_{TPA} = \frac{\sigma_{ETPA}}{I_{sq}} = \frac{(I_{vac} + I_{sq})\sigma_{sq,I}^{2PA}}{I_{sq}} \approx \frac{I_{vac}}{I_{sq}}\sigma_{sq,I}^{2PA} = 10^2 \cdot \sigma_{sq,I}^{2PA} \tag{C.13}$$

The resulting δ_{TPA} range for r-ETPA is 10^7 to 10^9 GM. Additionally, the authors also predict the range for classical r-TPA cross section to be 10^5 to 10^7 GM, which is unrealistically high according to experimental reports [4, 8] as well as our own measurement (20 GM). Taking the lower limit of the theory prediction and our measured r-TPA cross section, we can estimate the classical r-TPA cross section range as 10 to 10^5 GM. Comparing this range with r-ETPA's equivalent δ_{TPA} range of 10^7 to 10^9 GM, the enhancement on cross section due to entanglement is in the range of 2-8 orders of magnitude. This is also consistent with our experimental conclusion.

Landes et al. [9]

The authors predict that, experimentally, the ETPA cross section mainly depends on the bandwidth of the SPDC photons:

$$\sigma_{ETPA} = \frac{\delta_{classical}}{A} 2\Delta f \tag{C.14}$$

where Δf is the previously defined frequency bandwidth of SPDC, and is approximately 5×10^{13} Hz for our source. This results in a predicted σ_{ETPA} value of $\sim 10^{-30}$

cm^2. Note that this paper is a prediction for v-ETPA. It does consider homogeneous broadening due to dephasing in molecules.

Fei et al. [2]

According to the authors, the experimentally relevant ETPA cross section can be derived using a simple probabilistic model:

$$\sigma_{ETPA} = \frac{\delta_{classical}}{2AT_e} \tag{C.15}$$

Our experimental conditions lead to a σ_{ETPA} value of $\sim 10^{-31}$ cm^2. Note that this model is a prediction for atomic v-ETPA, and does not consider broadening effects in molecules.

References

1. Dayan, B., Pe'er, A., Friesem, A. A. & Silberberg, Y. Nonlinear Interactions with an Ultrahigh Flux of Broadband Entangled Photons. *Physical Review Letters* **94,** 043602. https://link.aps.org/doi/10.1103/PhysRevLett.94.043602 (2005).

2. Fei, H.-B., Jost, B. M., Popescu, S., Saleh, B. E. A. & Teich, M. C. Entanglement-Induced Two-Photon Transparency. *Physical Review Letters* **78,** 1679–1682. https://link.aps.org/doi/10.1103/PhysRevLett.78.1679 (1997).

3. Upton, L. *et al.* Optically Excited Entangled States in Organic Molecules Illuminate the Dark. *The Journal of Physical Chemistry Letters* **4,** 2046–2052. https://doi.org/10.1021/jz400851d (2013).

4. Hickam, B. P., He, M., Harper, N., Szoke, S. & Cushing, S. K. Single-Photon Scattering Can Account for the Discrepancies among Entangled Two-Photon Measurement Techniques. *The Journal of Physical Chemistry Letters,* 4934–4940. https://pubs.acs.org/doi/10.1021/acs.jpclett.2c00865 (2022).

5. Rumi, M. & Perry, J. W. Two-photon absorption: an overview of measurements and principles. *Advances in Optics and Photonics* **2,** 451–518. https://www.osapublishing.org/aop/abstract.cfm?uri=aop-2-4-451 (2010).

6. Ma, Z.-C. *et al.* Measurement of Two-Photon Absorption Cross Section of Metal Ions by a Mass Sedimentation Approach. *Scientific Reports* **5,** 1–8. https://www.nature.com/articles/srep17712 (2015).

7. Drago, C. & Sipe, J. E. Aspects of two-photon absorption of squeezed light: The continuous-wave limit. *Physical Review A* **106,** 023115. https://link.aps.org/doi/10.1103/PhysRevA.106.023115 (2022).

8. Raymer, M. G. & Landes, T. Theory of two-photon absorption with broadband squeezed vacuum. *Physical Review A* **106,** 013717. https://link.aps.org/doi/10.1103/PhysRevA.106.013717 (2022).

9. Landes, T. *et al.* Quantifying the enhancement of two-photon absorption due to spectral-temporal entanglement. *Optics Express* **29,** 20022–20033. https://opg.optica.org/oe/abstract.cfm?uri=oe-29-13-20022 (2021).

Appendix D

SUPPLEMENTARY INFORMATION FOR ENTANGLED PHOTON CORRELATIONS ALLOW A CONTINUOUS-WAVE LASER DIODE TO MEASURE SINGLE PHOTON, TIME-RESOLVED FLUORESCENCE

D.1 Select optical properties of ICG

Solvent	Peak absorption/emission wavelength (nm)	ε $cm^{-1}mol^{-1}$ at λ_{max}	Φ
Methanol	784/809	221,000	0.09
Ethanol	787/811	167,000	0.11
DMSO	794/817	170,000	0.12

Table D.1: Select optical properties of ICG in methanol, ethanol, and DMSO from Ref. [1].

D.2 Confirmation of fluorescence

While the results presented in the main text of the chapter suggest that the coincidences observed with the sample present originate from fluorescence due to the good agreement between the observed histograms and fits, a control experiment as additional evidence was performed to rule out the role of scatter from the excitation beam. Additionally, a blank scan was performed, where the dye solution was replaced with only methanol. Fig. D.1 displays this histogram, as well as a side-by-side comparison of the histograms observed with and without the dye. The lack of an obvious coincidence peak suggests that the SPDC flux is sufficiently filtered from the fluorescence detector, and that the coincidences observed in the experiment originated from fluorescence of the sample.

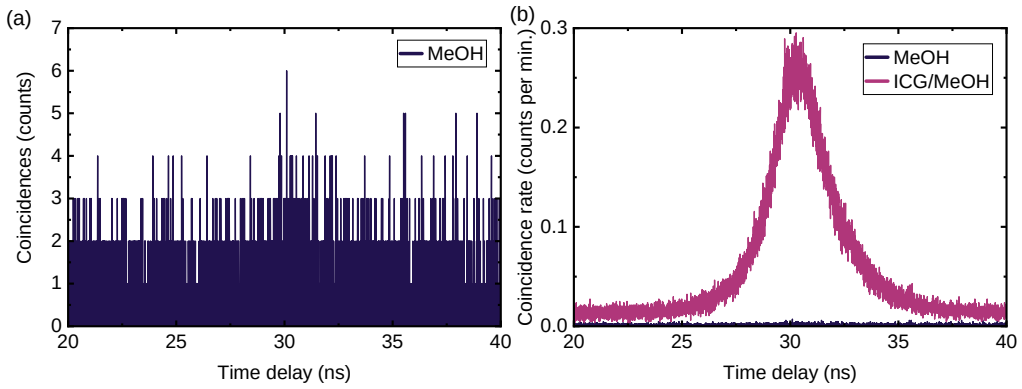

Figure D.1: Coincidence histograms of pure methanol and methanol/indocyanaine solutions. (a) Coincidence histogram from methanol blank experiment. (b) Coincidence rates for blank methanol and ICG/methanol solutions.

D.3 Experimental stability and background

Over the course of the 14-16 hour scans presented in Fig. 6.3, minimal drift or sample degradation were observed. Fig. D.2 shows the singles and coincidence count rates over the course of the experiment. Coincidence count rates were obtained by summing all coincidence counts between 24 and 34 nanoseconds and subtracting the product of accidentals per bin and the number of bins in this window. The accidental rate per bin was obtained by averaging the number of coincidences observed from 50 to 70 ns, far from the coincidence peak. While a slight decrease in the heralding channel (Channel 0) is observed in the DMSO data over time likely due to drift in the alignment, this change in intensity is about 1% of the original value. The singles rate in the fluorescence arm (Channel 1) as well as the coincidence rate appear to remain steady over time. While ICG is known to exhibit degradation over time due to a number of factors, we do not observe a loss in coincidence counts likely because the sample is exposed to low light levels, and the sealed cuvette containing the dye had minimal headspace. The observed fluctuations in the coincidence data is not due to technical noise, but rather the Poissonian statistics of a shot-noise limited system, as the variance of the observed rates is nearly equivalent to the mean of the rate (Table D.2).

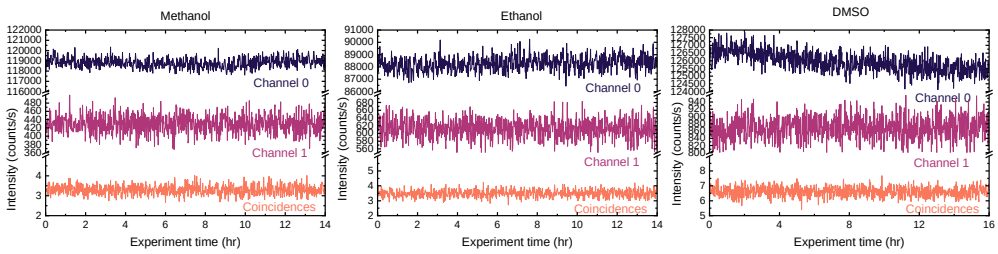

Figure D.2: Count rates in Channel 0 (reference photons), Channel 1 (fluorescence photons), and coincidences from 100μM ICG in methanol, ethanol, and DMSO experiment over the course of the scan.

Parameter	Mean rate (counts per second)	Rate variance (counts/second)^2
Heralding singles	12600	39300
Fluorescent singles	870	880
Raw coincidences	8.3	8.0
Accidental coincidences	0.78	0.77
True coincidences	7.5	8.7

Table D.2: Count rate means and variances demonstrating nearly shot-noise limited statistics.

The background of the experiments presented here are low, but some stray light is likely still present. From the blank experiment, the singles rate at the fluorescence detector was 28 ± 5 counts per second, slightly higher than the specified dark count rate of the detectors at 10 counts per second. Regardless, the fluorescence counts observed during experiments with dye are substantially higher, suggesting that these counts are mostly fluorescence and not background.

D.4 Lifetime fits with residuals

Fits of the raw histograms are shown in Fig. D.3 on a logarithmic scale to show the accuracy of the fit extending to the tails of the coincidence peaks over several decades of intensity.

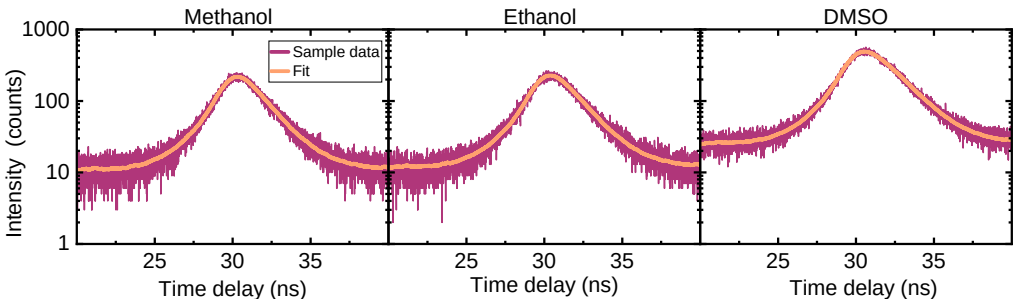

Figure D.3: Raw coincidence data and fits for ICG in methanol (left), ethanol (center), and DMSO (right) on a logarithmic scale.

The weighted residuals are shown in Fig. D.4, the lack of obvious trends in the data suggest that the model used for fitting the data is reasonable. Here, the residuals are weighted by the inverse square of the fit value at each timepoint, as the uncertainty of the counts is proportional to this value for Poissonian data.

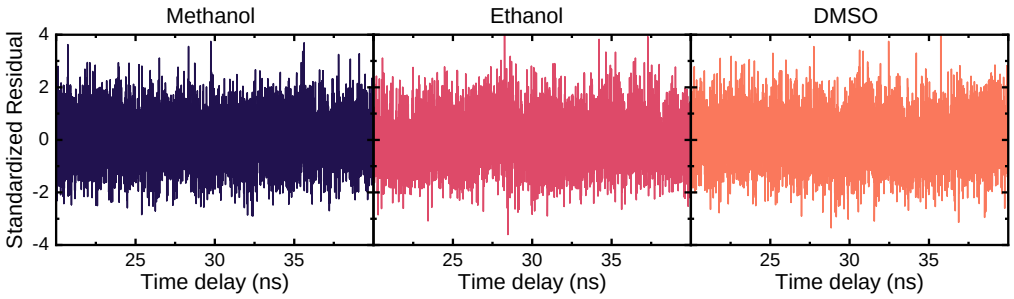

Figure D.4: Weighted residuals of the fits from Fig. D.3.

D.5 Fitting algorithm

The fits presented in this work were performed in a custom Matlab program using the iterative reconvolution technique. First, the accidentals present in the IRF, as obtained by averaging the histogram coincidence counts from 50-70 ns, were subtracted from the raw data, and the data were truncated to a 20-40 ns window to reduce the amount of baseline present in the fit. The resulting true coincidence curve was then scaled so that the sum of counts over the IRF was unity. The experimental data from each sample were also truncated to a 20-40 ns window. The accidental counts were not subtracted from the sample coincidence curve, as these were treated

as a fit parameter. The accidental data was also normalized so that the sum of counts was equal to unity. The sample response model functions were of the form:

$$R(t_i) = c(e^{-t_i/\tau} + A) \tag{D.1}$$

where τ, the fluorescence lifetime, and A¸a factor accounting for accidentals, are the fit parameters. The constant c is used to normalize the area of the sample response to unity. The normalization in all three cases is necessary because the convolved response of two functions has an area equal to the product of the areas of the original functions. The experiment response function was calculated as a discrete convolution of the sample response and the IRF, truncated to the length of the experimental data, and normalized to an area of one. Then, a trust-region nonlinear regression algorithm was performed to estimate the parameters τ and A that minimize the sum of squared errors between the experimental data and the fit.

References

1. Berezin, M. Y., Lee, H., Akers, W. & Achilefu, S. Near Infrared Dyes as Lifetime Solvatochromic Probes for Micropolarity Measurements of Biological Systems. *Biophysical Journal* **93,** 2892–2899. https://www.cell.com/biophysj/abstract/S0006-3495(07)71542-4 (2007).

INDEX